Nonlinear Optical Processes in Bulk and Waveguide Structures in the Infrared

John Edward McCarthy

Submitted for the degree of Doctor of Philosophy

School of Engineering and Physical Sciences

Heriot-Watt University

July – 2013

Abstract

The results of an experimental study into the third order nonlinear optical properties of chalcogenide glasses at a wavelength of 1550 nm are presented. Of the glasses investigated glass gallium lanthanum sulphide (GLS) was found to have an optical Kerr nonlinearity approximately 70 times higher than silica. Additionally the upper limit of GLS nonlinear absorption coefficient was measured to be over an order of magnitude smaller than the other chalcogenide glasses analysed. GLS was subsequently chosen as the host material for waveguide fabrication via ultrafast laser inscription. Near and mid infrared singlemode waveguide structures were successfully fabricated and their nonlinear guiding properties investigated. These investigations led to the generation of a supercontinuum from a singlemode waveguide that spanned over 3000 nm throughout the mid wavelength infrared spectral region. Studies into the contributing mechanisms of supercontinuum generation are presented in work conducted in silica based photonic crystal fibres with the extent of the supercontinuum generation being limited by the transmission range of silica. An investigation into saturable absorption effects in single walled carbon nanotubes is also presented. This study identified that for field irradiances on the order of 9.5×10^{13} W/m^2 the contribution of multi-photon absorption exceeded that of saturable absorption.

Acknowledgements

First and foremost I would like to thank my supervisor Professor Ajoy Kar for his help and support throughout my time as a student at Heriot-Watt.

I would also like to thank the other members of the nonlinear optics group for their help, most specifically Dr. Henry Bookey for his guidance and advice which has been instrumental throughout my PhD.

I thank our collaborators at the Central Glass and Ceramics Research Institute for providing photonic crystal fibres and allowing me to witness the many aspects of PCF fabrication during my stay with them.

I am indebted to my office mates whose keen interest in photonics often resulted in impromptu troubleshooting discussions over cups of coffee.

I would like to thank my mum and dad for their support and encouragement over the years and my fiancée Catherine for her love, friendship and relentless badgering. Without them none of this would have been possible.

Finally, I am eternally grateful to my high school physics teacher, Dr. Kevin Costello who was the most inspirational educator I have ever met. His passion for teaching inspired me, and many others, to pursue a career in physics.

ACADEMIC REGISTRY
Research Thesis Submission

Name*:*	John E. McCarthy		
School/PGI:	EPS		
Version: *(i.e. First, Resubmission, Final)*	First	Degree Sought (Award **and** Subject area)	PhD, Physics

Declaration

In accordance with the appropriate regulations I hereby submit my thesis and I declare that:

1) the thesis embodies the results of my own work and has been composed by myself
2) where appropriate, I have made acknowledgement of the work of others and have made reference to work carried out in collaboration with other persons
3) the thesis is the correct version of the thesis for submission and is the same version as any electronic versions submitted*.
4) my thesis for the award referred to, deposited in the Heriot-Watt University Library, should be made available for loan or photocopying and be available via the Institutional Repository, subject to such conditions as the Librarian may require
5) I understand that as a student of the University I am required to abide by the Regulations of the University and to conform to its discipline.

* *Please note that it is the responsibility of the candidate to ensure that the correct version of the thesis is submitted.*

Signature of Candidate*:*		Date:	

Submission

Submitted By *(name in capitals):*	AJOY K. KAR
Signature of Individual Submitting:	
Date Submitted:	

For Completion in the Student Service Centre (SSC)

Received in the SSC by *(name in capitals):*			
Method of Submission (Handed in to SSC; posted through internal/external mail):			
E-thesis Submitted (mandatory for final theses)			
Signature:		Date:	

Publications by the Author

Peer reviewed journal articles by the author

J. McCarthy, H. Bookey, N. Psaila, R. Thomson, and A. K. Kar, "Mid-Infrared spectral broadening in an ultrafast laser inscribed gallium lanthanum sulphide waveguide," Optics Express **20**, 1545-1552, (2012).

R. Buczynski, H. T. Bookey, D. Pysz, R. Stepien, I. Kujawa, J. McCarthy, A.,Waddie, A. Kar, and M. Taghizadeh, "Supercontinuum generation up to 2.5μm in photonic crystal fiber made of lead-bismuth-galate glass," Laser Phys. Letters **7**, 666-672, (2010).

D. Ghosh, S. Roy, M. Pal, A. Pal, S. K. Bhadra, J. McCarthy, H. T. Bookey, and A. K. Kar "Generation of supercontinuum and its theoretical study in three-ring silica microstructured optical fibers," Applied Optics, **48**, G12-G20, (2009).

H. T. Bookey, S. Dasgupta, N. Bezawada, B. P. Pal, A. Sysoliatin, J. McCarthy, M. Salganskii, V. Khopin, A. K. Kar, "Experimental demonstration of spectral broadening in an all-silica Bragg fiber." Optics Express, **17**, 17130-17135, (2009).

R. Rangel-Rojoa, J. McCarthy, H. T. Bookey, A.K. Kar, L. Rodriguez-Fernandez, J.C. Cheang-Wong, A. Crespo-Sosa, A. Lopez-Suarez, A. Oliver, V. Rodriguez-Iglesias and H.G. Silva-Pereyra, "Anisotropy in the nonlinear absorption of elongated silver nanoparticles in silica, probed by femtosecond pulses," Opt. Comms. **282**, 1909-1912, (2009).

J. McCarthy, H. T Bookey, S. Beecher, R. Lamb, I. Elder, and A. K. Kar, "Spectrally tailored mid-infrared supercontinuum generation in a buried waveguide spanning 1750 nm to 5000 nm for atmospheric transmission," Applied Phys. Letters, **103**, 151103 (2013)

J. McCarthy, H. T. Bookey, A. K. Kar, and A. C. Ferrari, "Bleaching of SCWNT saturable absorption in the femtosecond pulse regime," (To be submitted to APL).

Conference papers by the author

J. McCarthy, H.T. Bookey, N.D. Psaila, R.R. Thomson, and A.K. Kar, "Mid-infrared guiding and nonlinear spectral broadening in ultrafast laser inscribed gallium lanthanum sulphide waveguides," in the 23rd annual meeting of IEEE photonics society, Denver 2010.

Contents

List of figures

List of abbreviations

AR	Anti reflection
BBO	Barium borate
CGCRI	Central glass and ceramic research institute
CUDOS	Centre for ultrahigh-bandwidth devices for optical systems
CPA	Chirped pulse amplification
FOM	Figure of merit
FWM	Four wave mixing
GLS	Gallium lanthanum sulphide
GVD	Group velocity dispersion
MBE	Molecular beam epitaxy
MI	Modulation instability
MIMIC	Micro moulding in capillaries
MOCVD	Metal organic chemical vapour deposition
MWIR	Mid wavelength infrared
NA	Numerical aperture
ND	Neutral density
OCT	Optical coherence tomography
OPA	Optical parametric amplifier
OPO	Optical parametric oscillator
ORC	Optoelectronics research centre
PBS	polarising beam splitter
PCF	Photonic crystal fibre
PMMA	Poly(methyl methacrylate)
SESAM	Semiconducting saturable absorbing mirror
SPM	Self phase modulation
SRS	Stimulated Raman scattering
SSFS	Soliton self frequency shift
SWCNT	Single walled carbon nanotubes
ULI	Ultrafast laser inscription
XPM	Cross phase modulation
ZDW	Zero dispersion wavelength

Chapter 1. Introduction

1.1. Background

For low field intensities the properties of a material are independent of the light intensity. However as the field intensity is increased the optical response of the material can become nonlinear in nature, i.e. material properties such as transmission and refractive index can become dependent on the field intensity. Maria Goeppert-Mayer could be considered the mother of nonlinear optics as she identified the first all optical nonlinear effect, two-photon absorption, in 1931 [1]. Due to the large field intensities required it wasn't until 30 years later, a year after the advent of the laser, that the first experimental demonstration of a nonlinear optical process was reported by Franken et. al. [2]. Here they demonstrated the frequency doubling of light from a ruby laser when focused onto a quartz crystal. Soon after this first demonstration a plethora of other nonlinear optical processes were experimentally demonstrated as more research groups gained access to first generation laser systems. These nonlinear processes have in return enhanced the field of laser physics for example; Ti:Sapphire laser cavities are often optically pumped by a frequency doubled Nd:YAG laser. In this process the frequency doubled Nd: YAG output of 532 nm is well matched to the peak absorption cross-section of Ti: Sapphire allowing for an efficient absorption of the pump.

The nonlinear process of high harmonic generation (HHG) can be used to generate the shortest laser pulses on record [3]. Here a high intensity laser field, typically with a near infrared wavelength of emission is focused in a noble gas jet. Through a three-step process of field ionisation, acceleration and recombination, harmonic generation pulses of light up to the 51^{st} harmonic of the input light can be generated. Typical emission therefore occurs in the extreme ultraviolet or soft X-ray region of the electromagnetic spectrum. Due to the nature of the process the pulses are on the order of hundreds of attoseconds, these short pulses can then be used to time-resolve atomic dynamic processes such as electron tunnelling [4].

Time resolved optical spectroscopy, outside of HHG, can utilise another nonlinear process; parametric oscillation. Optical Parametric Oscillators (OPO) offer very broad wavelength tuneability as changing the phase-matching condition alters the generated signal and idler wavelengths. This is useful for spectroscopic analysis as the wavelength can be tuned to be on resonance of a particular test system. Naturally broadly tuneable sources of coherent radiation, like that provided by OPOs, have many applications outside of spectroscopy in both experimental and applied settings. Similarly the generation of a spectrally broad (on the order of over 1000 nm) source of coherent radiation is also of interest to many fields. Such sources are typically called *supercontinuum sources.* For instance Optical Coherence Tomography (OCT) is an interferometric technique which allows for three dimensional image analysis [5]. Due to the non-destructive testing nature of OCT it is typically used to generate 3D models of biological tissue [6] and can be used to monitor the progression of glaucoma [7]. Using broadband light sources will decrease the coherence length of the source; this will increase the spatial resolution of the interferometric imaging process and allow for a more detailed 3D model to be produced.

Similarly supercontinuum generation in the visible region of the electromagnetic spectrum is often used to characterise the solar-cells [8] as the broad spectrum can be tailored to emulate the sun's spectral output under a number of atmospheric conditions. Supercontinuum centred in the near infrared is of interest to the telecommunications industry as a proposed source of dense wavelength division multiplexing through spectral splicing/filtering [9]. Indeed, supercontinnum generation is one of the most interesting and extensively researched fields in nonlinear optics today. Of particular interest are the nonlinear mechanics involved in the process and to what extent each process contributes and how they shape the overall spectrum.

1.2. Supercontinuum generation

Supercontinuum generation refers to the spectral broadening of an intense optical pulse through nonlinear interaction and propagation inside a transparent material. Supercontinuum generation was first demonstrated in 1970 by Alfano and Shapiro by passing high power picosecond pulses through borosilicate (BK7) glass [10]. The pulses

were produced by pumping the glass with the frequency doubled output of a dye Q-switched Nd:Glass mode-locked laser with central wavelength of emission of 530 nm. The emission extended from 400 - 700 nm, this gave the supercontinuum generation a white-light appearance. The mechanism for the spectral broadening was attributed to a four wave parametric process occurring within the glass. Interestingly the term 'supercontinuum' generation was not used in relation to this process until ten years later by Gersten, Alfano and Belic [11]. Research into supercontinuum generation since this first demonstration in 1970 has been driven by the continued advances in the field of laser technology and fibre optics.

A significant landmark in laser development with regards to supercontinuum generation, and nonlinear optics in general, was the demonstration of the Kerr lens modelocked Ti:Sapphire laser [12]. In comparison with the larger and considerably higher-maintenance dye lasers of the time period, the modelocked Ti: Sapphire system offered a more compact and robust laser source for ultrashort pulses - pulses with durations of less than 1×10^{-12} seconds. Similarly the development of low-loss silica optical fibre attracted interest from those wanting to enhance nonlinear frequency conversion as they allowed for high field confinement over the length of the fibre and thus long pulse-material interaction lengths [13]. The improvement of fibre drawing techniques led to the development of microstructured fibre, commonly referred to as Photonic Crystal Fibre (PCF). This fibre design offered an increased modal confinement and unique dispersion tailoring qualities not available to standard step index fibre [14].

Researchers now had access to extremely high peak power sources from Ti:Sapphire lasers and the means of confining these pulses over long lengths in PCF. The significance of these two technological advances to the field of supercontinuum generation was demonstrated to great effect by J. Ranka et. al. in 2000 [15]. A supercontinuum spanning 390 – 1600 nm was produced with pulse energies of 800 pJ. Here they used a Ti: Sapphire laser oscillator which emitted pulses with durations of 100 fs at a repetition rate of 83 MHz and, most importantly, with a central wavelength of emission of 790 nm. These pulses were coupled to a 75 cm long PCF with a ZDW of 780 nm. The pump wavelength was 10 nm into the anomalous dispersion regime which

allowed for solitary wave propagation to impact upon the nonlinear pulse propagation along the fibre.

The relative advances in both laser and optical fibre technology since 2000 have seen modelocked rare-earth doped fibre lasers such as the ytterbium [16] and erbium fibre lasers [17] start to replace Ti:Sapphire laser systems as they are more compact and are easier to implement in a commercial device. The wide range of rare earth dopants and their respective emission wavelengths allow for high degrees of wavelength selectivity for pump sources. Indeed, all fibre continuum sources are more adaptable for medical industrial imaging environments, for example in OCT, due to the flexibility and manoeuvrability that fibres offer.

The first demonstration of a fully fibre integrated continuum source was reported by Rulkov et. al. in 2005 [18]. The laser source was a fibre amplified ytterbium doped passively modelocked fibre ring laser. This was spliced to a photonic-bandgap guiding photonic crystal fibre which generated the supercontinuum. Following on from this research conducted by Rulkov et. al. there are a number of commercially available compact all-fibre based continuum sources which operate in the visible to near infrared [19].

1.3. Thesis outline

Chapter 2 will present an introduction to the various nonlinear processes involved in supercontinuum generation in guided media. This is followed by a review of a number of optical fibre and waveguide designs that have been implemented to extend continuum generation into the mid infrared. Chapter 2 concludes with a detailed description of the femtosecond laser system used throughout this thesis.

Chapter 3 begins with a detailed description of the z-scan experimental technique. The z-scan technique is a highly effective method which is used to characterise the nonlinear coefficients of a material using a single beam. The nonlinear coefficients derived from the z-scan results are used to determine the nonlinear switching figures of merit of a

number of chalcogenide and tellurite glass systems at the telecoms wavelength of 1550 nm.

Chapter 4 focuses on the study of supercontinuum generation in photonic crystal fibres. The onset of spectral broadening is investigated in silica based photonic crystal fibres in order to aid computational modelling of the mechanics of supercontinuum generation. As supercontinuum generation is limited by the transmission range of the material, chapter 4 then presents results which focused on extending the long wavelength edge of the supercontinuum by investigating a non-silica micro-structured fibre which exhibited increased mid-IR transmission. Finally, Chapter 4 closes by presenting nonlinear spectral broadening measurements conducted on a multi-core fibre with evanescent field interaction between cores.

Chapter 5 is concerned with the use of nonlinear optical measurements on the characterisation of two important nanostructured materials – metallic nanostructures and carbon nanotubes. The polarisation dependent saturable absorption effects in silver nanostructures embedded in a silica matrix are presented. Also studied in this chapter are the coupled saturable absorption and nonlinear absorption effects in single walled carbon nanotubes at irradiances much higher than the saturation irradiance. The high peak powers available from the laser system enabled the study of both saturable absorption and nonlinear absorption occurring in the same sample simultaneously.

Chapter 6 surmises the development of a nonlinear chalcogenide waveguides fabricated by the ultrafast laser inscription technique (ULI). This will include a brief overview of the ULI process. The importance of fabrication parameters with regards to material modification of chalcogenides is discussed and demonstrates how the ULI process may be easily utilised to fabricate single-mode guiding structures for wavelengths in both the near and mid infrared (2-5 μm). The nonlinear guiding characteristics of single-mode guiding structures are then tested leading to supercontinuum generation in the near and mid infrared.

Finally, chapter 7 draws conclusions and suggests future research prospects for the fields of mid infrared nonlinear optics and continuum generation. This includes proposed designs for mid-IR directional couplers and evanescent field sensors.

1.4. Summary

The work carried out in this thesis focused on nonlinear interactions in the near and mid infrared. Encompassed in this work was the study of continuum evolution in silica based photonic crystal fibres and their limitation with regards to mid infrared guiding. This then lead to the nonlinear characterisation of suitable mid infrared transparent materials and finally implementation of the selected material for waveguide fabrication by the ultrafast laser inscription process. The landmark developments in the field of supercontinuum generation have been outlined above and the main design considerations for maximising supercontinnum generation were introduced.

Chapter 2. Review of supercontinuum generation

2.1. Introduction

This chapter gives an overview of the fundamental physical processes involved in supercontinuum generation. The nonlinear refractive index term is derived from the nonlinear polarisability tensor of a material. How this intensity dependent refractive index and other nonlinear optical processes interact to produce new wavelength components of an optical pulse are then outlined with emphasis on nonlinear propagation in optical fibres. This is followed by a historical review of the research conducted in this field, such as the development of silica photonic crystal fibres, tapered fibres and compound glass fibres. Finally the chapter concludes with a detailed description of the femtosecond laser system that is used throughout this thesis.

2.2. Nonlinear polarisation

The induced polarisation of a medium **P**, under the illumination of light with weak electric field strength **E**, can be expressed by the following equation:

$$\boldsymbol{P} = \varepsilon_0 \chi^{(1)} \boldsymbol{E} \qquad \textit{Eq. (2.1)}$$

where ε_0 is the permittivity of free space and $\chi^{(1)}$ is the linear susceptibility tensor which accounts for linear refraction and absorption. However, when the electric field strength approaches that of the materials inter atomic field strength its resulting polarisation response has a nonlinear dependence. This can be described by the following equation [20]:

$$\boldsymbol{P} = \varepsilon_0 \chi^{(1)} \boldsymbol{E} + \varepsilon_0 \chi^{(2)} \boldsymbol{EE} + \varepsilon_0 \chi^{(3)} \boldsymbol{EEE} + \cdots \qquad \textit{Eq. (2.2)}$$

where $\chi^{(2)}$ is the second order nonlinear susceptibility and $\chi^{(3)}$ is the third order nonlinear susceptibility. For materials that are centrosymmetric, such as amorphous glasses, liquids and gasses, the second order nonlinear susceptibility, $\chi^{(2)}$,is zero.

In order to demonstrate the effect of nonlinear polarisation consider the effect of an intense monochromatic laser beam propagating through a crystal and therefore $\chi^{(2)}$ is non-zero. For an electric field expressed as:

$$\boldsymbol{E} = \boldsymbol{E_0} cos\ (\omega t - kz) \qquad \textit{Eq. (2.3)}$$

Here *k* is the propagation constant. The linear polarisation term can simply be expressed as:

$$\boldsymbol{P^{(1)}} = \varepsilon_0 \chi^{(1)} \boldsymbol{E_0} cos\ (\omega t - kz) \qquad \textit{Eq. (2.4)}$$

The nonlinear polarisation term due to $\chi^{(2)}$ can be defined as:

$$\boldsymbol{P}^{(2)} = \varepsilon_0 \chi^{(2)} . (\boldsymbol{E_0} cos\ (\omega t - kz))^2 \qquad \textit{Eq. (2.5)}$$

This can then be expressed as:

$$\boldsymbol{P}^{(2)} = \frac{1}{2} \varepsilon_0 \chi^{(2)} \boldsymbol{E_0}^2 (1 + cos\ (2kz - 2\omega t) \qquad \textit{Eq. (2.6)}$$

Similarly the nonlinear polarisation term, $\boldsymbol{P}^{(3)}$, due to $\chi^{(3)}$ can be defined as:

$$\boldsymbol{P}^{(3)} = \varepsilon_0 \chi^{(3)} \boldsymbol{E_0}^3 \left(\frac{1}{4} cos(kz - \omega t) + \frac{3}{4} cos\ (3kz - 3\omega t) \right) \qquad \textit{Eq. (2.7)}$$

Combining equations 2.4, 2.6 and 2.7 gives:

$$\boldsymbol{P} = \varepsilon_0\chi^{(1)}\boldsymbol{E_0}\cos(\omega t - kz) + \frac{1}{2}\varepsilon_0\chi^{(2)}\boldsymbol{E_0}^2(1 + \cos(2kz - 2\omega t) + \varepsilon_0\chi^{(3)}\boldsymbol{E_0}^3\left(\frac{1}{4}cos(kz - \omega t) + \frac{3}{4}cos\ (3kz - 3\omega t)\right) \quad \textit{Eq. (2.8)}$$

From equation 2.8 one can see that the second order susceptibility has given rise to a new frequency term that has a frequency twice that of the input field, generation of a second harmonic. There is also generation of a static electric field within the crystal which is a process known as optical rectification. If two waves of different frequency, e.g. ω_1 and ω_2, are incident onto a material where $\chi^{(2)} \neq 0$ then processes such as difference frequency ($\omega_3 = \omega_2 - \omega_1$) and sum frequency ($\omega_3 = \omega_2 + \omega_1$) generation can occur.

The second bracketed term in equation 2.7 shows the presence of third harmonic generation, 3ω, due to the third order nonlinear susceptibility. The first bracketed term in equation 2.7 provides a nonlinear contribution to the polarisation that is matched to the frequency of the input field; this term is responsible for materials intensity dependent refractive index.

2.3. Intensity dependent refractive index

In centrosymmetric materials $\chi^{(2)} = 0$, thus equation 2.2 can be simplified to:

$$\boldsymbol{P} = \varepsilon_0\left[\chi^{(1)} + \chi^{(3)}\boldsymbol{E}^2\right]\boldsymbol{E} \quad \textit{Eq. (2.9)}$$

The bracketed term in equation 2.9 gives the term for the effective electrical susceptibility:

$$\chi_{eff} = \chi^{(1)} + \chi^{(3)}\boldsymbol{E}^2 \quad \textit{Eq. (2.10)}$$

At optical frequencies most materials have a relative permeability of ~1. The refractive index of a material can therefore be expressed [21]:

$$n^2 = 1 + \chi_{eff} \qquad \textit{Eq. (2.11)}$$

Similarly the linear refractive index term can be expressed as:

$$n_0{}^2 = 1 + \chi^{(1)} \qquad \textit{Eq. (2.12)}$$

Re-arranging equations 2.11 and 2.12 and substituting into equation 2.10 gives:

$$n = n_0 \sqrt{1 + \frac{\chi^{(3)} \boldsymbol{E}^2}{n_0{}^2}} \qquad \textit{Eq. (2.13)}$$

Since, $\frac{\chi^{(3)} \boldsymbol{E}^2}{n_0{}^2} << 1$ equation 2.13 can be simplified to:

$$n \approx n_0 \left(1 + \frac{\boldsymbol{E}^2 \chi^{(3)}}{2 n_0{}^2}\right) \qquad \textit{Eq. (2.14)}$$

Irradiance of the incident field is defined as:

$$I = \frac{c \varepsilon_0}{2 n_0} |\boldsymbol{E}|^2 \qquad \textit{Eq. (2.15)}$$

Therefore:

$$n = n_0 + n_2 I, \qquad \textit{Eq. (2.16)}$$

where n_2 is defined as:

$$n_2 = \frac{\chi^{(3)}}{c n_0{}^2 \varepsilon_0} \qquad \textit{Eq. (2.17)}$$

the n_2 term is a constant and is the materials intensity dependent refractive index and can either be positive or negative. It is the intensity dependent refractive index of a material that gives rise to the effects of self focussing and de-focussing of a field through that material. In terms of supercontinuum generation it is responsible for the generation of new frequencies via a process known as self-phase modulation. How these newly generated wavelengths then interact with each other in a media is then largely dependent on the material dispersion properties. In guided media, such as optical fibres, managing the dispersion over the interaction length is crucial to optimising the extent of the continuum.

2.4. Nonlinear propagation processes in guided media

Essentially the two key characteristics of continuum generation in waveguides are; the waveguides dispersion profile and the effective nonlinear refractive index experienced by the waveguide mode. In this section basic nonlinear mechanisms and their contribution to continuum generation are introduced.

2.4.1. Dispersion

The effect of material dispersion on an electromagnetic wave is dependent on how the material refractive index varies with frequency – the material's chromatic dispersion. Due to this refractive index variation, different wavelengths of a pulse will be travelling at different speeds and thus have different propagation constants, *β(ω)*. This can be defined as [22]:

$$\beta(w) = \frac{\omega n(w)}{c} \qquad \textit{Eq. (2.18)}$$

The group velocity, V_g, in terms of frequency can be defined as:

$$V_g = \frac{d\omega}{d\beta} = \frac{(c/n)}{1 + \frac{\omega}{n}\frac{dn}{d\omega}} \qquad \textit{Eq. (2.19)}$$

And in terms of wavelength as:

$$V_g = \frac{(c/n)}{1 - \frac{\lambda}{n}\frac{dn}{d\lambda}} \qquad \textit{Eq. (2.20)}$$

In of the case of ultrashort pulse propagation, which typically have large pulse bandwidths, the group velocity dispersion (GVD) can mean that different wavelengths in the pulse bandwidth experience different group velocities and can lead to a positive or negative chirping of the pulse.

To account for dispersion we expand the mode propagation constant, β, in a Taylor series [23]:

$$\beta(\omega) = n(\omega)\frac{\omega}{c} = \beta_0 + \beta_1(\omega - \omega_0) + \frac{1}{2}\beta_2(\omega - \omega_0)^2 + \cdots \qquad \textit{Eq. (2.21)}$$

where ω_0 is defined as the central frequency of the pulse. β_0 is equal to 1 over the phase velocity. β_1 is equal to 1 over the group velocity (v_g). β_2 is the parameter for group velocity dispersion and is defined as equation 2.22 in the frequency domain and in terms of wavelength it has is defined as in equation 2.23 [24]:

$$\beta_2 = \frac{d}{d\omega}\left(\frac{1}{V_g}\right) = \frac{1}{c}\left(2\frac{dn}{d\omega} + \omega\frac{d^2n}{d\omega^2}\right) \qquad \textit{Eq. (2.22)}$$

$$\beta_2 = \frac{\lambda^3}{2\pi c^2}\frac{d^2n}{d\lambda^2} \qquad \textit{Eq. (2.23)}$$

The β_2 term can then be used to express fibre dispersion, D, in terms of ps/nm/km and is defined as [25]:

$$D = -\left(\frac{2\pi c}{\lambda^2}\right)\beta_2 \qquad \textit{Eq. (2.24)}$$

The wavelength where β_2 crosses zero is classified as the materials zero dispersion wavelength, in fused silica the point in which $\beta_2 = 0$ is 1.27 µm. Wavelengths at which

β_2 is positive are classified to be in the normal dispersion regime and those wavelengths where β_2 is negative are classified to be in the anomalous dispersion regime.

The Zero Dispersion Wavelength (ZDW) of a waveguide, such as single-mode optical fibre, can be shifted by altering aspects of the waveguide geometry. In standard step-index fibres the overall contribution of waveguide dispersion is weak in comparison to that of chromatic dispersion. Waveguide dispersion arises from the fact that in all but the theoretically ideal guiding case the evanescent field of a guided mode penetrates into the cladding, where this will experience a different $n(\omega)$ from the field contained in the core. As mentioned earlier in the introductory chapter, the location of the pump wavelength with respect to the ZDW of the waveguide can significantly affect the spectral broadening mechanisms that take place. Namely solitary wave propagation can occur when the pump wavelength experiences a small amount of anomalous dispersion as the nonlinear chirp due to the nonlinear refractive index negates the linear chirp due to GVD. When numerically modelling nonlinear pulse propagation in fibres, the β_2 term is sufficient to accurately model supercontinuum generation for pump wavelength far from the waveguides ZDW. However optimum conditions for supercontinuum generation require the pump wavelength to be located close to the ZDW. It is therefore necessary to calculate the higher order dispersive terms, β_3, β_4, β_5 etc, that are present in the waveguide in order to properly model the nonlinear pulse propagation along the waveguide.

2.4.2. Self-phase modulation

As stated above, self-phase modulation (SPM) arises due to the intensity dependent refractive index. An intense optical pulse that propagates along a fibre will induce a nonlinear phase shift upon itself. Consider an intense pulse propagating along a fibre of length, L, with a propagation constant, β equal to $\omega n/c$ hence ignoring the frequency dependence of the refractive index, but taking into account the intensity dependent refractive index (equation 2.25):

$$E(t) = E_0 e^{i(\omega t - \beta L)} + c.c. \qquad \textit{Eq. (2.25)}$$

and

$$E(t) = E_0 e^{i\left(\omega t - \frac{(\omega n_0 L + \omega n_2 I(t) L)}{c}\right)} \qquad \textit{Eq. (2.26)}$$

The intensity dependent phase change, $\emptyset_{NL}(t)$, can then be defined as:

$$\emptyset_{NL}(t) = \frac{\omega n_2 I(t) L}{c} \qquad \textit{Eq. (2.27)}$$

Due to the time varying intensity of the pulse there is therefore a time varying nonlinear phase change which induces an angular frequency change about the central frequency of the pulse. For a material with a positive n_2 this has an effect of red-shifting the leading edge of the pulse and blue-shifting the trailing edge. Neglecting dispersion this broadening will be symmetric about the central pulse frequency. These newly generated frequencies can then interact and affect the nonlinear phase state of the other co-propagating pulse; this process is known as cross-phase modulation (XPM). In the case of continuum generation in order for efficient XPM to occur there needs to be low group-velocity mismatch to allow for temporal overlap. The nonlinear phase change is also enhanced if both frequencies have the same polarisation state. XPM has a number of device applications due to this strong nonlinear polarisation rotation such as ultrafast optical switching [26] and synchronizing two mode-locked fibre lasers [27].

2.4.3. Four-wave mixing

The effects of Four-Wave Mixing (FWM) with regards to continuum generation are more evident when working in the longer pulse regime, i.e. pulse durations > 10ps, as the effects of the soliton propagation and SPM are greatly reduced. Phase-matched FWM allows for the generation of sidebands equally spaced from the pump wavelength. FWM is a parametric process where the parametric gain is provided by the nonlinear refractive index of the fibre material; through conservation of energy and momentum this process can be described as in equations (2.28 and 2.29) [28].

$$2k_{pump} = k_{signal} + k_{idler} + 2P\gamma \qquad \textit{Eq. (2.28)}$$

and

$$2\omega_{pump} = \omega_{signal} + \omega_{idler} \qquad \textit{Eq. (2.29)}$$

where P is the peak pump power, k_{pump}, k_{signal} and k_{idler} are the propagation constants of the pump, signal and idler modes respectively. The terms ω_{pump}, ω_{signal} and ω_{idler} correspond to the frequencies of pump, signal and idler waves. The γ term is the effective fibre nonlinearity and is defined as:

$$\gamma = \frac{2\pi n_2}{\lambda A_{eff}} \qquad \textit{Eq. (2.30)}$$

where A_{eff} is the effective mode area, n_2 is the nonlinear refractive index and λ is the pump wavelength. This effective fibre nonlinearity arises due to the guided mode of an optical waveguide or fibre experiencing a different nonlinear refractive index than simply that of the base material. From equation 2.30 it is evident that a material with a high nonlinear refractive index and a small guided mode area would exhibit a high effective nonlinear refractive index. The high index contrast between the core and the cladding of PCF means that they can support guided modes with a higher degree of core confinement and thus an increased effective nonlinear refractive index. To optimise this phase matching process the fibre would ideally have a flat dispersion profile over a wide range of wavelengths and ideally the pump wavelength should be situated in the anomalous dispersion regime, as a non-zero value of $2P\gamma$ allows sideband generation in the anomalous dispersion regime of fibre via a process known as modulation instability (MI) [29].

2.4.4. Solitary wave propagation and stimulated inelastic scattering

When considering pulse propagation in a waveguide with a positive nonlinear refractive index and at a wavelength where there is a small amount of anomalous dispersion the effects of SPM can cancel with the effect of temporal pulse compression due to

anomalous dispersion and allow for the formation of an optical soliton. Under ideal conditions the fundamental soliton will keep its temporal and spectral shape over long distances [30]. However in the ultrashort pulse regime the inelastic scattering process, of Stimulated Raman Scattering (SRS), can cause a soliton to undergo a self-frequency shift (SSFS). As ultrashort pulse laser sources typically have large input bandwidths the long wavelength edge of the bandwidth can be amplified due to SRS at the expense of power in the short wavelength edge of the bandwidth. This causes a walk-off effect to longer wavelengths as the soliton propagates [31]. The high field irradiances that can be accessed from femtosecond lasers mean that a process called soliton fission can occur. The intense femtosecond pulse can be considered as a high order soliton, upon coupling to a fibre the pulse will broaden and break up into a number of discrete solitons this process is known as soliton fission [32]. These solitons can then self-frequency shift to longer wavelengths. During the initial soliton fission process energy can be deposited into shorter wavelengths, as a form of Cherenkov radiation [33], if these shorter wavelengths lie in the normal dispersion regime then they may temporally overlap with a soliton in the anomalous dispersion regime over a very small distance and thus allow for XPM to occur between the two. This then allows the soliton to be further red shifted and the Cherenkov radiation to experience a further blue shift [34]. Tailoring the fibre guiding characteristics, specifically the group velocity dispersion, can allow for efficient mixing of the waves over a wide range of wavelengths, the red-shifted soliton can continue to co-propagate with blue-shifted Cherenkov radiation.

Supercontinuum can be generated with ultrashort pulses, long pulses or continuous wave pump sources. However the contribution of the different broadening mechanisms introduced in this section will vary depending on the pump pulse regime. Therefore to optimise the supercontinuum generation for a particular source the fibre dispersion profile can be tailored to enhance the dominant nonlinear interaction. For example, dispersion flattened fibre for the long pulse or CW regime allows for stronger phase-matching over a broader wavelength range. Conversely in the ultrashort pulse regime a steep dispersion profile improves the supercontinuum generation enhancing the SSFS.

2.5. Historical review of experimental continuum generation research

2.5.1. Continuum generation in PCF and fibre tapers

The photonic crystal fibre is a fibre designed with a built-in microstructure that runs along its length. After the demonstration of white light continuum in PCF by Ranka in 2000, mentioned in Chapter 1 [15], research interest in supercontinuum generation was reignited. The guiding properties and freedom of design benefits of PCF have been alluded to in previous sections of this thesis. Here these advantages will be explained along with examples of their experimental realisation.

Solid core PCFs guide via total internal reflection. However due to the silica core effectively being surrounded by air cladding, the refractive index contrast is much higher than for standard optical fibre. Figure 2.1 (a) shows a PCF end facet showing the periodic microstructure of the of the air-hole cladding. This allows for a higher modal confinement and a smaller guided mode. From equation 2.30 this then yields a much higher effective nonlinearity.

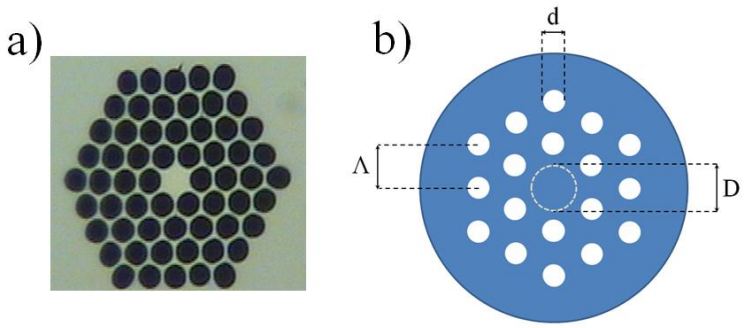

Figure 2.1: (a) Photonic crystal fibre end facet. (b) Schematic of PCF end facet.

This high index contrast also means that there is a much stronger dependence of waveguide dispersion to the overall dispersion. The total contribution of waveguide dispersion in PCFs can also be altered without varying the size of the core - as varying the air-hole size, d, and air-hole spacing, Λ, see figure 2.1 (b). Varying these two parameters will vary the effective index of the cladding and thus alter the waveguide dispersion. This was demonstrated by the fabrication of an endlessly single-mode PCF in 1997 by Birks et. al. [35]. By specific selection of the air hole diameter and air-hole

spacing it was theoretically predicted by Ferrando et. al. [36] that one could flatten the fibre dispersion over a wide range of wavelengths. This was then experimentally realised by Reeves et al [37] where a fibre exhibiting 0 ± 1.2 ps/nm.km over a spectral range of 600 nm from 1.0 - 1.6 μm with a dispersion slope at 1.0 μm of 0.017 ps/nm^2.km and a slope of -0.003 ps/nm^2.km at 1550 nm.

Another degree of design complexity was proposed by Saitoh et. al. [38]. Here they predicted that a flat dispersion profile could be achieved by increasing the size of the air-holes with radius away from the core. Overall the wide variety of design freedoms offered by PCF for extending the ZDW to either long or short wavelengths make it exceptionally well suited as the basis of a supercontinuum source. Many of these dispersion tailoring parameters of PCFs have been identified and then successfully implemented, as in Ref. [37] above, by the Optoelectronics group at Bath University. It was here that the first photonic crystal fibre was drawn. From the late 1990's onwards they have been at the forefront of research into microstructured silica fibre research.

For example in a 2004 experiment, conducted by W. J. Wadsworth et. al. [39], they configured PCF design parameters to enhance continuum generation from a Nd:YAG micro-chip laser. This emitted pulses with a duration of 0.6 ns at a repetition rate of 7.25 kHz and with a central wavelength of 1064 nm. The maximum average power from this laser was 30 mW and thus peak powers up to 6.9 kW. The fibre ZDW was situated at 1039 nm, therefore the pump wavelength was 25 nm into the anomalous dispersion regime. The weak positive dispersion at the pump wavelength of 5.0 ps/nm.km allowed for improved continuum generation through FWM and MI i.e. the main spectral broadening mechanisms for this pulse regime. These features coupled with the small core diameter of approximately 1.5 μm yielded strong nonlinear interactions over long fibre lengths. Figure 2.2 shows the continuum evolution with pump power for 1, 3, 20 and 100 m lengths of index-guided PCF.

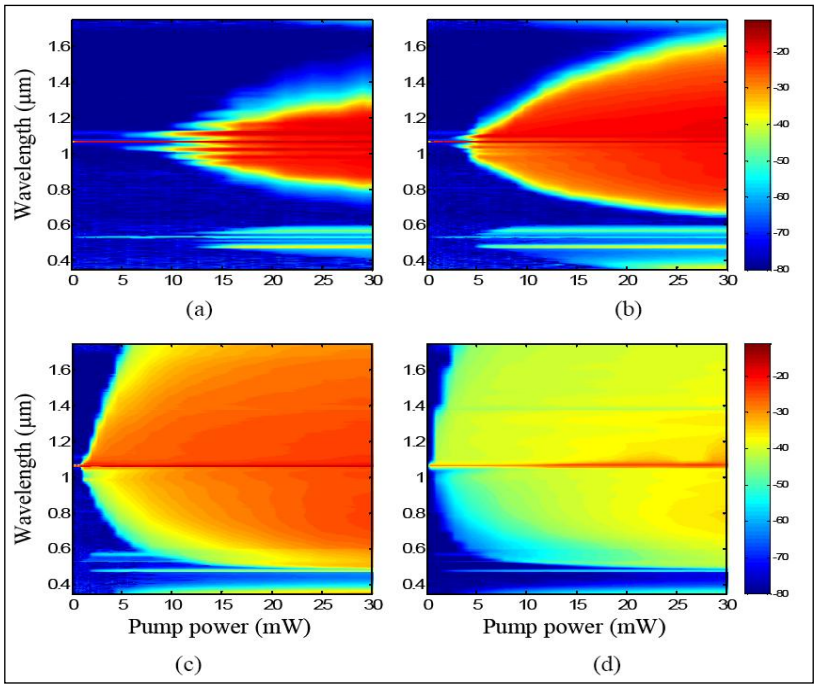

Figure 2.2: Continuum evolution with pump power for (a) 1m (b) 3m (c) 20 and (d) 100m [39]

A spectrally smooth continuum spanning 1400 nm from 500 – 1900 nm was measured at the output of the fibre. Another practical design feature of the fibre was its compatibility with standard fibre cleavers, strippers and splicers. As the fibres outer diameter was designed to match that of SMF-28 i.e. 125 μm outer diameter, 250 μm diameter buffer layer. This experiment demonstrated that spectrally smooth supercontinuum spanning the majority of the silica transmission window could be generated with a low-cost laser source and in a fibre compatible with well established fibre maintenance equipment.

There was however also a considerable amount of loss within the fibre itself. The fibres attenuation coefficient was estimated to be 12 $dBkm^{-1}$ at the pump wavelength of 1064 nm. There was also substantial absorption at the OH ion absorption peak situated at 1380 nm. At this wavelength the loss was calculated to be 110 dB/km, this absorption line is observed in the continuum spectra in Figure 2.2 (d). Additionally the fabrication cost of PCFs is considerably higher than that of standard optical fibre due to the nature of the fibre perform stacking process. A more economical approach to achieve a strongly guided and well confined mode is through fibre tapering.

The process of fabricating a tapered fibre is relatively simple; take a standard SMF-28 silica fibre and stretch it while heating with a flame as demonstrated in 2000 by Birks et. al. [40]. Here they tapered the optical fibre via the 'Flame Brush' technique. The fibre was heated over a flame that travels along the fibre and back while gradually stretching the fibre. This allows for uniform reduction of the fibre diameter over a specific length. No additional fibre design and pre-forming were required. Using this technique it is possible to drastically reduce the size of the fibre; effectively the fibre now guides as if it is a silica thread in air and thus the mode experiences a large refractive index contrast. They showed that the light was now guided in a very small area (approximately 2 μm^2). Like in the PCFs tapered fibres can modify their dispersive properties to such an extent that visible wavelengths are guided in the anomalous dispersion regime. A schematic of the fibre tapering is shown in Figure 2.3 (a) and figure 2.3 (b) show the evolution of the spectrum with input pump powers of 60, 210 and 380 mW. The pulses are emitted by an un-amplified Ti:Sapphire laser with pulses durations on the order of 90 fs, with a repetition rate of 76 MHz and a central wavelength of 850 nm. The continuum produced spanned 1200 nm from 400 to approximately 1600 nm.

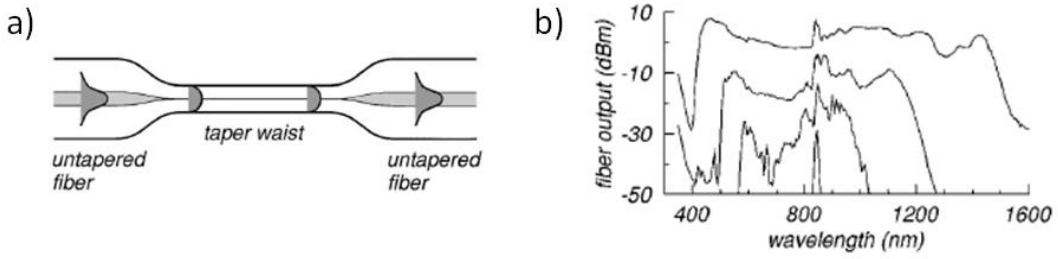

Figure 2.3: *(a) Schematic of tapered step-index silica fibre [40] (b) Evolution of continuum generation in tapered fibre for pulse powers of 60, 210 and 380 mW [40]*

The input and output facets of the fibre are un-tapered and are approximately 9 μm in diameter. It is therefore easier to achieve higher coupling efficiencies to tapered fibres in comparison to PCFs due to the larger area. Tapered fibres will additionally exhibit a higher damage threshold as the irradiance at the input facet will be significantly lower due to the softer focusing of the input radiation [41]. This allows for higher pulse energies to be guided in the fibre. The drawbacks to tapered fibres as a means of continuum generation are that they have to be carefully packaged due to their fragility;

the tapered lengths have to be short. There are also fewer design aspects to shape the dispersion profile of the fibre taper in comparison to PCFs.

With the advance of ultrafast laser sources and the strong guiding characteristics of PCFs, the limiting factor on the width of the continuum generation in silica PCFs is the transmission window of silica itself. Fibre structures such as photonic bandgap PCFs [42] and negative curvature fibre [43] can be used to guide mid-IR radiation in silica based fibres due to the majority of the mode being guided in air. They typically exhibit large mode areas and very low nonlinearity. This makes them un-appealing for supercontinuum generation sources. Conversely the above features are advantageous for applications in laser beam delivery at mid IR wavelengths from sources such as Er:YAG lasers used in dentistry. Therefore to extend the continuum into the mid IR non-silica based fibres must be considered. One such group of materials are chalcogenide glasses.

2.5.2. Chalcogenide glass based supercontinuum generation

A chalcogenide glass is defined as one that contains a large amount of the chalcogen atoms; sulphur, selenium or tellurium mixed with electropositive elements such as arsenic, germanium and gallium which act as network forming elements [44]. The resultant glasses have been shown to have a number of attractive optical properties including high nonlinearity of up to ~500 times that of silica at 1.55 μm [45]. Their high transmission in the 2 - 12 μm mid infrared range also means that they are of interest for military applications which utilise various wavelengths situated within the atmospheric transmission windows of this spectral region [46]. Furthermore, the compositional components, the ratios of those components and the bond configuration of chalcogenide glasses can all be varied. This means that there is a high degree of freedom when trying to tailor a chalcogenide glass to a specific need.

The linear refractive index of a chalcogenide glass is quite large, for example Gallium-Lanthanum-Sulphide (GLS) has a linear refractive index of 2.41 at a wavelength of 1.55μm [47]. This initially leads to problems when coupling into fibres or waveguides due to Fresnel reflection. However anti-reflection coatings on either end surface can

nullify these reflection losses. The high linear refractive index is also an advantage as the high index contrast compared to air will allow for improved confinement in photonic crystal fibres.

The ZDW of chalcogenide glasses usually lies in the mid infrared (e.g. As_2S_3 has a zero dispersion wavelength of 5 μm) well away from the zero-dispersion wavelength of bulk silica which lies at 1.3 μm and much longer than most conventional ultrafast laser sources. For the most part the majority of chalcogenide glasses exhibit strong normal dispersion at telecoms wavelengths of 1.3 μm and 1.55 μm. However, as with silica based waveguides and fibres the zero dispersion wavelength can be shifted down from ~5 μm to near infrared wavelengths [48]. Figure 2.4 shows the dispersion of a chalcogenide glass with wavelength and its linear refractive index profile [49].

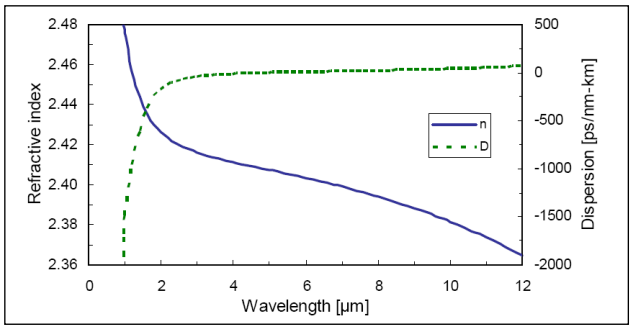

Figure 2.4: Variation of refractive index and dispersion of As_2S_3 with wavelength [49]

Chalcogenide glasses often have a short wavelength absorption edge in the visible region of the spectrum; however unlike crystalline semiconductors they don't exhibit a sharp absorption edge. Instead the absorption spectra of chalcogenides exhibit an Urbach tail; the consequence of this is that photon energies of less than half the band-gap can still cause two photon absorption to occur [50]. However at near and mid infrared wavelengths chalcogenide glasses typically exhibit low multiphoton absorption coefficients. The low levels of multi-photon absorption at these wavelengths greatly aids nonlinear processes such as continuum generation as any absorption will deplete the pulse propagating through the sample and thus limit the irradiance that contributes to the phase change within the sample. This limits the efficiency, and one cannot simply increase the input irradiance in the hope of trying to cancel out the absorption losses as the multi-photon absorption would just get stronger. While multi-photon absorption is a

restriction on nonlinear switching and continuum generation devices it also finds use in femtosecond waveguide inscription and optical limiting devices. In 1999, K. Petkov and P.J.S. Ewen [51] stated that the wavelength dispersion of the linear refractive index could be used to estimate the nonlinear refractive index through equation 2.31:

$$n_2 = \frac{\sqrt{3} g S (n^2 + 2)^{1.5} (n^2 - 1)^2 \hbar^2 e^2}{12 n m E_d {E_0}^2} \qquad \textit{Eq. (2.31)}$$

where S is the oscillator strength, n is the linear refractive index, g is an anharmonicity parameter, m is the mass of an electron, e is the charge of an electron, E_d is the dispersion energy and E_0 is the oscillator energy. Investigations into continuum generation in chalcogenide glass fibres have utilised the same techniques from those used with silica fibres; namely tapering and microstructuring to enhance the overall effective nonlinearity. Many of these advances have been demonstrated by the Centre for Ultrahigh-bandwidth Devices for Optical Systems (CUDOS) in Sydney and the Novel Glass research group at the Optoelectronics Research Centre (ORC) in Southampton.

In 2007 an experiment by E.C. Mägi et. al. [52] tapered down a chalcogenide As_2Se_3 fibre to sub a wavelength diameter. The tapering of the fibre was performed in two stages using the flame-brush technique described earlier for silica fibres; first a multimode fibre core was tapered down from 7.5 μm to 5 μm so that it then only guided a single mode. This uniform tapered section is then tapered further so that a core diameter of 1.2 μm is produced. Figure 2.5 shows a theoretical comparison of the effective nonlinearity between tapered silica fibres and a tapered chalcogenide fibre using appropriate parameters at a wavelength of 1550 nm [52].

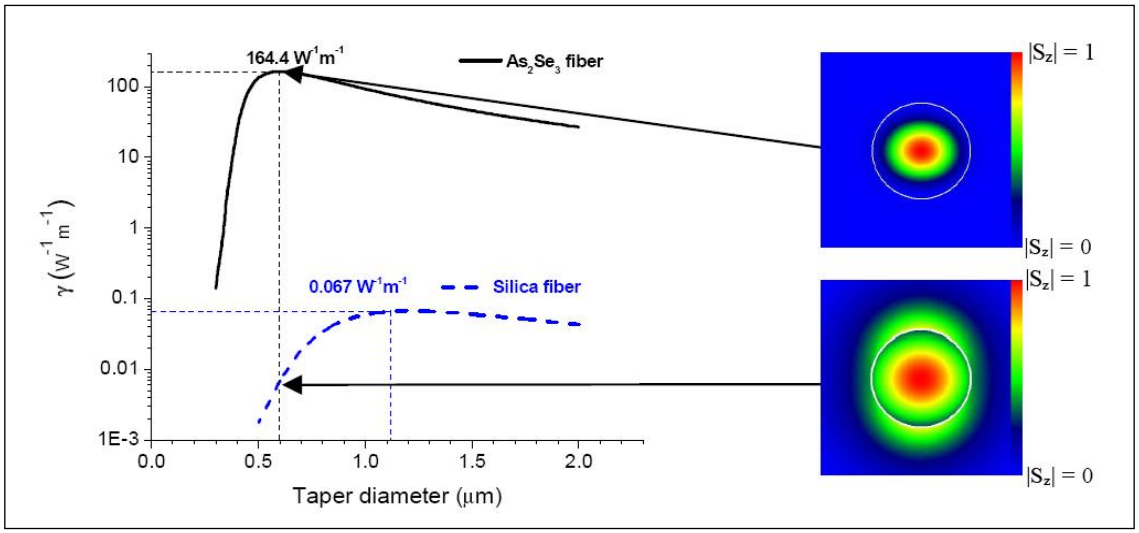

Figure 2.5: Effective nonlinearities of silica and As_2Se_3 fibres for different taper diameters[52].

The peak effective nonlinearity of a tapered As_2Se_3 fibre is predicted to be 2440 times that of a tapered silica fibre. This was due to enhanced mode confinement the higher non-linear refractive index of the chalcogenide glass. The chalcogenide fibre taper was then butt-coupled to a passively modelocked erbium fibre laser. The laser emitted pulses with a central wavelength of 1545 nm with a duration of 1.48 ps and at a repetition rate of 4 MHz. They experimentally measured the tapered fibre's effective nonlinearity, γ, at the pump wavelength to be 68 $W^{-1}m^{-1}$. Despite the considerable contribution of waveguide dispersion the fibre ZDW was greater than that of the pump source. Moderate self-phase modulation was observed for peak pulse powers as low as 4.47 W.

In order for the 1545 nm wavelength erbium fibre laser source to be guided in the anomalous dispersion regime the fibre was tapered further down to a diameter of 0.48 μm. This enhanced the nonlinear pulse propagation properties of the fibre and lowered the supercontinuum generation threshold [53]. The fibre with a 30 mm tapered section length was able to produce a supercontinuum spanning 500 nm when 2.2 pJ pulses with durations of 250 fs were coupled into the fibre. The fibre was estimated to have an effective nonlinearity of approximately 93.4 W^{-1} m^{-1} at the pump wavelength. Figure 2.6 shows the continuum evolution for the average power of the pump input.

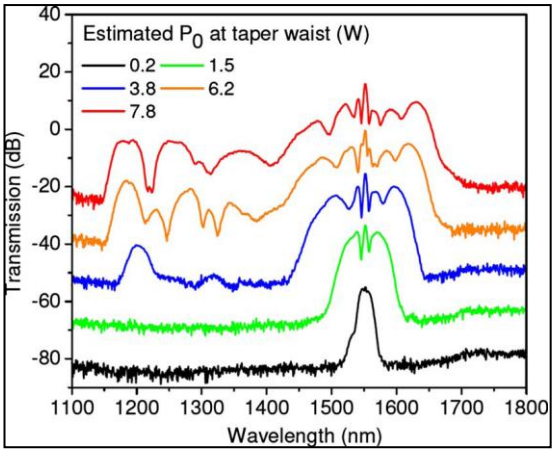

Figure 2.6: Continuum evolution for varying pump power in sub-micron chalcogenide nanowires [53].

Tellurite glasses also have high transmission into the mid infrared and a high nonlinearity, the low wavelength absorption edge translates to a very low multi-photon absorption coefficient in the near infrared [54]. Domachuk et. al. fabricated a tellurite glass PCF and experimentally demonstrated a continuum spanning over 4000 nm from 789-4870 nm [55]. The fibre was designed to have a zero-dispersion wavelength of 1380 nm. The fibre microstructure had a 'wagon wheel' design with a 2.5 μm core. A short 8 mm length of fibre was used to overcome the substantial propagation losses that occur at longer wavelengths. Pulses from a modelocked Ti:Sapphire laser seeded an OPO to generate pulses with a duration of 110 fs, 80 MHz repetition rate and a max average power of 250 mW were used to couple into the fibre. The OPO's output wavelength was centred on 1550 nm where the fibre dispersion was anomalous. Two 40× 0.5NA objectives were used to couple into and out of the fibre, coupling efficiency was found to be ~50%. The nonlinear refractive index of the tellurite glass used was 2.5×10^{-19} m^2W^{-1}, the effective nonlinearity of the fibre was 596 W^{-1} km^{-1}. Figure 2.7 shows the continuum produced with a peak pulse power of 7.95 kW coupled into the fibre.

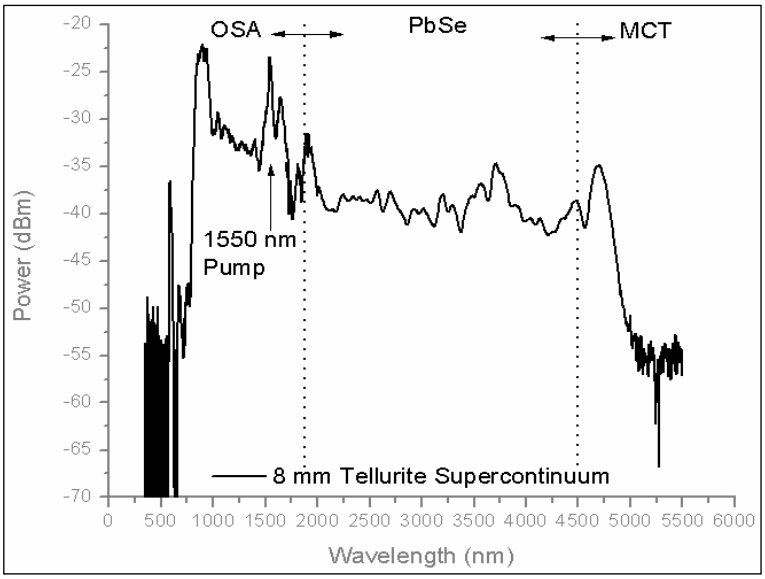

Figure 2.7: Supercontinuum spanning over 4000nm produced by an 8mm length of tellurite fibre [55]

While not as extensively researched as continuum generation in optical fibres, continuum generation in femtosecond inscribed waveguides [56], [57] has also been investigated [58].

Psaila et. al. [58] investigated the spectral broadening characteristics of a ULI waveguide written in the chalcohalide glass, GeS_2-Ga-S_3-CsI. This glass had a nonlinear refractive index ~22 times that of fused silica and a short wavelength absorption edge of 459 nm. Embedded channel waveguides were written into the structure. 'Teardrop' shaped structures were formed in the substrate via this technique. These structures had different guiding regions, ranging from highly multimode to singlemode depending on the position of the input coupling objective. The waveguide selected had been inscribed using 317 nJ pulses and a sample translation speed of 500 μm/s. A spectrally smooth 600 nm wide continuum is produced when 11 μJ pulses are coupled into this highly multimode waveguide. The pulses were 110 fs in duration and had a central wavelength of 1460 nm. Figure 2.8 below shows the continuum generation produced.

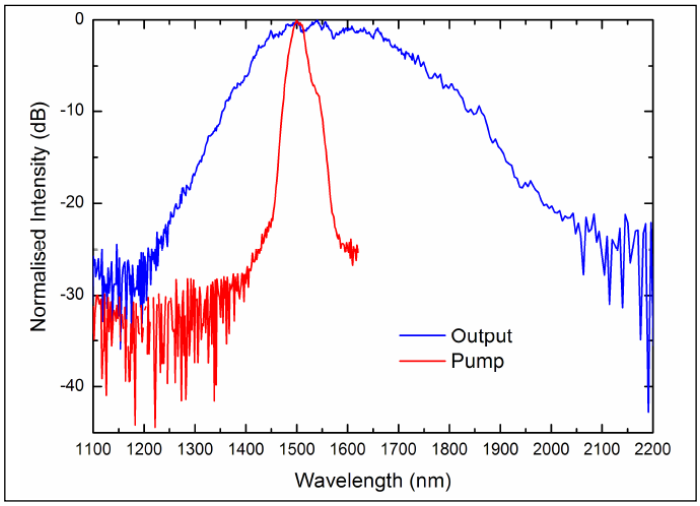

Figure 2.8: Continuum generation in an ultrafast laser inscribed waveguide written in GeS_2-Ga-S_3-CsI [58]

A similar experiment was carried out by Hughes et. al. [59]. Here they investigated the onset of continuum generation in ULI waveguides in gallium lanthanum sulphide. The laser source used to inscribe the waveguides was a regeneratively amplified Ti:Sapphire laser operating with a repetition rate of 250 kHz and with a pulse duration of 130 fs. This pulse train was then focused 400 µm below the substrate surface by a 0.55 NA aspheric lens. By coupling to a structure written with 1.75 µJ pulses and a sample translation speed of 0.2 mm/s they demonstrated spectral broadening with a full width half maximum bandwidth of 200 nm of a pump source with a central wavelength of 1540 nm.

2.6. Femtosecond laser system

The laser system used to investigate nonlinear optical effects throughout this thesis was a regeneratively amplified Ti:Sapphire femtosecond laser system which seeded an Optical Parametric Amplifier (OPA). A schematic of the laser system is shown in Figure 2.9. All the laser systems were manufactured by Spectra-Physics.

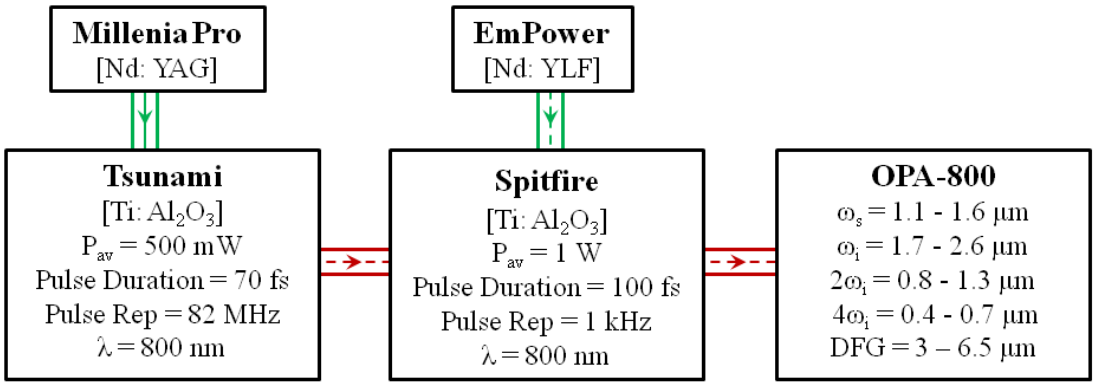

Figure 2.9: Femtosecond optical parametric amplifier pumped by a regeneratively amplified Ti: Sapphire laser system.

A diode-pumped frequency doubled Nd:YAG laser (Millenia Pro) provides a continuous wave output of 5 W at a wavelength of 532 nm. This output is used to optically pump a Ti:Sapphire laser (Tsunami). The laser wavelength of emission can be tuned between 700-900 nm with the use of a dispersive prism and variable filter. The wavelength of emission was set to 800 nm. An intra-cavity Acousto-optic modulator is used to initiate mode-locked operation. When mode-locked, the output pulses from the Tsunami are of the order of 70 fs with a repetition rate of 82 MHz and with an average power of 500 mW.

The femtosecond pulse train from the Tsunami then acts as the seed source for the 'Spitfire' chirped pulse amplification system (CPA). The pump source for the CPA is Q-switched Nd: YLF laser (Empower). For the purposes of pumping the Ti:Sapphire rod within the CPA cavity this was operated at a wavelength of 527 nm, i.e. frequency doubled, with a pulse duration of 300 ns at a repetition rate of 1 kHz and an average power of 7 W.

Before being regeneratively amplified the pulse train is passed through a diffraction grating – dramatically increases the pulse duration and hence decreasing the peak pulse power within the CPA cavity. After amplification the pulses are then compressed by passing them through a grating which has a complimentary dispersion to that of the input grating. At the output of the Spitfire the pulses then have a duration of 100 fs with a repetition rate of 1kHz and an average power of 1W. In terms of pulse energy the input pulses have been amplified from ~ 6 nJ to 1 mJ.

The output of the Spitfire is then directed into an Optical Parametric Amplifier (OPA) system. Upon entering the OPA the input beam is divided into three separate beams; first 1% of the power is tapped off and used to generate a white light continuum by focusing onto a sapphire plate- this acts as a seed pulse. The remaining pump is then split again, 25% of which is spatially and temporally overlapped inside a type-II BBO crystal – this is the pre-amplification stage. The low power seed pulse lowers the threshold for optical parametric generation provided the signal and idler wavelengths generated in the nonlinear crystal are also present in the continuum. The remaining white light is then dumped while the generated signal and idler beams are then passed through the BBO crystal again, this time spatially and temporally overlapped with the remaining pump pulse. This greatly intensifies the amount of power generated in the signal and idler wavelengths – this is the power amplification stage. By tuning the crystal it is possible to generate signal wavelengths between 1100 – 1590 nm and idler wavelengths between 1600-2500 nm. The signal and idler wavelengths can then be separated by a Bragg mirror at the output of the OPA.

Typical un-attenuated output powers were 60 mW and 40 mW for the signal and idler outputs respectively - thus pulse energies of 60 μJ and 40 μJ as the system is running with a pulse repetition rate of 1 kHz. The 1 kHz repetition rate is low enough to avoid the thermal contribution to nonlinear effects.

Further nonlinear conversion of the idler and signal can allow for wavelength generation from 400 to 6500 nm. Second harmonic generation of the idler, $2\omega_i$, by focusing onto a type II- BBO crystal and then collimating allows for a wavelength tuning range of 800 – 1300 nm. This is used in Chapter 4 when investigating continuum generation in silica PCFs. A wavelength range of 400-750 nm is generated by doubling the second harmonic of the idler, i.e. the fourth harmonic of the idler, $4\omega_i$. This arrangement is used in Chapter 5 when investigating polarisation dependent saturable absorption effects of aligned silver nanoparticles. In Chapter 6, mid infrared guiding in chalcogenide glass based waveguides were investigated using the difference frequency of the signal and idler, $\omega_s - \omega_i$. By focusing both onto a Ag-Ga-S crystal a wavelength tuning range of 3000 - 6500 nm could potentially be accessed.

2.7. Summary

The term for a materials intensity dependent refractive index has been derived from the effect of nonlinear polarisation. This nonlinear refractive index was shown to be responsible for the generation of new wavelength components via light-matter interactions. Optical fibres were introduced as a means to improve upon this nonlinear process as they offer interaction lengths, provided that dispersion is managed correctly. A review of previous research in the field of supercontinuum generation in guided media has then presented. This highlighted how different materials and waveguide designs can be implemented to improve the continuum generation, such as tailoring a dispersion profile for a specific wavelength source or pulse duration. Non-silica fibre based materials were introduced and experimental methods outlining how the effective nonlinear index of these fibres could be increased to over 80,000 times that of un-tapered smf-28 optical fibre [Ref 53]. Finally a description of the femtosecond laser system used throughout this thesis was given which highlighted the wide range of pump wavelengths available, this enabled numerous types of fibre and waveguide designs to be investigated.

Chapter 3. Nonlinear optical properties of chalcogenide and tellurite glasses at 1550 nm

3.1. Introduction

The following chapter is an investigation into the third order nonlinearity of several novel chalcogenide and tellurite glasses at the wavelength of 1550 nm. This research was conducted in collaboration with the novel photonic glasses group at Nottingham University. The main aim of the collaborative project was to determine the nonlinear optical switching figure of merit for each glass. Comparison of these measured values to those already existing in literature would give an indication of the suitability of the Nottingham fabricated glasses for optical switching applications. Additionally if a glass with a high optical switching FOM was identified from this study then it would be considered for a substrate material for fabrication of waveguides via ULI - provided high optical quality samples could be repeatedly produced. As the provided chalcogenide samples all contained arsenic, changes would need to be made to the established ULI rig at Heriot-Watt in order to ensure no human contact with airborne particulates. Essentially there would be a trade-off between the materials nonlinearity, optical quality and the required safety requirements when selecting the most appropriate material. Therefore two other materials, zinc selenide and gallium lanthanum sulphide, were also investigated to determine their suitability for inscription. The aim of the ULI is to develop compact photonic devices.

As mentioned in Chapter 2, chalcogenide glasses exhibit high nonlinear refractive indices and low nonlinear absorption. These make them attractive materials for nonlinear optical switching devices, such as a Kerr shutter [60] as the high nonlinear refractive index will allow for a high phase change per unit length. Multi-photon absorption limits the effectiveness of a nonlinear optical switching device as the material absorbs energy from the pulse and thus limits the interaction length and phase change within the device. A typical figure-of-merit (FOM) for optical switching devices can be defined as in equation 3.1:

$$FOM = \frac{n_2}{2\beta\lambda} \qquad \textit{Eq. (3.1)}$$

where β is the nonlinear absorption coefficient with units of mW^{-1} and λ is the wavelength of the incident light in nm. The nonlinear absorption term arises due to the fact that the nonlinear susceptibility tensor, $\chi^{(3)}$, is complex:

$$\chi^{(3)} = \chi_R^{(3)} + i\chi_I^{(3)} \qquad \textit{Eq. (3.2)}$$

The extent of absorption as light passes through a sample can be expressed as:

$$\frac{dI}{dz} = \alpha(I).I \qquad \textit{Eq. (3.3)}$$

where *α(I)* is the intensity dependent absorption, which can be expressed as;

$$\alpha(I) = \alpha + \beta I + \gamma I^2 + \cdots \qquad \textit{Eq. (3.4)}$$

Considering only the two-photon absorption term, *β,* the above expression for absorption can be expressed as:

$$I = I_0 e^{(-\beta I_0 Z)} \qquad \textit{Eq. (3.5)}$$

where I_0 is the incident intensity, and *z* is the sample thickness, this is similar to the single photon absorption term but dependent on intensity. For a thin sample the amount of absorbed light can therefore be expressed as:

$$I_0 - I = \beta I_0^2 z \qquad \textit{Eq. (3.6)}$$

Equation (3.6) above shows that the two-photon absorption term varies quadratically with irradiance whereas one photon absorption varies linearly. Nonlinear absorption can

be used for 3D sample imaging, micro-fabrication and optical limiting; however it also limits the efficiency of certain types of optical switches which rely on the nonlinear refractive index of a material.

3.2. Z-Scan experimental technique

The z-scan experimental technique [61] allows for the sensitive measurement of the nonlinear absorption and the nonlinear refractive index of a material. The basis of the z-scan experiment is simple; the test sample is translated through the beam waist of a focused beam, while continually monitoring the transmittance in the far-field. When far from focus the power per unit area is low and the absorption and refraction of the sample are due to linear effects which give a non-varying transmittance. In and around the focal plane there will be a much higher irradiance – thus the materials nonlinear properties will affect the properties of the beam. The change in aperture transmittance of a Gaussian beam as a material with a positive nonlinear refractive index is translated through the focal plane is highlighted in figure 3.1.

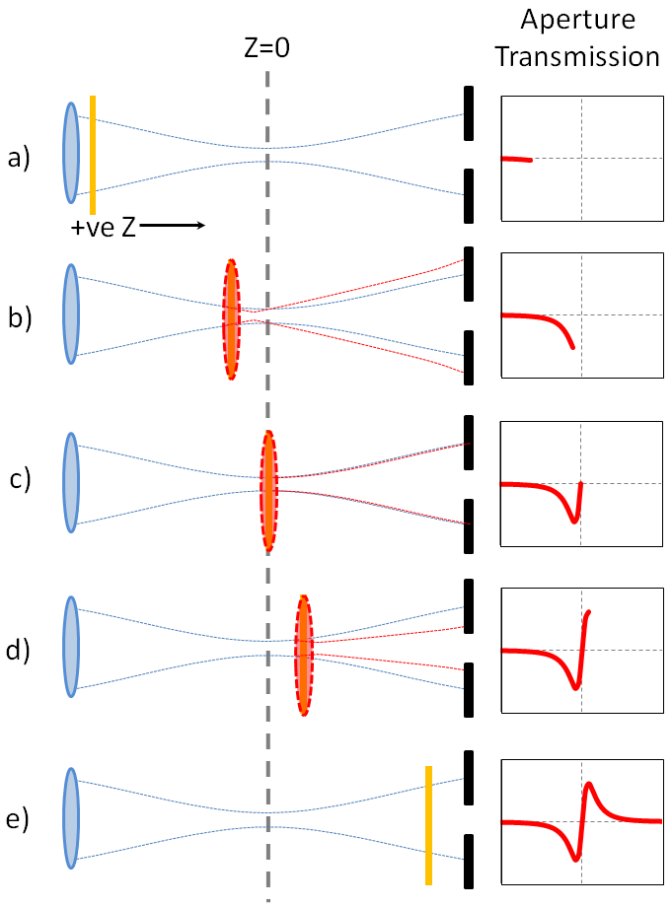

Figure 3.1: Translation of a material with a positive nonlinear refractive index inducing an aperture transmission change as it is scanned through the focus of an intense laser beam.

As the sample approaches the focal plane, a sample with a positive non-linear refractive index, will induce a self-focusing effect onto the beam (Kerr lensing), causing the beam to focus earlier and become more divergent in the far-field. This effect becomes stronger the closer the sample is to the focus. If an aperture that is smaller than the beam cross-section is placed infront of the detector and centred on axis then this divergence will lead to a drop in transmittance. Then as the sample is moved immediately past the focal point, collimation of the beam occurs, which will lead to an increase in transmittance as more light will be able to pass through the aperture. Far behind the focus of the beam, the irradiance once again lowers, and only linear effects are observed. Therefore, a material with a positive nonlinear refractive index will produce a z-scan trace with a distinct drop in transmittance, followed by a peak in transmittance as the sample is passed through the focus. A material with a negative refractive index will yield a z-scan trace of a peak followed by a trough as it is scanned through the focus.

This variation will be symmetric about the focus provided there is no nonlinear absorption. Therefore, the sign and magnitude of a materials non-linear refractive index can be readily obtained from a z-scan trace. This is known as a ‘closed aperture scan’.

The effect of nonlinear absorption can be observed either by removing the aperture in-front of the detector, or adding in a beam-splitter to tap off a small amount of the signal to a second detector without an aperture. This detector, the open aperture detector, is insensitive to the effects of nonlinear refraction and thus only effects relating to nonlinear absorption will affect the measured transmittance. The open aperture z-scan trace for a sample that exhibits nonlinear absorption will be a symmetric trough with the point of minimum transmission in the focal plane. This arrangement is demonstrated in figure 3.2, here a sample with a positive nonlinear refractive index has been translated through the focus of a laser pulse train. The microscope slide allows for simultaneous capture of nonlinear absorption and nonlinear refractive index effects.

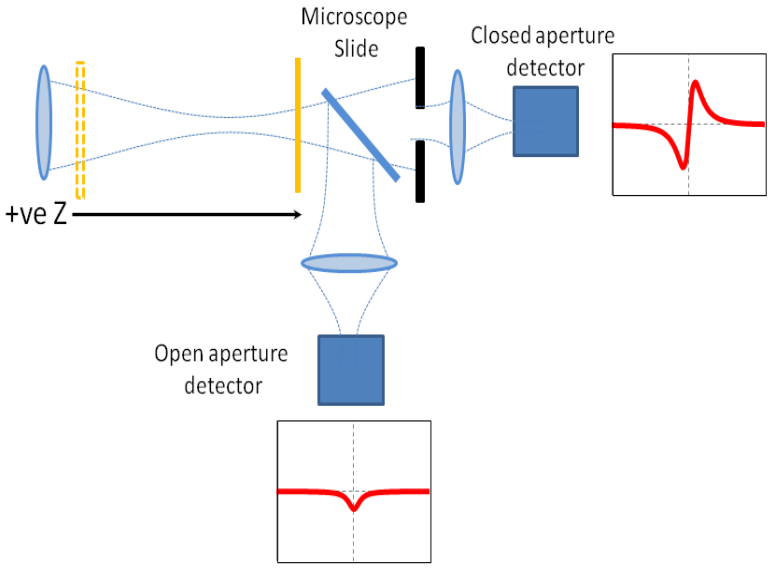

Figure 3.2: Schematic of open and closed aperture z-scan data capture. A material with a positive nonlinear refractive index has been translated through z. The effect of nonlinear absorption is observed on the open aperture detector.

The z-scans can clearly show the effects of non-linear refraction and absorption, but in order to obtain the magnitude of the non-linear coefficients theoretical fits must be applied to the collected data. This can be done in a number of ways and two fitting methods will be outlined below.

For small phase changes ($|\varphi_0|<<1$) then simplified empirical equations can be used to obtain a value for the nonlinear coefficients. Such simplified formulae for the open aperture transmission with sample position, $T_{open}(z)$, and the closed aperture transmission with sample position, $T_{closed}(z)$, take the form of equations 3.7 and 3.8 [62].

$$T_{open}(z) = 1 - \frac{\beta I_0 L}{2\sqrt{2(1+x^2)}} \qquad \textit{Eq. (3.7)}$$

$$T_{closed}(z) \cong 1 + \frac{4x(\Delta\emptyset_0)(1-S)^{0.25}}{(1+x^2)(9+x^2)} \qquad \textit{Eq. (3.8)}$$

where $x=z/z_0$, where z is the sample distance and $z_0=\pi\omega_0^2/\lambda$, where ω_0 is the beam radius at focus. S is the aperture transmission, I_0 is the peak on-axis intensity, $\Delta\phi_0$ is the time-averaged on-axis phase change and is defined by the equation:

$$\Delta\emptyset_0 = \frac{2\pi L n_2 I_0}{\lambda\sqrt{2}} \qquad \textit{Eq. (3.9)}$$

A materials nonlinear refractive index coefficient can be calculated by varying the n_2 parameter in equation 3.8 until the experimental data and the theoretical fit show agreement. Likewise a materials two-photon absorption co-efficient can be calculated by varying the β term in equation 3.7. Such fits require the data to be shifted so as to be symmetric about the axis and symmetric about the focus. When trying to determine nonlinear refractive of a material using this fitting method, no multi-photon absorption effects can be present on the closed aperture z-scan.

In order to accurately model the effects of nonlinear absorption and nonlinear refraction from a single z-scan a Fast Fourier Transform Beam Propagation Method FFT-BPM [63] can be used. The FFT-BPM divides the sample into a number of thin 'slices', each of which are then treated as a thin lens. The strength of each lens is determined by the *slice* nonlinearity. It calculates the nonlinear effects by considering the beam size and radius of curvature as the light is incident, passes through and exits each slice. There are a number of important experimental parameters to record when fitting z-scan traces. For

example the pulse duration, pulse energy and focusing spot size used to calculate the irradiance at focus. When fitting with the empirical formula the aperture transmission value is used. In the case of curve fitting with the BPM the aperture diameter and the distance from the aperture to the focal plane need to be measured. Additionally the test sample thickness must be less than the Rayleigh range of the beam for thin lens approximations to hold.

3.3. Experimental set-up

The BBO crystal in the OPA was tuned to give a signal wavelength of 1550 nm. The signal is heavily attenuated from 60 µJ to 2 µJ by placing a neutral density filter at the output port, an RGA850 filter was also inserted into the beam path to remove any unwanted residual light that may have been co-propagating with the signal beam.

The experimental configuration is shown below in Figure 3.3. After passing through the ND and RGA850 filters the beam is directed by two silver coated mirrors, M1 and M2, through a spatial filter. The spatial filter consists of two 200 mm focal length achromatic doublets placed 2-*f* apart either side of a 200 µm diameter diamond pinhole which is mounted on an x, y stage. The pinhole is held under vacuum to eliminate the creation of plasma which could occur at the focus. The spatial filter is used to ensure the laser beam profile was as close to a pure Gaussian distribution as possible. This filtering process typically reduces the laser power by 40%.

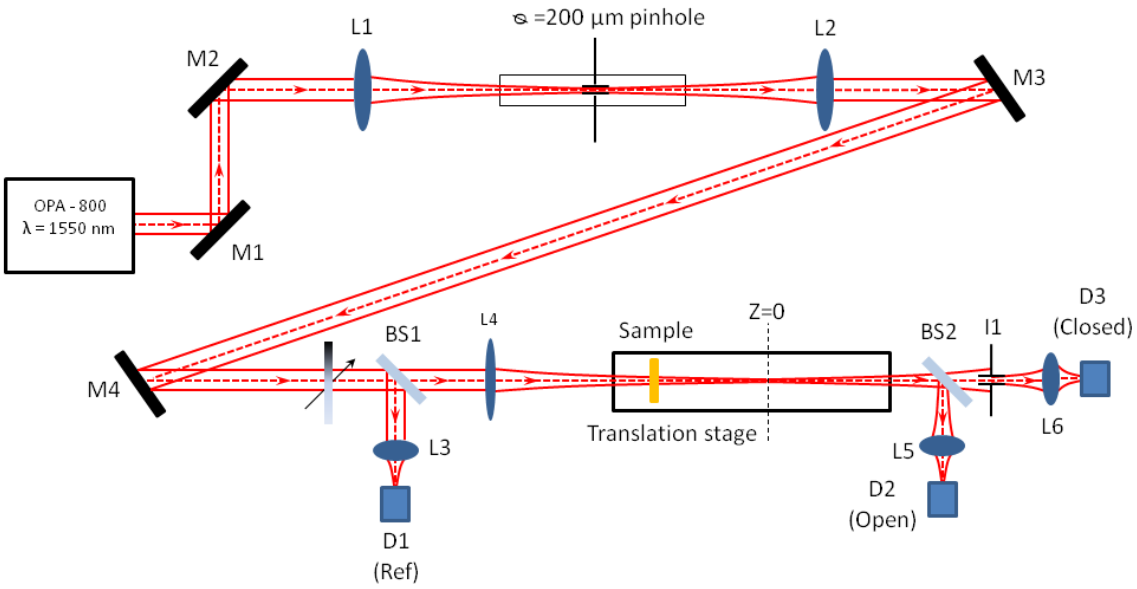

Figure 3.3: Z-scan experimental set-up

After passing through the spatial filter the laser beam is then directed by mirrors M3 and M4, through two irises (not shown in figure 3.3) to ensure that the beam path is 'on-axis' and co-linear with that of the translation of the test sample. A beam splitter, BS1, taps off ≈3% of the laser signal before being focussed onto a photodiode, D1, which allowed for a reference level reading. The remaining 97% of the un-deflected signal was then focused by an anti-reflection (AR) coated convex silica lens which had a focal length of 300 mm. L4 is the lens used to focus the radiation for the actual z-scan measurement. The focal spot size of L4 was measured using the scanning knife-edge technique and was calculated to be 37µm. Another beam-splitter, BS2, taps off approximately 3% of the signal before being focussed onto a photodiode, D2, which is the detector used to measure the amount of nonlinear absorption, i.e. the open aperture detector. The remaining un-deflected signal was then passed through a variable aperture, I1, mounted onto an x, y translation stage before being focused onto photodiode, D3, this detector allowed for measurement of the nonlinear refraction of a test sample.

All photodiodes in this set-up were New Focus (model 2033) germanium detectors. These detectors were triggered from the signal used to switch the Pockels cells inside the RGA. The signals from each detector are amplified and then fed through a peak-hold unit and then connected to a data acquisition card and PC. The detectors were

found to have a linear response up to 1.1 V. Combinations of neutral density (ND) filters were placed in front of each detector so that their signal levels were well below 800 mV for each z-scan measurement. A variable ND filter was placed between M4 and BS1 to allow for fine adjustment of the incident power onto the sample, this was measured by an InGaAs low power meter (Newport 980-IG) connected to universal power meter (Newport 1930c). The sample was mounted on a translation stage (Newport UTM 150) which was connected to a Newport MM005 motion controller.

An HP-VEE program was used to control the stage movement and decrease the error for each recorded value from the open and closed aperture detectors. A reference and plus-minus value is set for D1. For each stage position a set number, e.g. 100, measurements of the reference level and corresponding open and closed detector signal levels are made. If a percentage of these values, e.g. 10%, lie outside the error window for the reference then the measurements are discounted. The process repeats until the windowing conditions are met. At this point the mean values of the ref, open and closed detectors are recorded along with the current z-position and saved to a text file. The stage then moves the sample a set distance to the next position. Windowed collection of data occurs again at this particular stage position. This process continues until a 'stop' command is entered at the program interface.

3.4. Chalcogenide and tellurite glass sample compositions

The chalcogenide and tellurite glass samples were provided by Nottingham University. The chalcogenide glass samples were made by sealed ampoule melting in a rocking furnace by first weighing and mixing the high purity powders inside a glove box. The compound mixtures were then transferred to silica glass ampoules which had been air and vacuum baked prior to use. The ampoules were sealed under vacuum at a pressure of 10^{-5} mBar and placed in a rocking furnace. To fabricate the As-S-Se chalcogenides glass samples the furnace temperature was increased at 30 °C per hour before holding the temperature at 250 °C for 2 hours. The furnace was then rocked as the temperature was heated further, again at a rate of 30 °C per hour, until the temperature reached 650 °C. The furnace then maintained this temperature for 12 hours to achieve homogenization. The samples were then cooled at a rate of 60 °C per hour before being

held vertically to refine the glasses at a temperature of 570 °C. The ampoules were then quenched using a jet of nitrogen and then annealed at the glass transition temperature. The tellurite glass samples were fabricated by via the melt quenching technique. The annealed glasses were then diced into thin samples and polished to allow for optical characterisation. The glass compositions are summarised in Table 3.1 where the samples have been divided into sub-sets. The first sub-set contains chalcogenides made up of the As-S-Se composition and studies how the nonlinearity varies as higher concentrations of sulphur are added to the glass composition at the expense of selenium. The second glass system investigated had the composition As-Se-Te. Here the study focuses on the nonlinear effects of added increasing concentrations of tellurium at the expense of selenium. The third chalcogenide system investigated consisted of the Ge-As-Se-Te quaternary glass compound. The two tellurite systems investigated are made up of K_2O-TeO_2 and Na_2O-TeO_2 glass compositions.

As-S-Se System	As-Se-Te System	Ge-As-Se-Te System	K_2O-TeO_2 System {mol %}	Na_2O-TeO_2 System {mol %}
$As_{40}Se_{60}$	$As_{30}Se_{70}$	$Ge_{17}As_{18}Se_{56}Te_7$	{10}K_2O-{90}TeO_2	{10}Na_2O-{90}TeO_2
$As_{40}Se_{45}S_{15}$	$As_{30}Se_{67}Te_3$	$Ge_{15}As_{15}Se_{17}Te_{53}$	{15}K_2O-{85}TeO_2	{15}Na_2O-{85}TeO_2
$As_{40}Se_{40}S_{20}$	$As_{30}Se_{60}Te_{10}$	-	{20}K_2O-{80}TeO_2	{20}Na_2O-{80}TeO_2
$As_{40}Se_{50}S_{30}$	$As_{30}Se_{50}Te_{20}$	-	-	-
$As_{30}Se_{30}S_{40}$	$As_{30}Se_{40}Te_{30}$	-	-	-
$As_{40}Se_{15}Se_{45}$	$As_{30}Se_{30}Te_{40}$	-	-	-
$As_{40}S_{60}$	-	-	-	-

Table 3.1: Chalcogenide and tellurite glass compositions

3.5. As-S-Se chalcogenide system

3.5.1. $As_{40}Se_{60}$

Figure 3.4 shows a normalised closed aperture z-scan curve fits for $As_{40}Se_{60}$ sample with incident pulse energies of 20 and 40 nJ, the theoretical traces were plotted with a nonlinear refractive index coefficient of 1.05×10^{-17} m^2W^{-1}. The aperture transmission was set to 20%. The focusing spot size was 35 µm. The sample thickness was 640 µm.

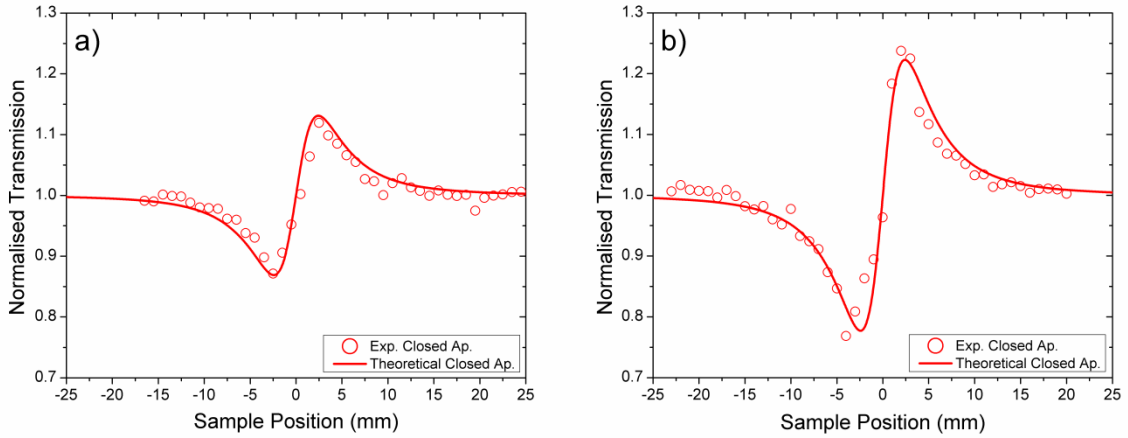

Figure 3.4: Closed aperture z-scan trace conducted on $As_{40}Se_{60}$ with pulse energies of (a) 20 nJ and (b) 40 nJ. Theoretical fits were calculated using an n_2 coefficient of 1.05×10^{-17} m^2W^{-1}.

As the pulse energy was increased stronger nonlinear absorption effects were observed on the open aperture trace. A nonlinear absorption coefficient of 2.8×10^{12} mW^{-1} was calculated by fitting to the experimental data from z-scans conducted with pulse energies of 50 nJ and 120 nJ. These z-scan traces are shown in figure 3.5 (a) and (b) respectively.

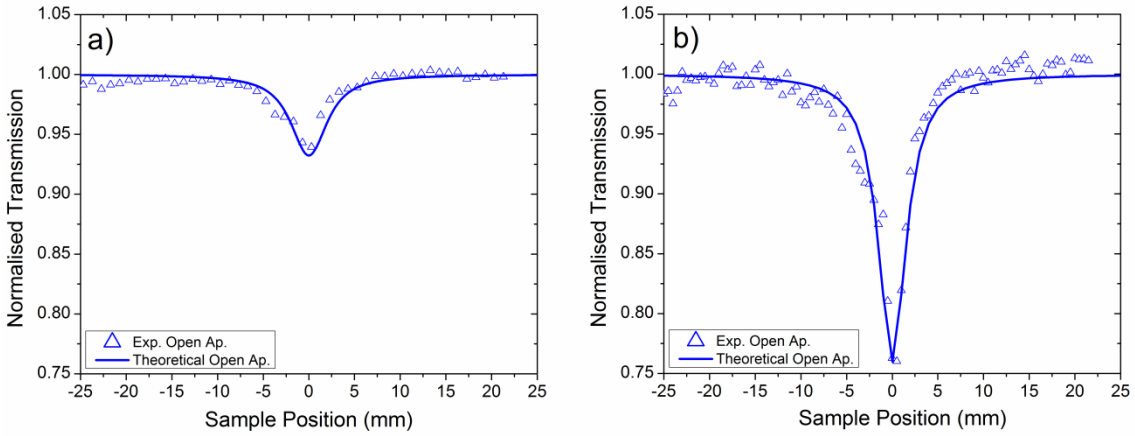

Figure 3.5: Open aperture z-scan trace conducted on $As_{40}Se_{60}$ with pulse energies of (a) 50 nJ and (b) 120 nJ. Theoretical fits were calculated using an nonlinear absorption coefficient of 2.8×10^{-12} mW^{-1}.

3.5.2. $As_{40}S_{60}$

The $As_{40}S_{60}$ sample was found to have a much lower nonlinear refractive index in comparison to that of $As_{40}Se_{60}$, but also a significantly lower nonlinear absorption coefficient. Figure 3.6 shows closed aperture z-scan traces with incident pulse energies of 59 and 100 nJ which were fitted with a NLR coefficient of 2.25×10^{-18} m^2W^{-1} and 2.5×10^{-18} m^2W^{-1} respectively. The aperture transmission was 34% and the sample thickness was 700 µm.

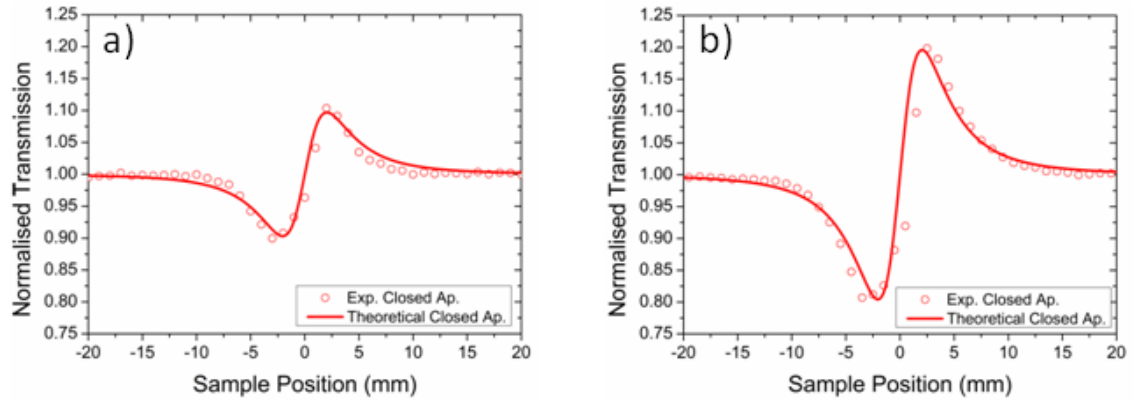

Figure 3.6: Closed aperture z-scan trace conducted on $As_{40}S_{60}$ with pulse energies of (a) 59 nJ and (b) 100 nJ. Theoretical fits were calculated using an n_2 coefficient of 2.25×10^{-18} m^2W^{-1} and 2.5×10^{-18} m^2W^{-1} respectively.

Nonlinear absorption effects were observed for incident pulse energies of 150 nJ, which corresponded to an irradiance of 38 GW/cm^2, fitting the theoretical open aperture curve

to the experimental data yielded a nonlinear absorption coefficient of 5.3×10^{-13} mW^{-1}. Figure 3.7 shows the two z-scans conducted on $As_{40}S_{60}$ with the pulse energies of 150 and 200 nJ.

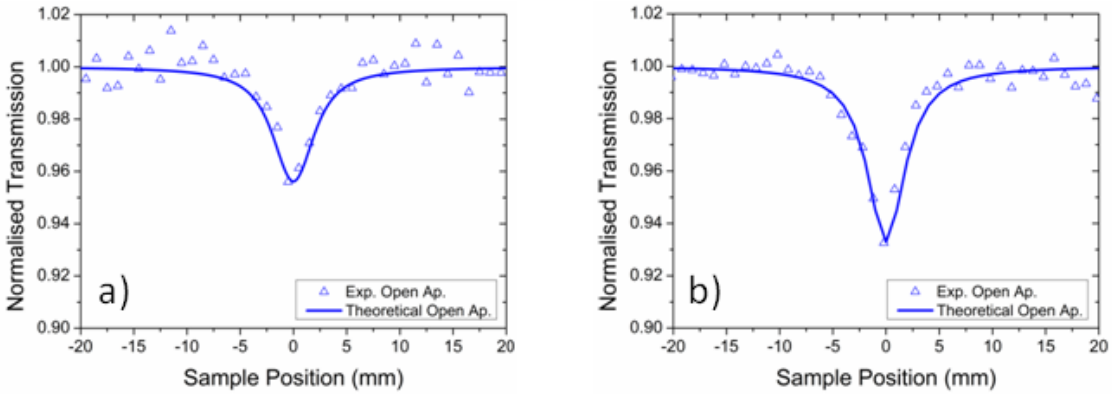

Figure 3.7: Open aperture z-scan trace conducted on $As_{40}S_{60}$ with pulse energies of (a) 150 nJ and (b) 200 nJ. Theoretical fits were calculated using an nonlinear absorption coefficient of $5.3\times10^{-13}mW^{-1}$.

3.5.3. $As_{40}S_{15}Se_{45}$, $As_{40}S_{20}Se_{40}$, $As_{40}S_{30}Se_{30}$, $As_{40}S_{40}Se_{20}$, $As_{40}S_{45}Se_{15}$

The effects of increasing concentrations of sulphur at the expense of selenium in the As-S-Se composition to the magnitude of the nonlinear refractive index are presented in figure 3.8 (a) – (e) and summarised in 3.8 (f). Figure 3.8 (a) shows a closed aperture z-scan conducted on $As_{40}S_{15}Se_{45}$ with pulse energies of 50 nJ and with an aperture transmission of 0.34. This was fitted with a nonlinear refractive index coefficient of 6.1×10^{-18} m^2W^{-1}. This corresponds to a 43% reduction in n_2 from that of $As_{40}Se_{60}$. The nonlinear refractive index coefficient of $As_{40}S_{20}Se_{40}$ was found to be comparable to that of $As_{40}S_{15}Se_{45}$. The experimental z-scan data were fitted with an n_2 of 6.0×10^{-18} m^2W^{-1}, one plot of which is shown in figure 3.8 b) for pulse energies of 25 nJ and an aperture transmission of 34%. As the chalcogenide glass composition is changed to $As_{40}S_{30}Se_{30}$ the nonlinear refractive index decreases to 4.5×10^{-18} m^2W^{-1}, a z-scan trace conducted on $As_{40}S_{30}Se_{30}$ with pulse energies of 55 nJ and an aperture transmission of 34% is shown in figure 3.8 (c). Z-scans conducted on $As_{40}S_{40}Se_{20}$ again showed a reduction in the nonlinear refractive index and were fitted with a n_2 coefficient of 3.6×10^{-18} m^2 W^{-1}, one such z-scan is shown in figure 3.8 (d) and shows a closed aperture trace with incident pulse energies of 48 nJ and an aperture transmission of 34%. The smallest measured n_2

for this sub-set was found for the composition of $As_{40}S_{45}Se_{15}$, for which a nonlinear refractive index coefficient of $2.3\times10^{-18}m^2W^{-1}$ was obtained, this is approximately 37% of that measured for $As_{40}S_{15}Se_{45}$. Figure 3.8 (e) shows a z-scan conducted on $As_{40}S_{45}Se_{15}$ pulse energies of 55 nJ and an aperture transmission of 34%. Figure 3.8 (f) gives the sample compositions, thickness and their measured n_2 coefficients. The error in the n_2 values were calculated by combining the experimental errors that would yield the highest focal irradiance (equation 3.9) and then fitting this theoretical curve to the experimental data.

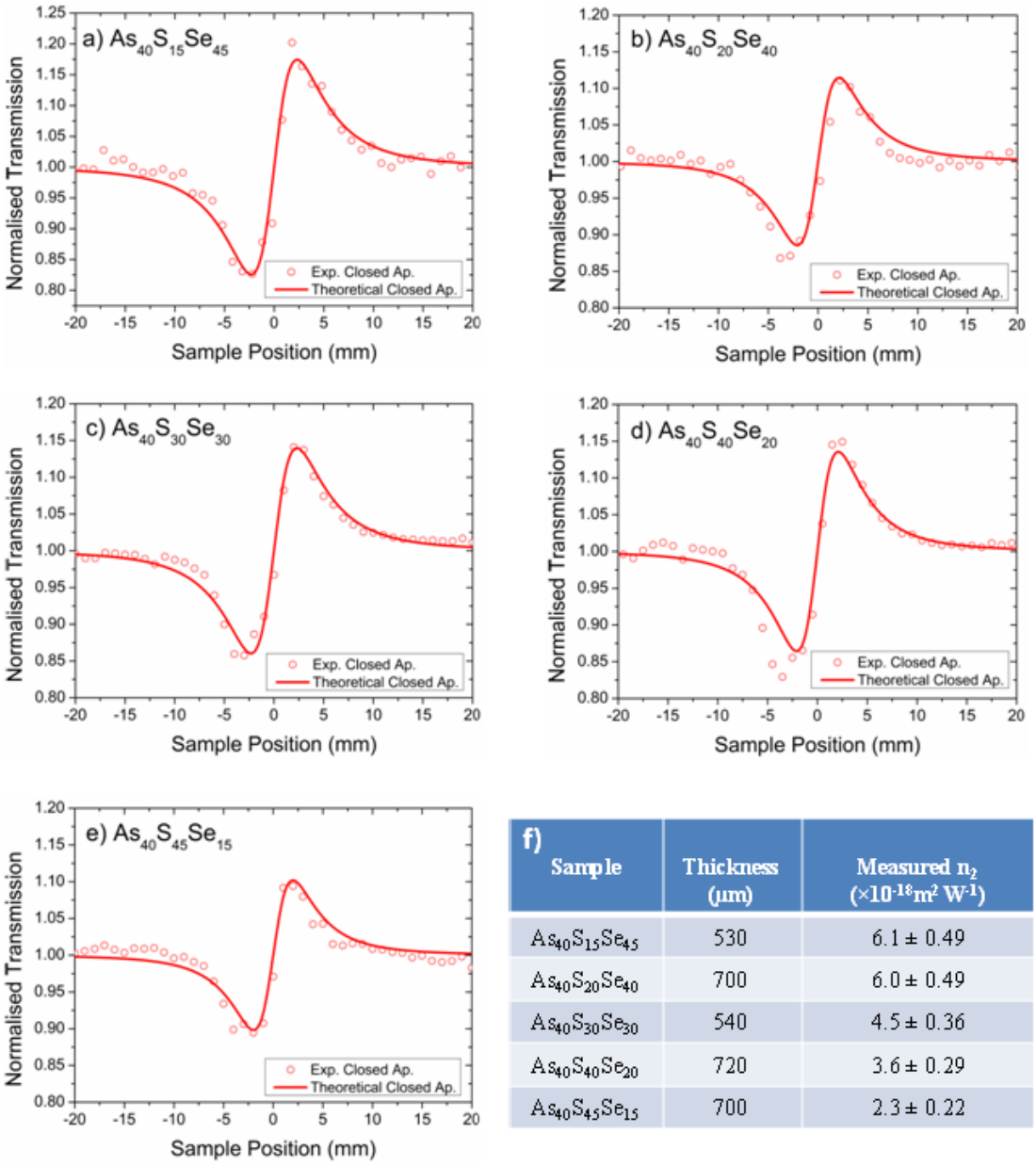

f) Sample	Thickness (μm)	Measured n_2 ($\times10^{-18}m^2W^{-1}$)
$As_{40}S_{15}Se_{45}$	530	6.1 ± 0.49
$As_{40}S_{20}Se_{40}$	700	6.0 ± 0.49
$As_{40}S_{30}Se_{30}$	540	4.5 ± 0.36
$As_{40}S_{40}Se_{20}$	720	3.6 ± 0.29
$As_{40}S_{45}Se_{15}$	700	2.3 ± 0.22

Figure 3.8: (a) – (e) Show closed aperture z-scan traces conducted on varying compositions of the As-S-Se chalcogenide glass system. (f) Shows the calculated n_2 coefficients used to fit the theoretical curves to the experimental data.

The nonlinear absorption coefficients of the samples were also investigated. Nonlinear absorption effects were observed in these samples when the incident pulse energy was increased to around 100 nJ. Figure 3.9 (a) shows an open aperture z-scan conducted with pulse energies of 125 nJ on $As_{40}S_{15}Se_{45.}$ Figure 3.9 (b) shows an open aperture z-scan conducted with pulse energies of 200 nJ on $As_{40}S_{20}Se_{40}$. Figure 3.9 (c) shows an open aperture z-scan conducted on $As_{40}S_{30}Se_{30}$ with pulse energies of 200 nJ. Figure 3.9 (d) shows an open aperture z-scan conducted on $As_{40}S_{40}Se_{20}$ with pulse energies of 200 nJ and figure 3.9 (e) shows an open aperture z-scan trace conducted on $As_{40}S_{45}Se_{15}$ with pulse energies of 130 nJ. Figure 3.9 (f) gives the sample compositions, thickness and their measured β coefficients. The error in the β values were calculated by combining the experimental errors that would yield the highest focal irradiance (equation 3.9) and then fitting this theoretical curve to the experimental data.

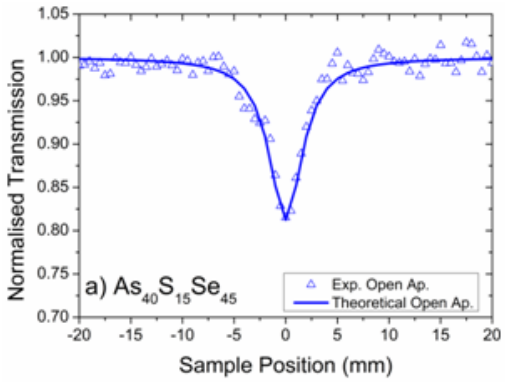

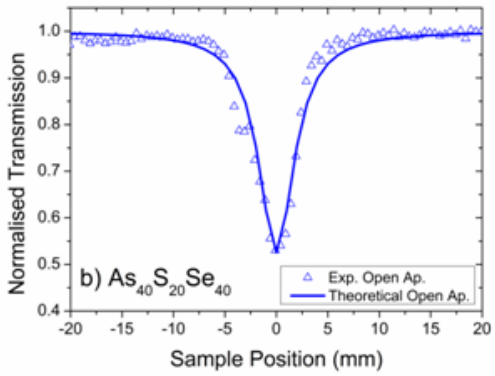

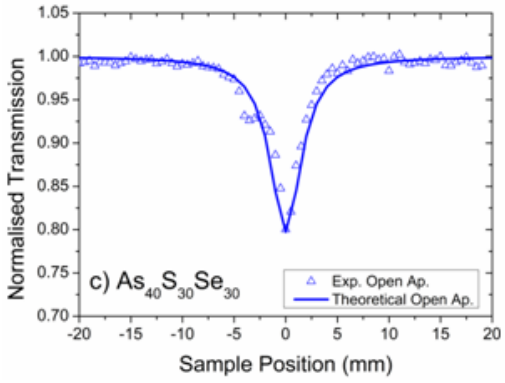

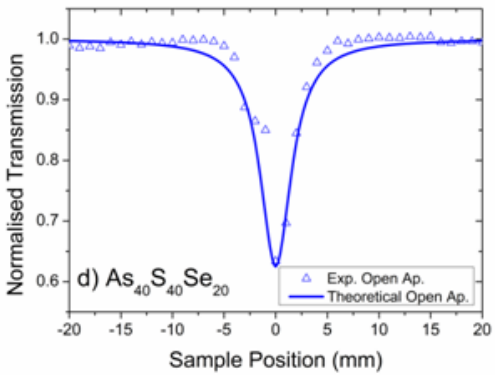

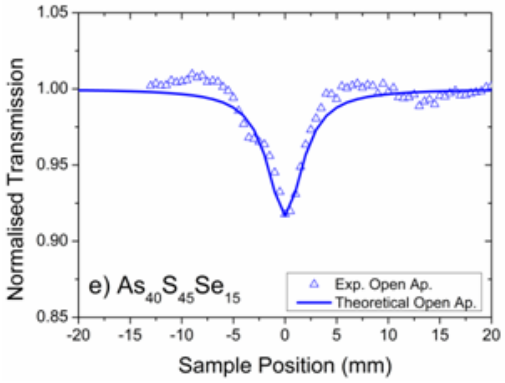

f) Sample	Thickness (μm)	Measured β ($\times 10^{-12}$ m W^{-1})
$As_{40}S_{15}Se_{45}$	530	2.8 ± 0.23
$As_{40}S_{20}Se_{40}$	700	3.7 ± 0.29
$As_{40}S_{30}Se_{30}$	540	2.0 ± 0.16
$As_{40}S_{40}Se_{20}$	720	2.7 ± 0.23
$As_{40}S_{45}Se_{15}$	700	1.0 ± 0.11

Figure 3.9: (a) – (e) show open aperture z-scan traces conducted on varying compositions of the As-S-Se chalcogenide glass system. (f) Shows the calculated nonlinear absorption coefficients used to fit the theoretical curves to the experimental data

A linear reduction in the nonlinear refractive index is observed for decreasing concentrations of selenium in the As-S-Se glass composition. The nonlinear absorption trend also shows a linear reduction with decreasing concentrations of selenium, however the glass compositions $As_{40}S_{20}Se_{40}$ and $As_{40}S_{40}Se_{20}$ lay out with this trend by exhibiting a much higher nonlinear absorption. The nonlinear refraction and absorption coefficients obtained for $As_{40}S_{(60-x)}Se_x$ are shown in figure 3.10.

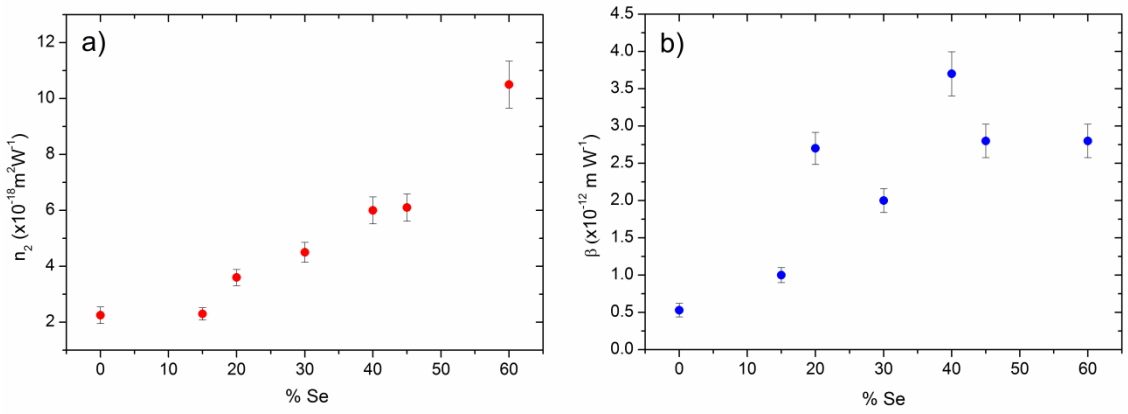

Figure 3.10: Shows trends for (a) nonlinear refractive index and (b) nonlinear absorption coefficients for the investigated $As_{40}S_{(60-x)}Se_x$ chalcogenide glass composition.

The increase in the nonlinear refractive index for percentage increase of selenium in the $As_{(40)}$-$S_{(60-x)}$-$Se_{(x)}$ system agrees with data obtained by Harbold et. al. [64]. However, the values calculated here are approximately 55% lower than those measured in their study. They also observed a similar 'spike' in nonlinear absorption coefficient for the $As_{40}S_{20}Se_{40}$ glass composition but not in the $As_{40}S_{40}Se_{20}$ glass composition. Both this study and that conducted by Harbold et. al. show an opposite trend in the nonlinear refractive index for the $As_{(40)}$-$S_{(60-x)}$-$Se_{(x)}$ system than that measured by T. Cardinal et. al. [65]. In this study the value the nonlinear refractive index of $As_{40}Se_{60}$ was measured to be 1.05×10^{-17} m^2W^{-1}, this is within the experimental error of the theoretically predicted value [66] and matches that of previous experimentally measured values [67-69]. Whereas in ref. [65] the value obtained for $As_{40}Se_{60}$ was less than half of the value measured here. This demonstrates how sample quality and fabrication conditions can affect the nonlinearity of the glass. As the nonlinear optical coefficients of $As_{40}S_{60}$ are well characterised at a wavelength of 1550 nm, therefore the z-scans obtained from this glass composition were used as a reference in determining the nonlinear characteristics of the other glass compositions and the validating the experimental set-up/procedure. The values obtained here for the nonlinear absorption coefficient of $As_{40}S_{60}$ match those measured elsewhere [70, 71], this adds further weight to the values/trends calculated here for the other As-S-Se glass compositions and the quality of Nottingham Universities fabrication facilities and methods.

3.6. As-Se-Te chalcogenide system

This chalcogenide group is investigated to examine the effect of increasing tellurium concentration at the expense of selenium in the As-Se-Te chalcogenide glass system. Five samples were investigated; the concentration of arsenic was fixed at 30% for each of these samples. The nonlinear optical properties of $As_{30}Se_{70}$ were also investigated. There is a red-shift in the short wavelength absorption edge for glasses for increasing tellerium concentration, consequently the glasses with large Te concentrations exhibited large nonlinear absorption coefficients. Nonlinear absorption effects were observed in samples with greater than 20 weight per cent of tellurium with pulse energies of 2 nJ, this corresponded to an irradiance at focus of 0.43 GW/cm^2. In the case of the $As_{30}Se_{30}Te_{40}$ glass composition the investigated wavelength of 1550 nm actually lies on the absorption edge of the sample.

Figure 3.11 shows the calculated nonlinear refractive index and nonlinear absorption coefficients for $As_{30}Se_{(70-x)}Te_x$ glass compositions. As can be seen the nonlinear absorption coefficient greatly increases as the tellurium concentration is increased. A nonlinear absorption coefficient of 1.7×10^{-12} mW^{-1} was calculated for $As_{30}Se_{70}$ and the nonlinear refractive index coefficient was calculated to be 4.5×10^{-18} m^2W^{-1}. These were the lowest measured in this chalcogenide group. Although samples such as $As_{30}Se_{40}Te_{30}$ exhibited a large nonlinear refractive index coefficient of 4.3×10^{-17} m^2W^{-1}, the dominance of multiphoton absorption at 1550 nm for this group of chalcogenides makes them unappealing for base materials in photonic switching devices.

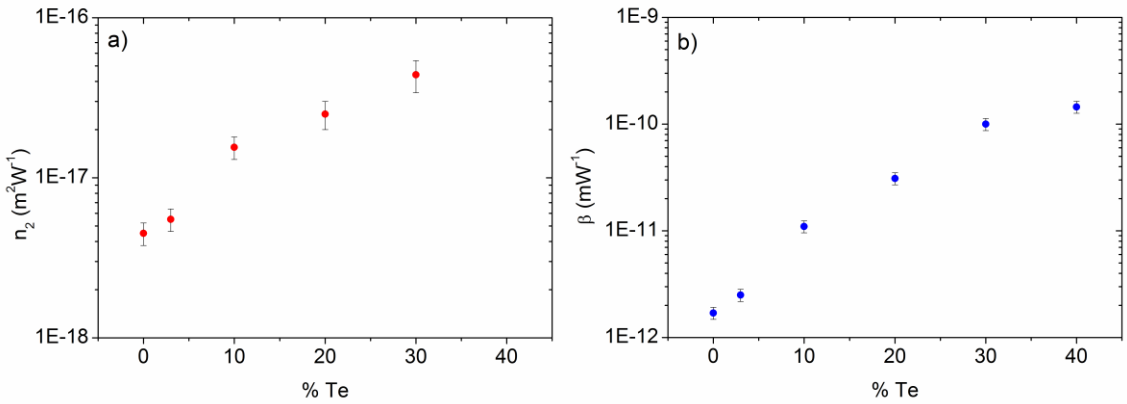

Figure 3.11: Shows trends for (a) nonlinear refractive index and (b) nonlinear absorption coefficients for the investigated $As_{30}Se_{(70-x)}Te_x$ chalcogenide glass composition.

3.7. Ge-As-Se-Te chalcogenide system

Similar to the investigation carried for the As-S-Se and As-Se-Te glass systems, this investigation compared the nonlinear optical coefficients of the quaternary Ge-As-Se-Te chalcogenide glass, namely the $Ge_{17}As_{18}Se_{56}Te_9$ and $Ge_{15}As_{15}Se_{17}Te_{53}$ glass compositions.

3.7.1. $Ge_{17}As_{18}Se_{56}Te_9$

The absorption edge of this material was 950 nm and it exhibited a transmission of 60% at 1550 nm. Figure 3.12 shows a z-scan conducted on $Ge_{17}As_{18}Se_{56}Te_9$ with incident pulse energies of 10 nJ with an aperture transmission of 50% (aperture diameter of 6 mm). The theoretical closed aperture trace was generated with an n_2 coefficient of 9.0×10^{-18} m^2W^{-1}. The theoretical open aperture trace was calculated using a nonlinear absorption coefficient of 3.0×10^{-12} mW^{-1}.

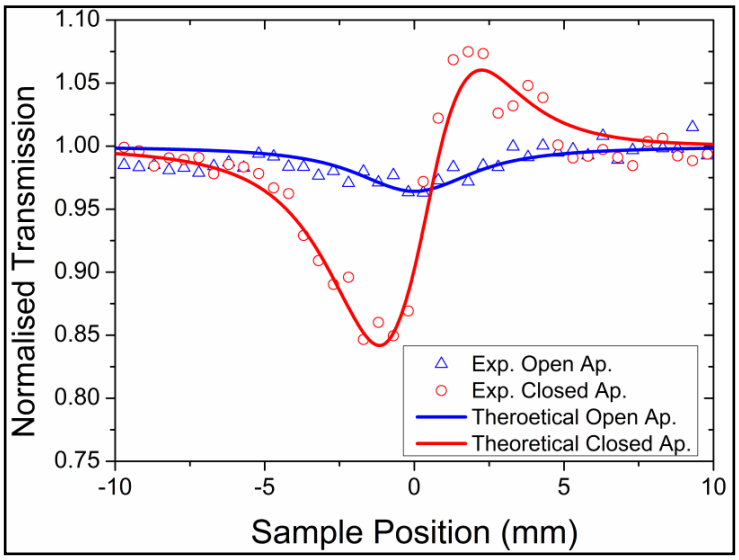

Figure 3.12: Z-scan trace conducted on $Ge_{17}As_{18}Se_{56}Te_9$ with pulse energies of 10 nJ. The closed aperture theoretical fit was calculated with a nonlinear refractive index coefficient of 9.0×10^{-18} m^2W^{-1}. The open aperture theoretical fit was modelled with a nonlinear absorption coefficient of 3.0×10^{-12} mW^{-1}.

3.7.2. $Ge_{15}As_{15}Se_{17}Te_{53}$

Strong linear absorption occurred in this sample as the investigation wavelength lies on the short wavelength absorption edge. Thus unsurprisingly this sample exhibited strong nonlinear absorption at 1550 nm, this strong nonlinear absorption clouded the effect of the nonlinear refraction on the z-scan traces; however the material n_2 was still estimated. Figure 3.13 (a) shows a z-scan conducted on $Ge_{15}As_{15}Se_{17}Te_{53}$ with pulse energies of 2 nJ and an aperture transmission of 50% (aperture diameter of 6 mm), here the closed aperture data has been divided by the open aperture data to more clearly observe the effects of nonlinear refraction. The theoretical fits used a nonlinear absorption coefficient of 2.7×10^{-10} mW^{-1} and a nonlinear refractive index of 4.45×10^{-17} m^2W^{-1}.

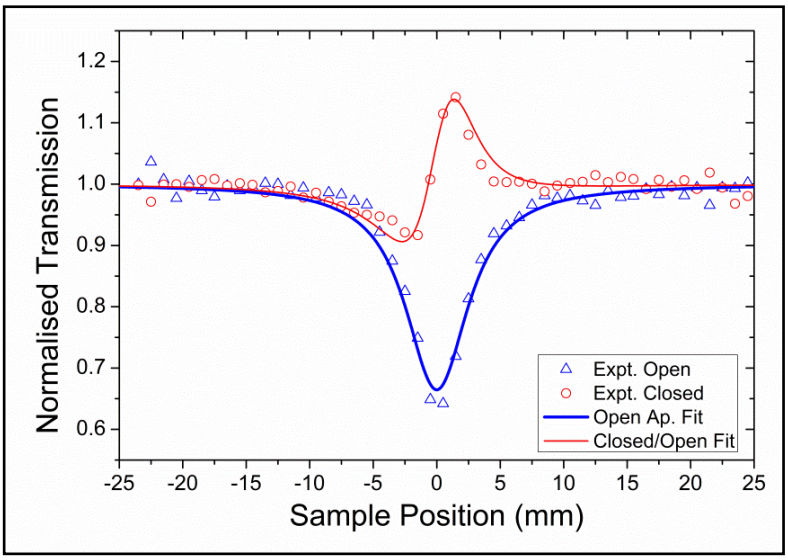

Figure 3.13: Z-scan trace conducted on $Ge_{15}As_{15}Se_{17}Te_{53}$ with pulse energies of 2 nJ. The closed aperture theoretical fit was calculated with a nonlinear refractive index coefficient of 4.47×10^{-17} m^2W^{-1}. The open aperture theoretical fit was modelled with a nonlinear absorption coefficient of 2.7×10^{-10} mW^{-1}.

3.8. Tellurites

Z-scan experiments at a wavelength of 1550 nm were carried out on six tellurite glasses in order to characterise their nonlinear refractive index coefficient. The six tellurite glasses are separated into two groups of three due to their compositions, namely; Na_2O-TeO_2 and K_2O-TeO_2 based tellurites. All six of the tellurite glasses were measured to have a nonlinear refractive index coefficient in the region of $\times10^{-19}$ m^2W^{-1} which is an order of magnitude lower than that of the chalcogenides. This also meant that z-scans on the tellurite glasses were carried out with higher pulse energies, ~300 – 480 nJ, no optical damage was observed on any of the tellurites after being exposed to field strengths of up to 98 GW/cm^2. No multi-photon absorption effects were observed in these samples up to the pulse energies outlined above.

Figure 3.14 shows the trend of the nonlinear refractive index for both sets of tellurite glasses with percentage of tellurium. Of the two sets, the Na_2O-TeO_2 based compositions exhibited the higher nonlinear refractive index. Little variation of the nonlinear refractive index, within the margin of error, was observed for the K_2O-TeO_2 based tellurites. A more distinct trend of varying nonlinear refractive index with

composition was observed in the Na_2O-TeO_2 tellurites with a maximum measured n_2 of 7.8×10^{-19} m^2W^{-1}.

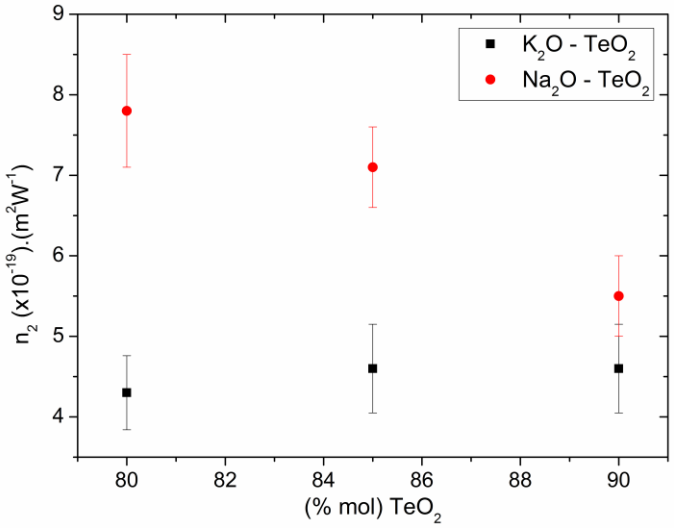

Figure 3.14: Calculated nonlinear refractive index coefficients calculated for the investigated Na_2O-TeO_2 and K_2O-TeO_2 tellurite glass systems.

3.9. ZnSe

The large transmission window, high damage threshold and low thermo-optical coefficient make ZnSe an appealing candidate for a number of photonic devices. The optical nonlinearities of ZnSe measured via the z-scan technique was the focus of the original z-scan [61] and white-light continuum z-scan [72] articles. The vast majority of these investigations characterised the nonlinear coefficients at wavelengths between 500-1270 nm. Major et al [73] measured the optical nonlinearities of single crystal ZnSe at the telecoms wavelengths of 1310 nm and 1550 nm – quoting an n_2 of 1.1×10^{-18} m^2W^{-1} and estimated the nonlinear absorption coefficient to be less than 1.0×10^{-13} mW^{-1} at wavelength of 1550 nm.

The polycrystalline ZnSe sample had a lower wavelength absorption edge of 485 nm and a linear transmission at 1550 nm of 70%. Figure 3.15 shows four z-scans conducted on the ZnSe with incident pulse energies of 40, 34, 30 and 20 nJ. These were fitted with a nonlinear refractive index coefficient of 1.8×10^{-18} m^2W^{-1} and a two-photon absorption coefficient of 6.5×10^{-13} mW^{-1}.

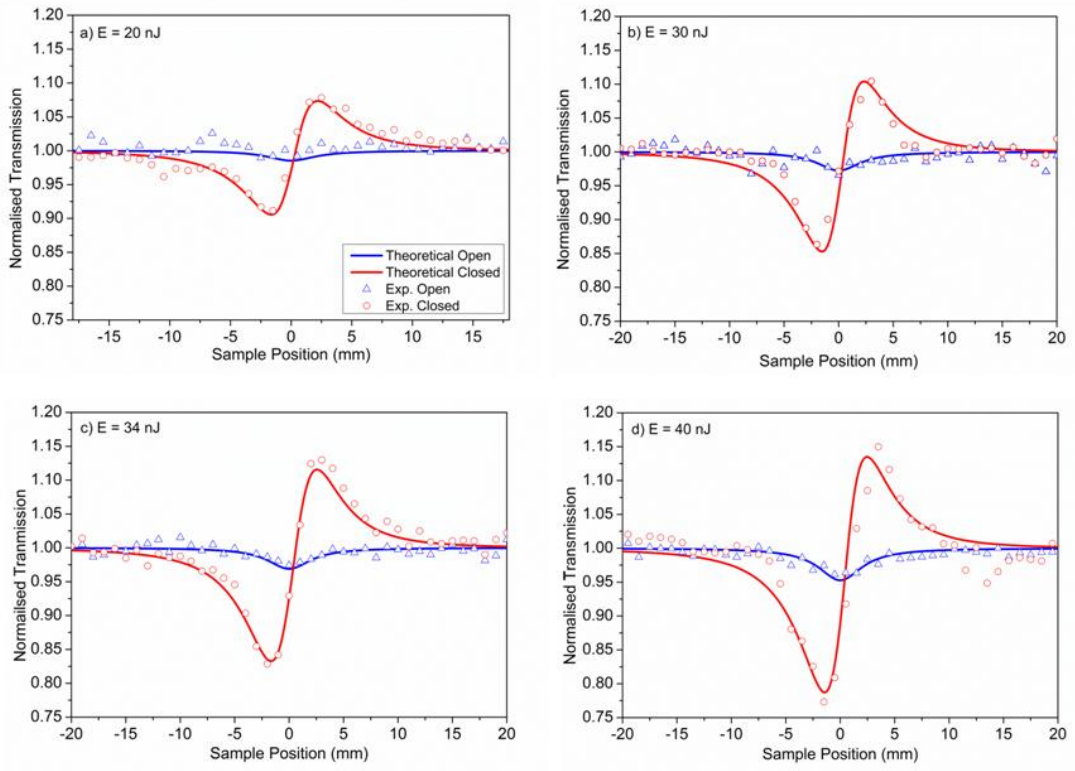

Figure 3.15: Z-scan traces conducted on ZnSe with pulse energies of (a) 20 nJ, (b) 30 nJ, (c) 34 nJ and (d) 40 nJ. The closed aperture theoretical fits were modelled with a nonlinear refractive index coefficient of 1.8×10^{-18} m^2W^{-1}. The open aperture theoretical fits were modelled with a nonlinear absorption coefficient of 6.5×10^{-13} mW^{-1}.

This calculated nonlinear refractive index is ~65% higher than that measured by Major et. al. and the nonlinear absorption coefficient is roughly 6 times higher than their estimated upper limit.

3.10. GLS

The GLS sample composition was {65} Ga_2S_3: {32} La_2S_3:{3} La_2O_3 and had a short wavelength absorption edge of 490 nm compared to the As-S-Se and As-Se-Te chalcogenide systems and a linear transmission of 70% at a wavelength of 1550 nm. The GLS glass was fabricated by melting a mixture of gallium sulphide, lanthanum sulphide and lanthanum oxide powders. The powders were then placed in a vitreous carbon crucible and melted in an argon-purged tube furnace at 1150 °C for approximately 24 hours. The melt was then quenched and the glass then annealed at 530 for approximately 24 hours [47].

Z-scans on GLS had to be conducted at much higher incident pulse energies compared to those conducted on ZnSe due to the disparity between the ZnSe and GLS sample thicknesses. Figure 3.16 shows two z-scans conducted on GLS with incident pulse energies 100 and 174 nJ. The aperture was set to a diameter of 2.8 mm which corresponded to 30% beam transmission. The closed aperture theoretical traces were fitted using a nonlinear refractive index coefficient of 1.5×10^{-18} m^2W^{-1}. This is approximately 30% lower than that measured in [47]. The effects of nonlinear absorption were not apparent in any z-scan; incident pulse energies of up to 400 nJ were investigated. This corresponds to a peak power of 3.64 MW and an irradiance of 9.45×10^{14} Wm^{-2} at the focus. Thus the upper limit on the nonlinear absorption coefficient is therefore 8×10^{-14} mW^{-1}. The lower limit for the nonlinear switching figure of merit for GLS at a wavelength of 1550 nm can be estimated by taking the measured value for the nonlinear refractive index and the approximated upper limit for the multiphoton absorption. The lower limit for the nonlinear optical switching FOM for GLS is therefore 6.05. This is much higher than the respective value for polycrystalline ZnSe and the chalcogenide samples investigated in sections 3.5 - 3.7.

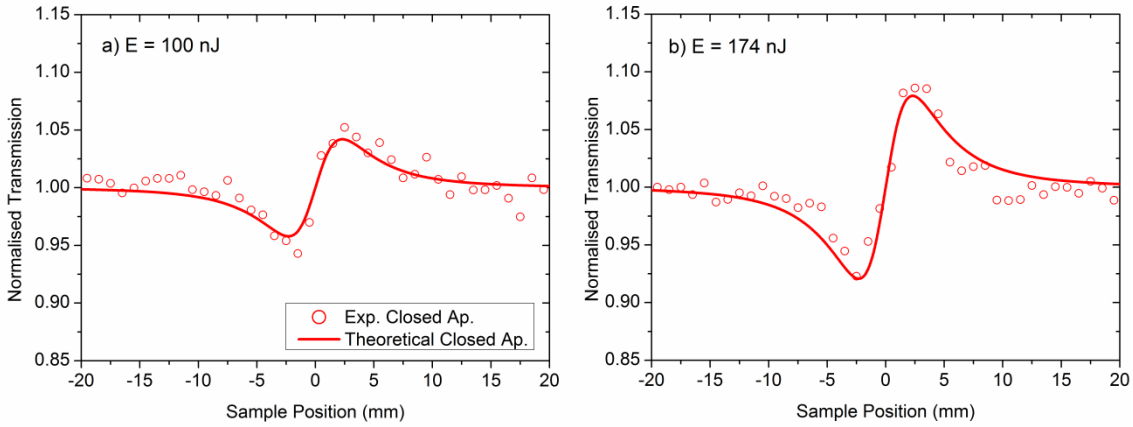

Figure 3.16: Closed aperture Z-scan traces conducted on GLS with pulse energies of (a) 100 nJ and (b) 174 nJ. The theoretical fits were modelled using a nonlinear refractive index coefficient of 1.5×10^{-18} m^2 W^{-1}.

3.11. Discussion

The aim of the investigation was to identify a material with a high nonlinear refractive index which was also easily compatible with the ULI process. A high nonlinear refractive index will allow for lower threshold for self-phase modulation, and therefore

allow for spectral broadening to occur at much lower pulse energies than in silica based waveguides. However the presence of nonlinear absorption during this process severely constricts the amount of spectral broadening. Applying the nonlinear switching figure of merit for each material will therefore help determine the best candidate for a ULI continuum source.

The glasses in the As-S-Se chalcogenide system exhibited a high nonlinear refractive index but also exhibited relatively high nonlinear absorption. Their nonlinear optical switching FOM were calculated by substituting these values into equation 3.1. These values are summarised in table 3.2. From table 3.2 it can be observed that none of the ternary As-S-Se based chalcogenides had a FOM greater than 1. The highest nonlinear refractive index of this system was exhibited by $As_{40}Se_{60}$ although this sample also exhibited the second highest nonlinear absorption. The calculated switching FOM for $As_{40}Se_{60}$ was greater than one, which demonstrates its suitability for photonic switching applications. The highest switching figure of merit in this system group was for the composition $As_{40}S_{60}$ despite exhibiting one of the lowest nonlinear refractive indices in the system group its multi-photon absorption coefficient was an order of magnitude smaller than that of $As_{40}Se_{60}$.

	As(40)S(60-x)Se(x)						
	Se(0)	Se(15)	Se(20)	Se(30)	Se(40)	Se(45)	Se(60)
n2 ($1x10^{-18}$).(m^2W^{-1})	2.35	2.30	3.60	4.50	6.00	6.10	10.50
β ($1x10^{-12}$).(mW^{-1})	0.53	1.00	2.70	2.00	3.70	2.80	2.80
F.O.M.	1.40	0.74	0.43	0.49	0.52	0.69	1.18

Table 3.2: Table summarising the nonlinear refractive index and absorption coefficients of the investigated $As_{40}S_{(60-x)}Se_{(x)}$ glass compositions and their corresponding nonlinear optical switching FOM.

The As-Se-Te based chalcogenide glasses exhibited the lowest nonlinear switching figures of merit. This was pre-dominantly due to the large multi-photon absorption. This can be seen from table 3.3 as the amount of tellurium is increased the FOM decrease rapidly.

	As(30)Se(70-x)Te(x)					
	Te(0)	Te(3)	Te(10)	Te(20)	Te(30)	Te(40)
n2 (1x10-18).(m2W-1)	4.50	5.50	15.50	25.00	44.00	-
β (1x10-12).(mW-1)	1.70	2.50	11.00	31.00	100.00	1.5
FOM	0.85	0.71	0.45	0.26	0.14	-

Table 3.3: Table summarising the nonlinear refractive index and absorption coefficients of the investigated $As_{30}Se_{(70-x)}Te_{(x)}$ glass compositions and their corresponding nonlinear optical switching FOM.

Although the multi-photon absorption coefficients of the tellurite glasses was so low that no nonlinear absorption effects were observed, the low nonlinear refractive indices of over an order of magnitude smaller than that of GLS and ZnSe meant that they were un-appealing when compared to these materials.

ZnSe was measured to have a slightly higher nonlinear refractive index but also a much higher nonlinear absorption than GLS, GLS therefore had a much higher FOM. Both materials showed no signs of optical damage even after exposure to very high irradiances (on the order of 1×10^{15} Wm^{-2}). Both samples are commercially available and have mature fabrication technologies; this is an important factor as any variation from sample to sample can have a large effect on the repeatability of the ULI fabrication process.

3.12. Conclusion

It has been shown how the z-scan method is a simple yet powerful optical characterisation technique that enables both nonlinear absorption and nonlinear refraction to be measured in many different types of materials. Z-scan experiments were carried out on various chalcogenide and tellurite glasses in order to determine their nonlinear refractive index and absorption coefficients. These coefficients not only determine the applicability of a material to ultrafast nonlinear optical switching and signal processing applications but can also inform us how useful a particular material will be for supercontinuum generation and give insight into ultrafast laser inscription processes. Of these samples, gallium lanthanum sulphide was measured to have the highest nonlinear switching figure of merit. Thus, GLS was chosen as substrate material for the writing of nonlinear optical waveguides via the ultrafast laser inscription

process. Other factors in favour of GLS included the fact that it is safer to work with than the arsenic based chalcogenide glasses and polycrystalline ZnSe, it is commercially available at a high optical quality and exhibits long wavelength transmission – this later fact being important to enable the extension of supercontinuum into the mid infrared and for mid infrared integrated photonic applications.

Chapter 4. Supercontinuum generation in microstructured fibres

4.1. Introduction

The work in this chapter focuses on supercontinnum generation in micro-structured optical fibres. Optical fibres can provide long interaction lengths with low transmission loss and a high level of optical confinement. This makes them well suited to the study and exploitation of nonlinear optical effects. The advances in microstructured fibre development have enabled the waveguide dispersion to be controlled and this fact can be used to tailor a fibre design to suit a particular pump source. Section 1.2 presents research conducted on two silica photonic crystal fibres fabricated at the Central Glass and Ceramics Research Institute (CGCRI) Kolkata, the emphasis of this study is the on the onset of the different spectral broadening mechanisms and how they shape the output spectrum. Section 1.3 presents results of a continuum investigation into a lead-silicate photonic crystal fibre, where the heavy lead doping allowed for decreased infra red absorption at wavelengths greater than 2000 nm. Finally, section 1.4 presents results into a 120 core fibre structure pumped at a wavelength of 1789 nm as to allow evanescent coupling between the cores.

4.2. CGCRI photonic crystal fibres

Two fibres with sample names PCF-19A and PCF-24 were fabricated by the CGCRI and investigated in this work. Both fibres consisted of a three air-ring cladding structure and had a zero dispersion wavelength in the region of 980 nm. This would allow solitary wave propagation to occur within the PCF structures when pumped by laser sources such as Nd:YAG or ytterbium doped fibre laser systems. The two fibres differed as PCF-24 was designed with an elliptical core and was therefore highly birefringent whist PCF19A had a more circularly symmetric core. The purposes of this investigation were to observe the threshold for the separate spectral broadening mechanisms in short lengths of PCF at pump wavelengths either side of the zero dispersion wavelength. These were then compared with the theoretical spectra numerically modelled by collaborators at CGCRI. The experimental framework

provided by this study aided microstructered fibre development at CGCRI by validating their nonlinear guiding model and allow them to accurately model fibre nonlinearity in advance of fabrication and tailor fibre design characteristics to yield a desired output spectra.

4.2.1. PCF-19A

4.2.1.1. *Fibre characteristics*

Figure 4.1 shows the fibre facet image of PCF-19A. The image was taken using a microscope calibrated with a USAF 1951 resolution chart. The fibre had a hexagonal shaped core with a size of 4.37 µm, an air hole size of 5.06 µm and pitch of 5.52 µm

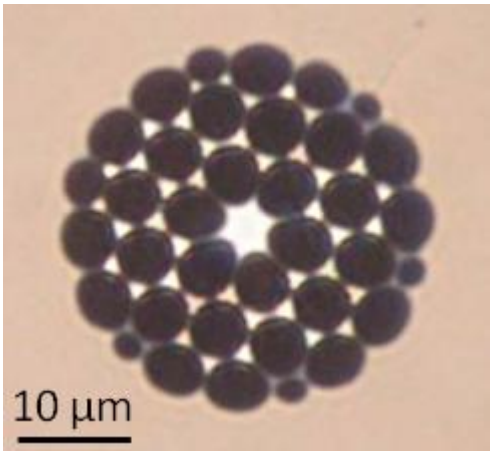

Figure 4.1: PCF-19A facet image

Linear characterisation of the fibre was performed at CGCRI. This characterisation included theoretical prediction of the dispersion profile and experimental measurement of the wavelength dependent loss. The theoretical dispersion profile would subsequently be used to calculate the higher order dispersion terms required to accurately model the nonlinear pulse propagation in the fibre. Figure 4.2 (a) shows the theoretically predicted dispersion profile of the fibre from 800-1800 nm. The zero dispersion wavelength of PCF19-A was calculated to be 987 nm. Figure 4.2 (b) shows the wavelength dependent loss in dB/km between 800 nm and 1800 nm. The large attenuation measured at 1400 nm, 1215 nm and 910 nm are due to large OH absorption.

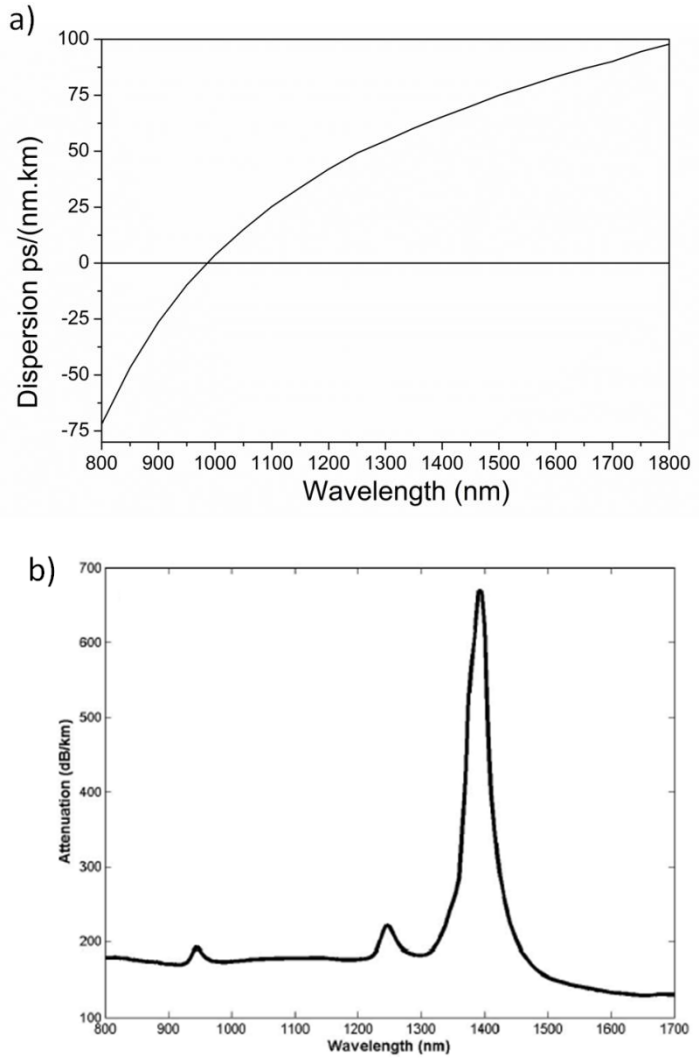

Figure 4.2: Graphs showing (a) Theoretical dispersion profile and (b) Attenuation of PCF-19A

The evolution of the spectral broadening of femtosecond pulses after propagation along 15, 20 and 30 cm fibre lengths were investigated for pump wavelengths of 900, 980 and 1060 nm.

4.2.1.2. *Experimental set-up*

In order to access pump wavelengths on either side of PCF-19As zero dispersion wavelength of 987 nm the idler output of the femtosecond OPA system outlined in section 2.7 was frequency doubled. The frequency doubling process had a 50% conversion efficiency. A maximum pulse energy of 20 µJ was measured at the OPA

output. As the frequency doubled idler has an orthogonal polarisation state to that of the fundamental Idler, the residual Idler radiation is separated from the beam path by a polarisation beam splitter (PBS) before being directed onto a beam dump. Figure 4.3 shows the experimental set-up for this investigation.

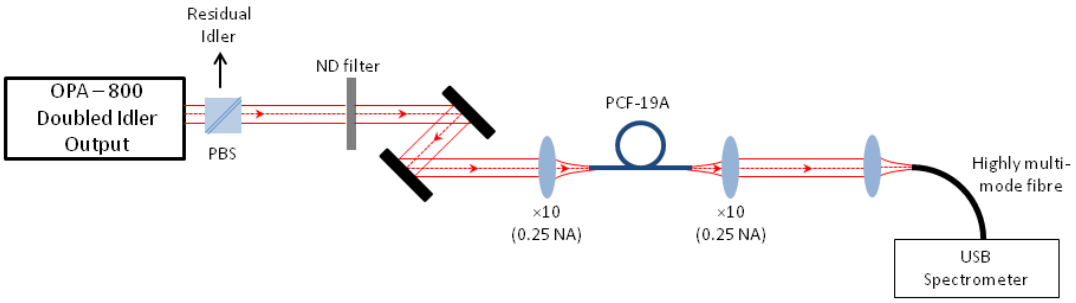

Figure 4.3: PCF-19A Supercontinuum investigation experimental set-up

After passing through the PBS the beam is then heavily attenuated by a set of ND filters and then directed by two mirrors onto the fibre coupling set-up. Each fibre facet is mounted onto an x, y, z translation stage. Two silica ×10 (0.25 NA) microscope objectives couple and collect the light to and from the test fibre. The coupling efficiency to the test fibre was 10%. Incident power measurements were made using a wavelength calibrated silicon low power photodiode (Newport 918-UV) connected to a universal power meter (Newport 1930c). The spectral output of PCF-19A was measured on two spectrometers; Ocean optics VIS2000 and Ocean optics NIR512, via a highly multimode collection fibre. The VIS2000 spectrometer has a silicon detector array and a working range of 400-1150 nm, whereas the NIR512 spectrometer has an InGaAs detective array and a working range of 850-1650 nm. A tungsten halogen light source (Ocean Optics LS-1) was used to calibrate the wavelength dependent response of each spectrometer and the collection fibre. Independently capturing and applying the separate wavelength correction factors for each spectrometer allows for their spectra to be stitched together in the 850 – 1150 nm wavelength regions. This allows for a working range of 400 – 1650 nm for recording broadband spectral outputs that lie on either side of the working range of the individual detectors.

4.2.1.3. *Experimental results – 900 nm pump wavelength*

Figure 4.4 shows the spectral output from a 30 cm length of PCF-19A for three incident pulse energies. The peak wavelength of each captured spectrum has been normalised to 0 dB. The input pump spectrum with a central wavelength of 900 nm is also shown for comparison.

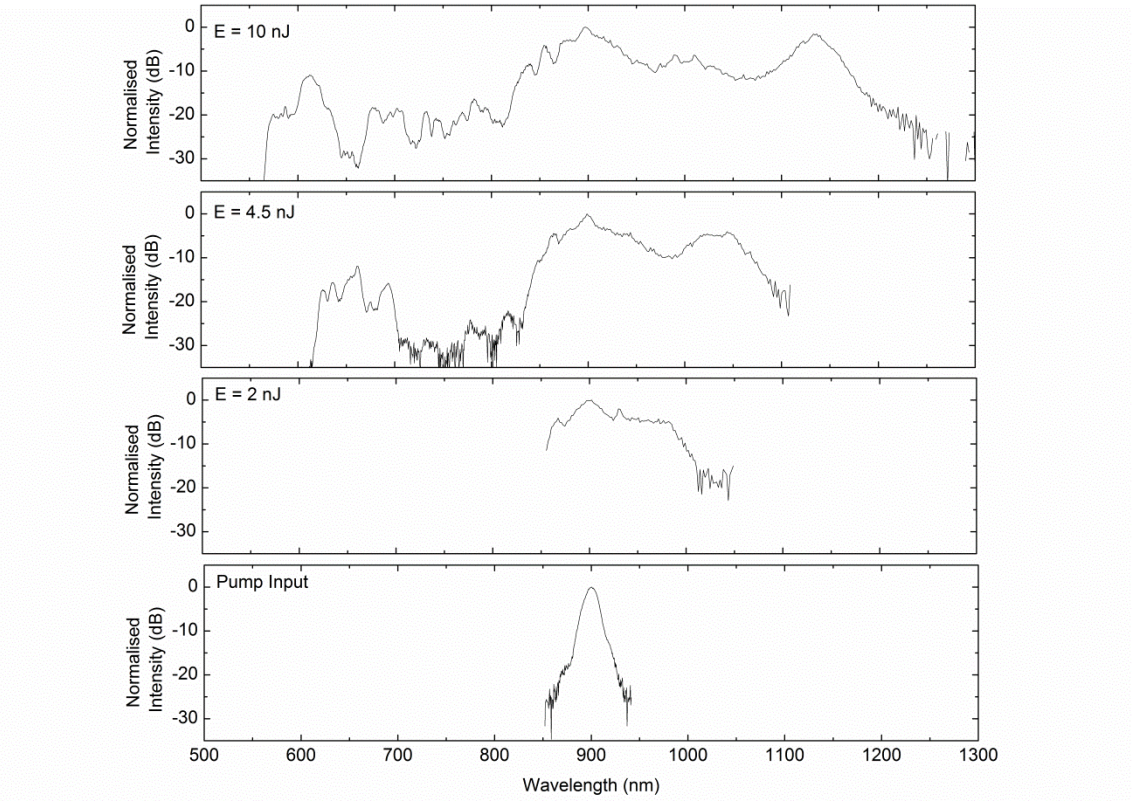

Figure 4.4: Spectrally broadened outputs from PCF-19A for incident pulse energies of 2, 4.5 and 10 nJ. The central pump wavelength was 900 nm. Pump spectrum is shown for comparison.

The characteristics of self-phase modulation; sharp spectral peaks symmetric about the pump wavelength can be observed on the 2 nJ spectrum of figure 4.4. As the coupled pulse energy is increased significant power is re-distributed into wavelengths that lie in the anomalous dispersion. This then generates a solitary wave that disperses to longer infrared wavelengths via stimulated Raman scattering. This soliton self frequency shift (SSFS) effect of this can be seen in the 4.5 nJ and 10 nJ traces of figure 4.4. The resulting spectral output is not symmetrical about the pump wavelength with reduced power in the 720 – 800 nm spectral region due to inefficient wave interaction.

4.2.1.4. *Experimental results – 980 nm pump wavelength*

Figure 4.5 shows the nonlinear broadening evolution with increasing incident pulse energies with a central pump wavelength of 980 nm. The pump wavelength lies just below zero dispersion wavelength of PCF-19A and is also shown for comparison with the output spectra.

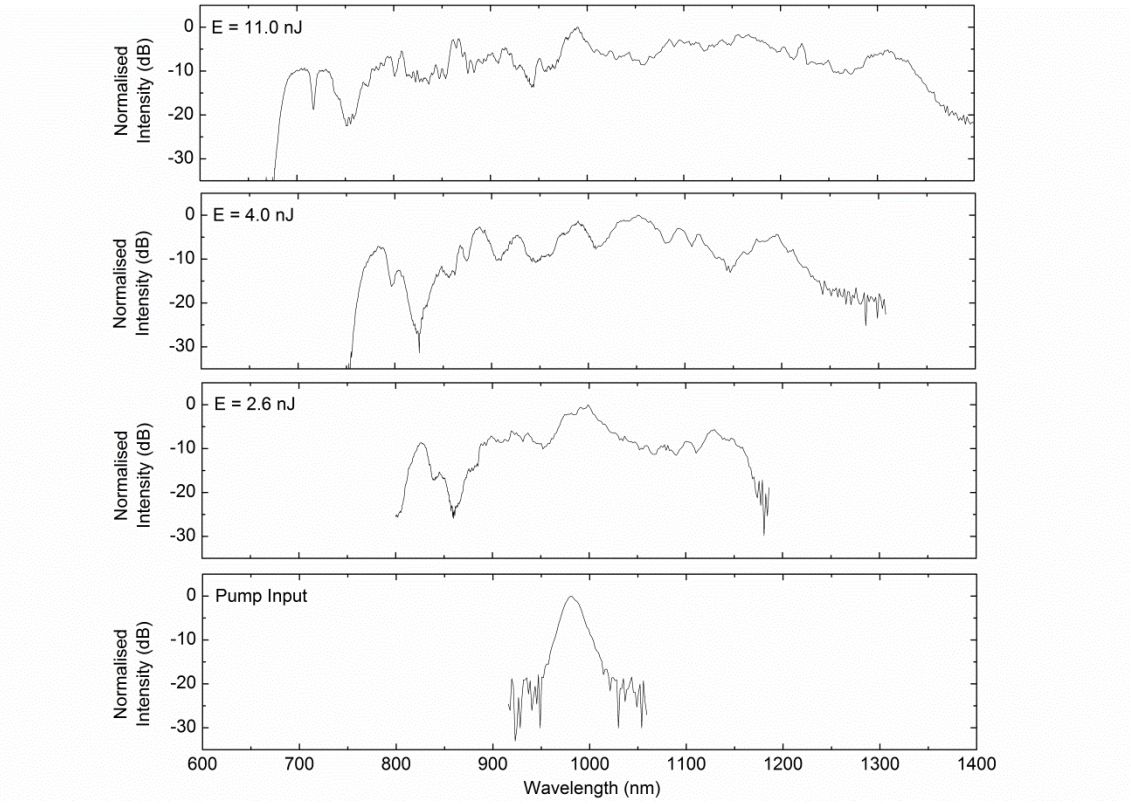

Figure 4.5: Spectrally broadened outputs from PCF-19A for incident pulse energies of 2.6, 4 and 11 nJ. The central pump wavelength was 980 nm. Pump spectrum is shown for comparison.

Due to the pump wavelength lying in the normal dispersion regime but just below the PCF-19As ZDW the effects of self-phase modulation are again clearly evident. However due to pump wavelengths close proximity with the ZDW the temporal broadening of the pulse as it propagates along the fibre is greatly reduced. Therefore, the peak power is higher over a longer length of the fibre. This increased peak power results in a stronger nonlinear interaction. Additionally due to pump wavelength being situated close to the ZDW the spectral broadening is more symmetric about the pump wavelength and more homogeneous.

4.2.1.5. *Experimental results – 1060 nm pump wavelength*

The pump wavelength of 1060 nm is situated ≈70 nm into the anomalous dispersion regime; therefore soliton dynamics such as soliton fission and SSFS will have an increased effect on the spectral broadening process over that of self-phase modulation. The evolution of spectral broadening with increased pump power is shown in figure 4.6. The low threshold effects of self-phase modulation are again evident. The dip in and around the zero-dispersion wavelength of 987 nm in all three spectra is due to weak four-wave mixing [74]. The width of this spectral dip is wider than that observed in the 980 nm output spectra as the pump is situated further from the fibre ZDW. Additionally the red shifting solitary wave can be observed on all three PCF-19A output spectra

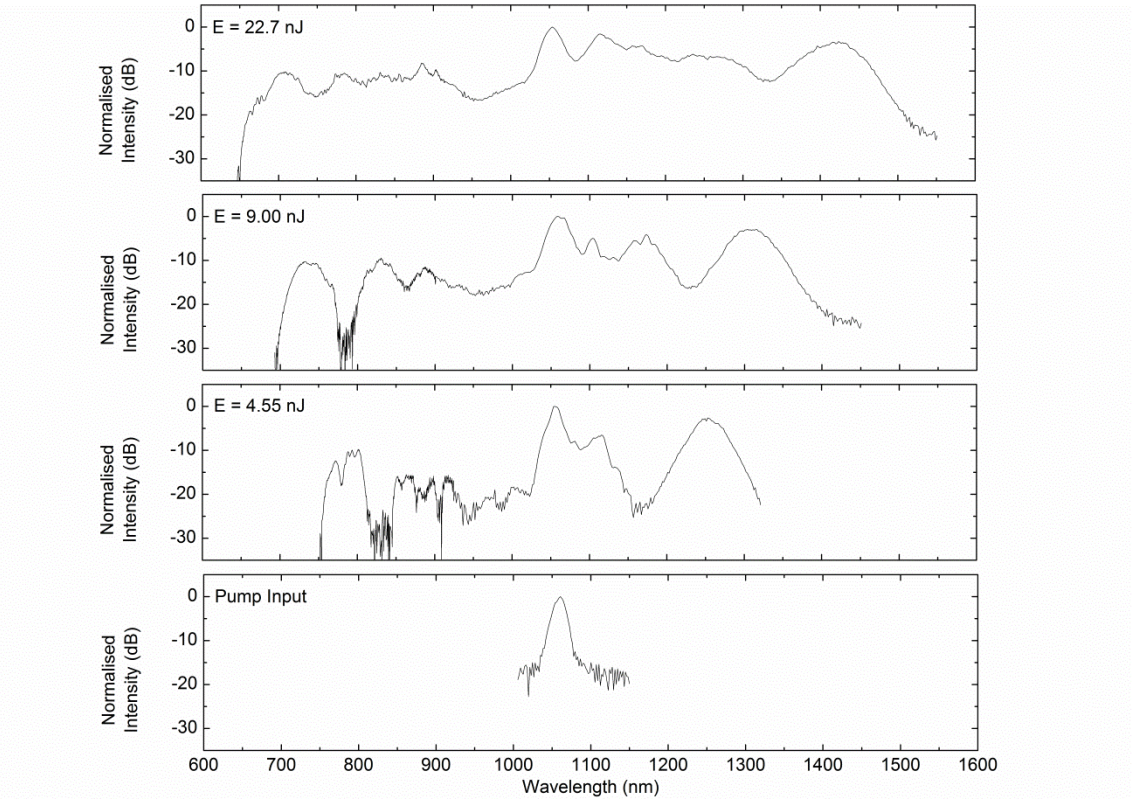

Figure 4.6: Spectrally broadened outputs from PCF-19A for incident pulse energies of 4.55, 9 and 22.7 nJ. The central pump wavelength was 1060 nm. Pump spectrum is shown for comparison.

The 4.55 nJ incident pulse spectra above is compared to that of a numerically modelled spectra calculated by D. Ghosh at CGCRI. The comparison is shown in figure 4.7 (a). The simulation was based on modelling the general nonlinear Schrodinger equation.

This was simulated using up to the 6th order dispersive term of the fibre at the wavelength of 1060 nm. There is good agreement with the experimental and theoretical spectra; figure 4.7 (b) highlights the enhancement of power in the normal wavelength regime due to interaction with the co-propagating solitary wave due to their matched group delays.

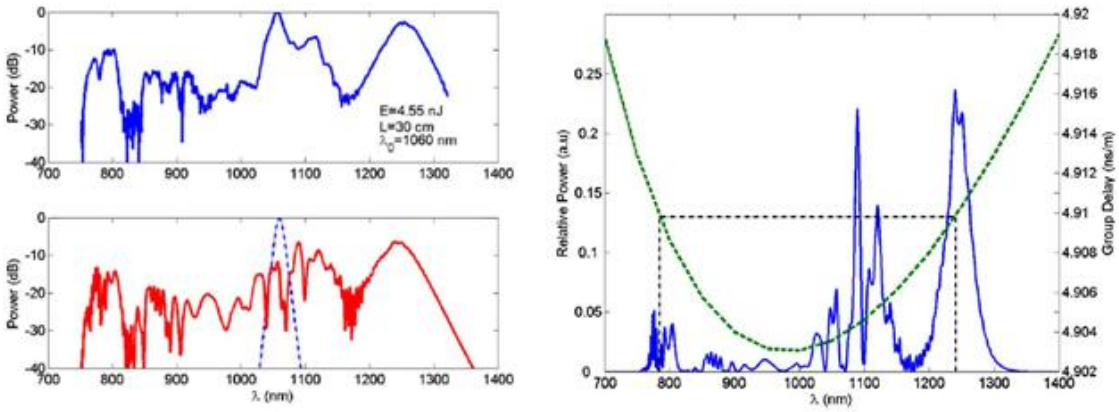

Figure 4.7: a) Comparison of experimental and theoretical spectral outputs of PCF 19-A for incident pulse energies of 4.55 nJ. b) Experimental ouptut curve from a) plotted with a linear y-axis and highlighting the matched group delay of the solitary wave and radiation in the normal dispersion regime [75].

4.2.1.6. *Discussion - PCF-19A*

The threshold and evolution of spectral broadening mechanisms were experimentally investigated. The investigation was primarily undertaken to confirm the highly nonlinear guiding characteristics of the 3 air-hole ring photonic crystal design. The 3 air hole ring design has a significantly lower manufacturing cost and has less stringent fabrication conditions. The peak powers required for the onset of spectral broadening were quite high; this was primarily due to the poor coupling of the laser light to the photonic crystal fibre. Numerical simulations performed by D. Ghosh at the CGCRI closely matched the experimental spectra thus validating their theoretical modelling methods. Using this information they then designed a polarisation maintaining highly bi-refringent fibre, PCF-24, in the expectation that it should enhance the continuum generation for radiation that is launched into the fast or slow axis of the fibre.

4.2.2. SC in PCF -24

4.2.2.1. *Fibre characteristics*

PCF-24 is designed with an elliptical core structure. The ellipticity of the core allows for polarisation state of the guided mode to be preserved after propagation along the fibre [76] i.e. the fibre is polarisation maintaining when launched into either of the principle axis of the fibre. Due to this high birefringence the fibre dispersion characteristics for each principal axis are different. A polarised supercontinuum can then be used to pump a non-centrosymmetric crystal to allow for nonlinear frequency conversion [77]. Figure 4.8 shows an end facet image for PCF-24. The fast axis core diameter is 2.76 µm and the slow axis core diameter is 5.52 µm, thus giving a core ellipticity of 2:1. The theoretical fibre dispersion characteristics for both the slow and fast axis are shown in figure 4.9. The slow axis ZDW is 950 nm and the fast axis had a ZDW of 925 nm.

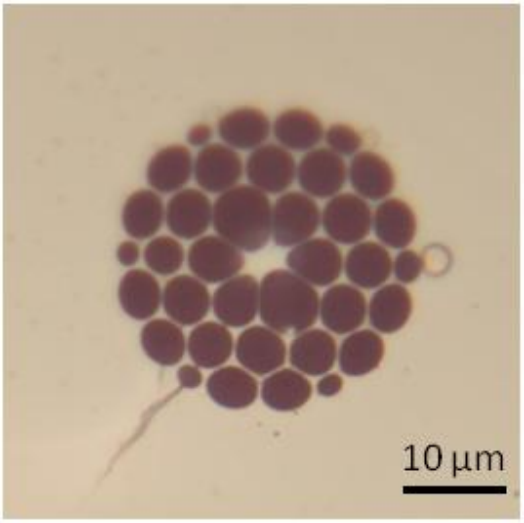

Figure 4.8: Microscope image of PCF-24 facet.

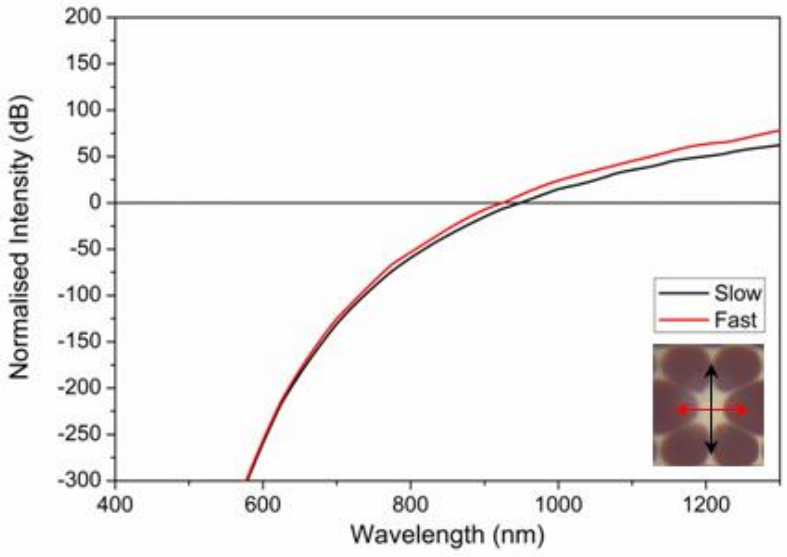

Figure 4.9: Theoretical PCF-24 dispersion profile for both the fast and slow axis

The experimental arrangement for investigating the supercontinuum polarisation dependence of PCF-24 is shown in figure 4.10. This is an adaption of that shown in figure 4.3 with the addition of a half-wave plate to rotate the plane of polarisation added to the input beam path. 30 cm fibre lengths were investigated. The input facet orientation is observed on a camera by coupling the LS-1 white-light calibration source to multi-mode fibre and coupling to the fibre, a flip mirror then directs the illuminated front facet onto a camera.

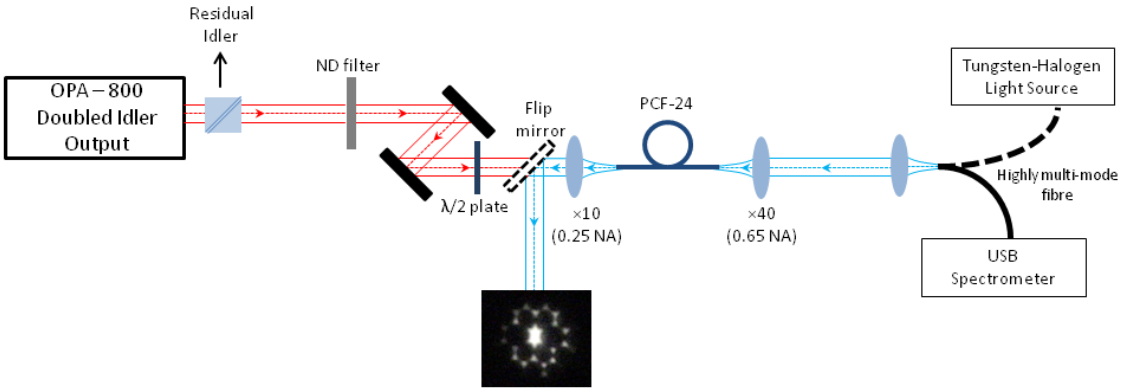

Figure 4.10: PCF-24 Supercontinuum investigation experimental set-up.

Three pump sources are investigated; 900, 935 and 980 nm. These investigation wavelengths were chosen as they lie in the normal (900 nm) and anomalous (980 nm) dispersion regimes for both principle axis of the fibre and the 935 nm wavelength lies in

the region between the two zero dispersion wavelengths. A coupling efficiency of 17 % was achieved via coupling with a 10× (0.25 NA) microscope objective.

4.2.2.2. *Experimental results - 980 nm central pump wavelength*

Figure 4.11 shows the effect of polarisation orientation on the extent of spectral broadening when pumping in the anomalous dispersion regime for polarisations of a) 90° i.e. coupled to fast axis, b) 0° i.e. coupled to slow axis and c) 45° equally coupled to two principal axis'. The incident pulse energy was 13 nJ.

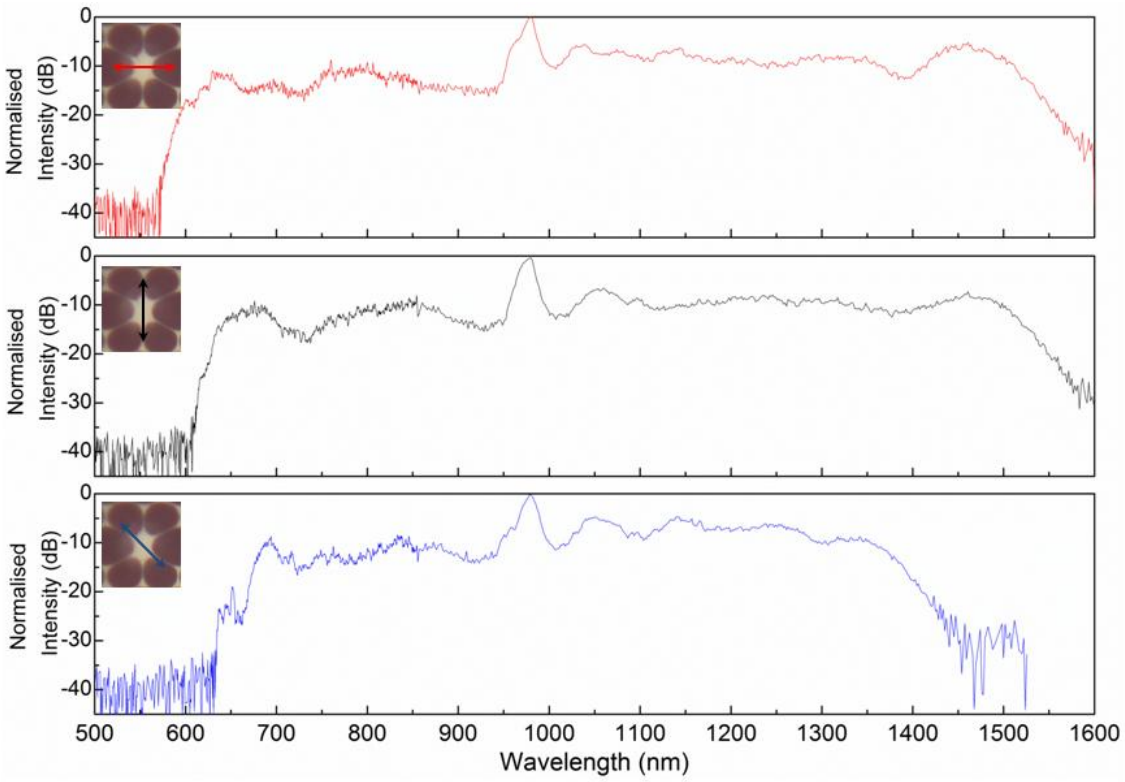

Figure 4.11: Spectral output recorded from PCF-24 for input field polarisations aligned to the fast axis – red curve, aligned to the slow axis – black curve, and aligned 45° to either axis – blue curve. The incident pulse energy was 13 nJ with a central wavelength of 980 nm.

All three spectra in figure 4.11 have been normalised to their respective peaks and all three exhibit a small red shift with respect to that of the pump wavelength of 980 nm. The broadest continuum is generated when coupling to the fast axis of the PCF. When comparing the spectra that generated by coupling to the fast and slow axis there is little difference in the power generated on the long wavelength edge ≈ 10 nm difference in

the -20 dB points of each spectra. Where-as on the short wavelength side there is a difference by aligning the pump polarisation into the fast axis extends the continuum approximately 40 nm further than aligning to the slow axis. This increased extension on the short wavelength side is due to shorter wavelengths matching the group velocity of the Raman shifted soliton due to the 25 nm difference in ZDW between the two orthogonal axis. The continuum generated by having the input pump polarisation set to 45° with respect to both axis' is dramatically reduced due to the temporal walk-off, due to group-velocity mis-match. This is due to the input pulse energy being split between the two axes which have two differing dispersion characteristics and thus the split pump components only over-lap in time over a very short fibre length < 1 cm. Since the fibre length of 30 cm is much greater than this interaction length the generated continuum is not as broad.

4.2.2.3. *Experimental results – 900 nm central wavelength*

Figure 4.12 shows three spectra for three input pump polarisations. The incident pulse energy was 13 nJ. The pump wavelength of 900 nm lies in the normal dispersion regime, and unlike when the case when pumping in the anomalous dispersion regime at 980 nm there is little effect on the width of the continuum generation when coupling into the fast or slow axis of the fibre. However the pulse energy threshold for spectral broadening was lower when coupled into the fast axis rather than the slow axis. The initial broadening occurs in the normal dispersion regime. As the broadening then crosses into anomalous dispersion regime solitons are formed and they then undergo SSFS. This effect is highlighted in figure 4.13.

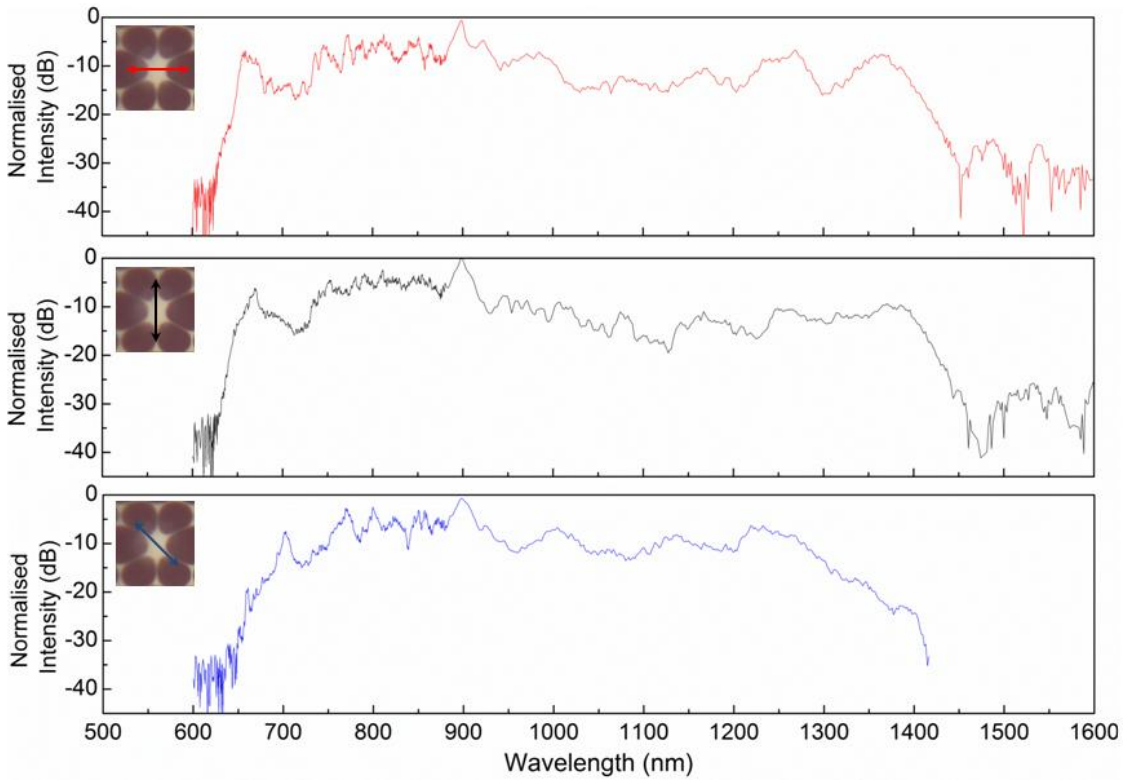

Figure 4.12: Spectral output recorded from PCF-24 for input field polarisations aligned to the fast axis – red curve, aligned to the slow axis – black curve, and aligned 45° to either axis- blue curve. The incident pulse energy was 13 nJ with a central wavelength of 900 nm.

When coupling equally into both axis of the fibre the power is again split and the width of the continuum is again observed to be dramatically reduced. At the -20 dB points the continuum when aligned to the fast axis spanned 776 nm from 1421 to 645 nm, this is almost 200 nm less than when the pump was tuned to a wavelength of 980 nm. Figure 4.13 shows the spectral broadening evolution for three pump powers with a central wavelength of 900 nm for a 30 cm length of PCF-24. The pump input was coupled into the slow axis of the fibre.

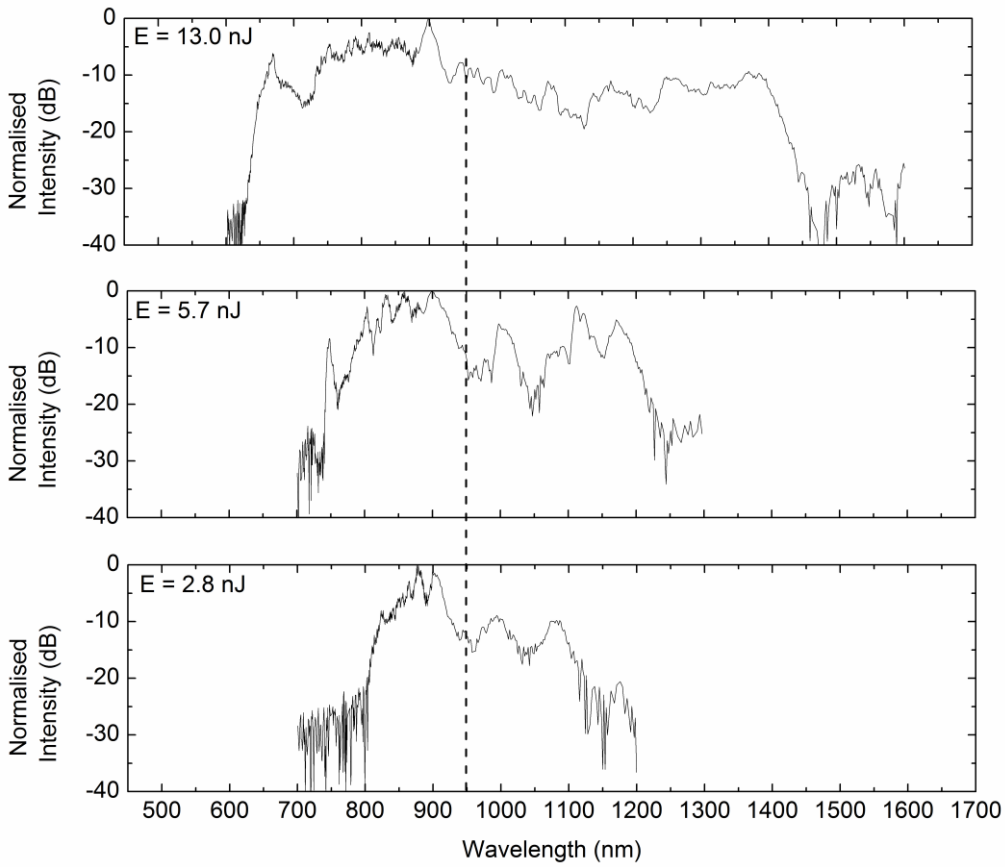

Figure 4.13: Spectral power distribution of PCF-24 for incident pulse energies of 2.8, 5.7 and 13.0 nJ. The central pump wavelength was 950 nm. The pump radiation was aligned to the slow axis of the fibre. Dashed line indicates the ZDW.

Figure 4.13 highlights the effect of pumping in the normal dispersion regime but close to the zero dispersion wavelength – namely SPM effects on the short wavelength side of the continuum generation and SSFS effects as the continuum crosses over into the anomalous dispersion regime [78].

4.2.2.4. *Experimental results - 935 nm central wavelength*

The central pump wavelength of 935 nm lies in the normal dispersion regime for light confined in the slow axis of PCF-24 whereas for radiation coupled to the fast axis this wavelength lies in the anomalous dispersion regime. Figure 4.14 shows the effect the input pump polarisation had on the broadening for a pump wavelength of 935 nm. The input pulse energies were 6.1 nJ and the fibre length was 30 cm.

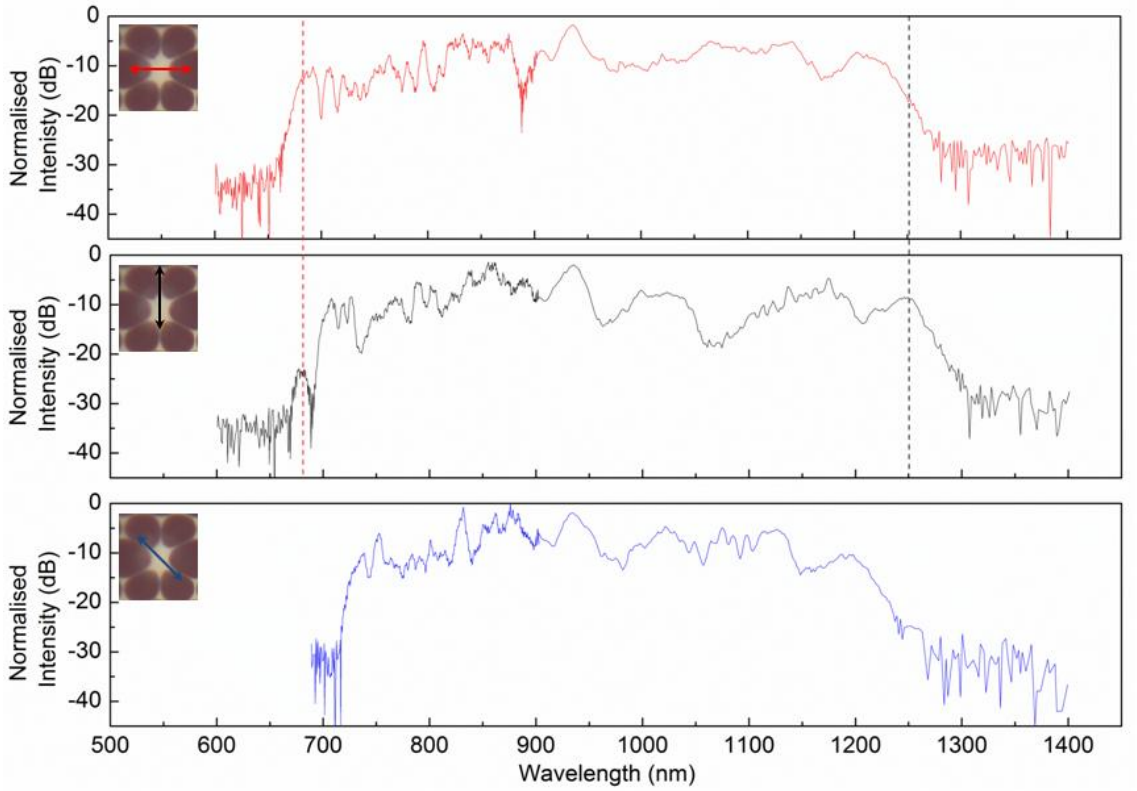

Figure 4.14: Spectral output recorded from PCF-24 for input field polarisations aligned to the fast axis – red curve, aligned to the slow axis – black curve, and aligned 45° to either axis- blue curve. The incident pulse energy was 6.1 nJ with a central wavelength of 935 nm.

As seen in figure 4.14 the continuum extends furthest into the infrared when coupled into the slow axis, this differs from the 980 nm pumping regime. When coupled to the slow axis the pump wavelength lies in the normal dispersion regime, therefore soliton dynamics don't affect the pulse propagation until the broadening extends into the anomalous dispersion regime. This cross-over occurs further along the fibre than the initial SPM broadening and therefore the SSFS gives less of its energy to the short wavelength radiation and is allowed to shift further into the infrared. The opposite case is evident when coupled to the fast axis of the fibre which lies in the anomalous dispersion regime – the pump initially undergoes soliton fission and SSFS shifts to longer wavelengths, the long wavelength walk-off of which is restricted by XPM effects with the co-propagating short wavelength radiation. This yields an enhanced short wavelength edge to the continuum, and a more uniform continuum, at the expense the infrared extending continuum. Again the when coupling into both axis shows a

reduction in spectrally broadening due to the power being split between both axis with a reduced interaction.

4.2.2.5. *1060 nm fibre laser coupling*

A ytterbium doped fibre laser (Fianium µJ) was used to investigate the nonlinear guiding properties of PCF-24. This investigation focused on obtaining the broadest continuum possible and was of interest to CGCRI due to the compact and robust nature of the pump source. The fibre laser repetition rate was set to 500 kHz with pulse durations of 300 fs and a central wavelength of 1060 nm. The laser output was linearly polarised and aligned to the fast axis of PCF-24. Figure 4.15 shows the dispersed output from PCF-24 for input pulses with an average power of 200 mW (pulse energies of 400 nJ) after propagation along a 30 cm length of fibre. The output was dispersed by guiding the output radiation through a prism. The long wavelength edge of the continuum did not extend beyond 1900 nm. The short wavelength edge extended throughout the visible down to a wavelength of 410 nm.

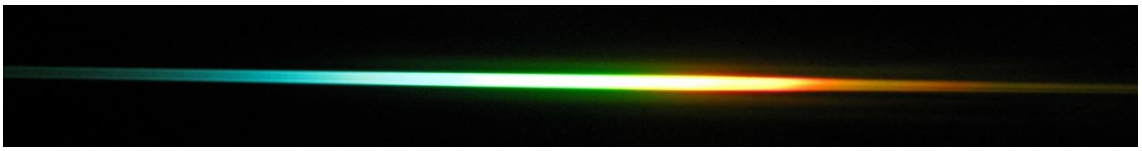

Figure 4.15: Visible wavelength component of the supercontinuum from PCF-24 dispersed through a prism.

4.2.2.6. *Discussion PCF-24*

The effect of input polarisation on the generation of supercontinuum generation was investigated for a highly bi-refringent microstructured fibre. Optimum pumping conditions were found to be when pumping in the anomalous dispersion regime and with the input field aligned to that of the fast axis of the fibre. The long wavelength cut-off was found to be 1900 nm; this was due to high intrinsic losses exhibited by silica at wavelengths greater than 1700 nm. Coupling the input pump radiation to the fast axis of the fibre allowed for increased nonlinear interactions in PCF-24 compared to that of the low birefringent PCF-19A.

4.3. Supercontinuum generation in lead-bismuth-galate oxide glass PCF

As seen in the PCF-19A and PCF-24 investigations the span of the supercontinuum generation in the 2-5 μm wavelength region of silica based PCFs is restricted due to the poor transparency of silica in this wavelength region. This section presents results for the nonlinear guiding properties of a lead-bismuth-galate oxide glass photonic crystal fibre (PBG08) with a high mid infrared transparency.

4.3.1. Glass composition and fibre structure

The lead-bismuth-galate oxide fibre (PBG08) was fabricated at the Institute of Electronic Materials Technology in Poland. The glass composition was {mol %}:

{40} SiO_2, {30} PbO, {10} Bi_2O_3, {13} Ga_2O_3, {7} CdO.

In addition to the increased mid infrared transparency this material exhibited a higher linear index of 1.97 and a higher nonlinear refractive index of 4.3×10^{-19} m^2W^{-1} than that of silica and therefore comparable to tellurite glasses; however PBG08 was found to have a much lower thermal expansion co-efficient relative to tellurite glasses. This is beneficial to the preform fabrication and fibre drawing process as the glass is less sensitive to temperature fluctuations.

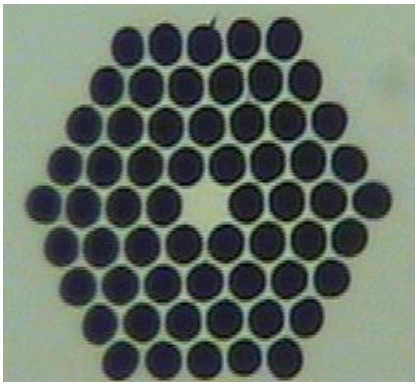

Figure 4.16: PBG08 microscope facet image

The fibre end facet is shown in figure 4.16. The PCF was designed with a 4 air ring structure with a lattice constant of $\Lambda = 3.55$ μm and fill factor 0.77. The diameter of the

core is 3.63 µm and a photonic cladding diameter of 24.3 µm. The effective mode area was 3.1 µm^2. The zero dispersion wavelength was calculated to be 1420 nm. Due to the total diameter being 586 µm the 'fibre' was in-flexible and was comparable to a rod. The fibre facets were prepared by introducing a defect on the fibre surface with a diamond tipped scribe and gently applying angular pressure to cleave the facet.

4.3.2. Extending infrared supercontinuum generation in PBG08 photonic crystal fibre

The selected pump wavelength was 1540 nm which is situated 120 nm into the anomalous dispersion regime of the fibre according to the calculated dispersion properties. The laser system outlined in section 2.7 was used. The experimental configuration is shown in figure 4.17. The signal output port was used to generate the required 1540 nm wavelength radiation. After being heavily attenuated by neutral density filters the output is passed through a spatial filter and then through a half-wave plate and polariser which were used to adjust the incident power. Light was coupled to the test fibre via a ×20 (0.4 NA) microscope objective. The coupling efficiency was 20%. A ×40 (0.65 NA) microscope objective collected the fibre output and directed it onto a near infrared camera or into a highly multimode fibre which was then coupled independently to one of three spectrometers. In addition to the OceanOptics spectrometers used in section 4.2 a BWTek BTC500E spectrometer with a PbS detector array was used to measure the spectral power in the wavelength region of 1650 – 2500 nm. A 20 cm length of PBG08 was tested.

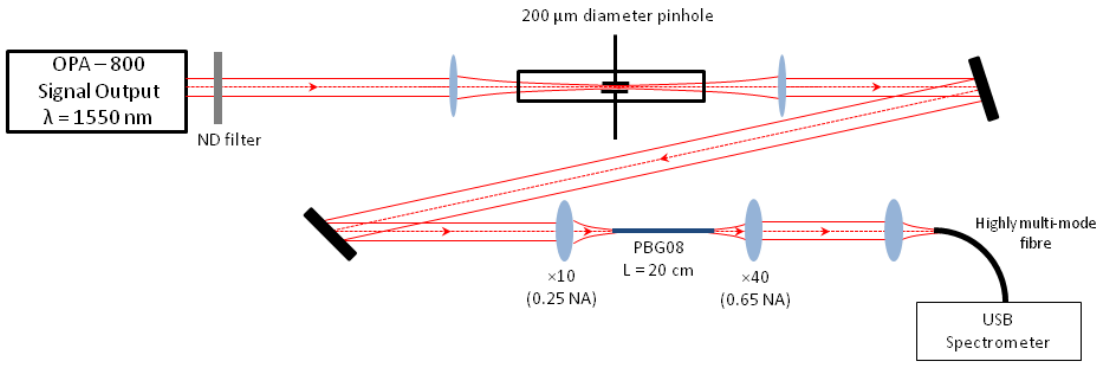

Figure 4.17: PBG08 Supercontinuum investigation experimental set-up

Continuum generation spanning 700 – 2500 nm was measured for input pulse energies of 44 nJ (figure 4.18). Figure 4.18 shows the input pulse spectrum and the spectra collected at the fibre output after 16 nJ and 44 nJ pulses are incident onto the fibre facet. Taking into account the 20 % coupling efficiency this yielded coupled pulse energies of 3.2 and 8.8 nJ. Due to the poor transmission of the silica multi-mode patchcord and poor response of the PbS spectrometer at wavelengths longer than 2600nm the measured continuum plots in figure 4.18 are cut-off at 2500 nm.

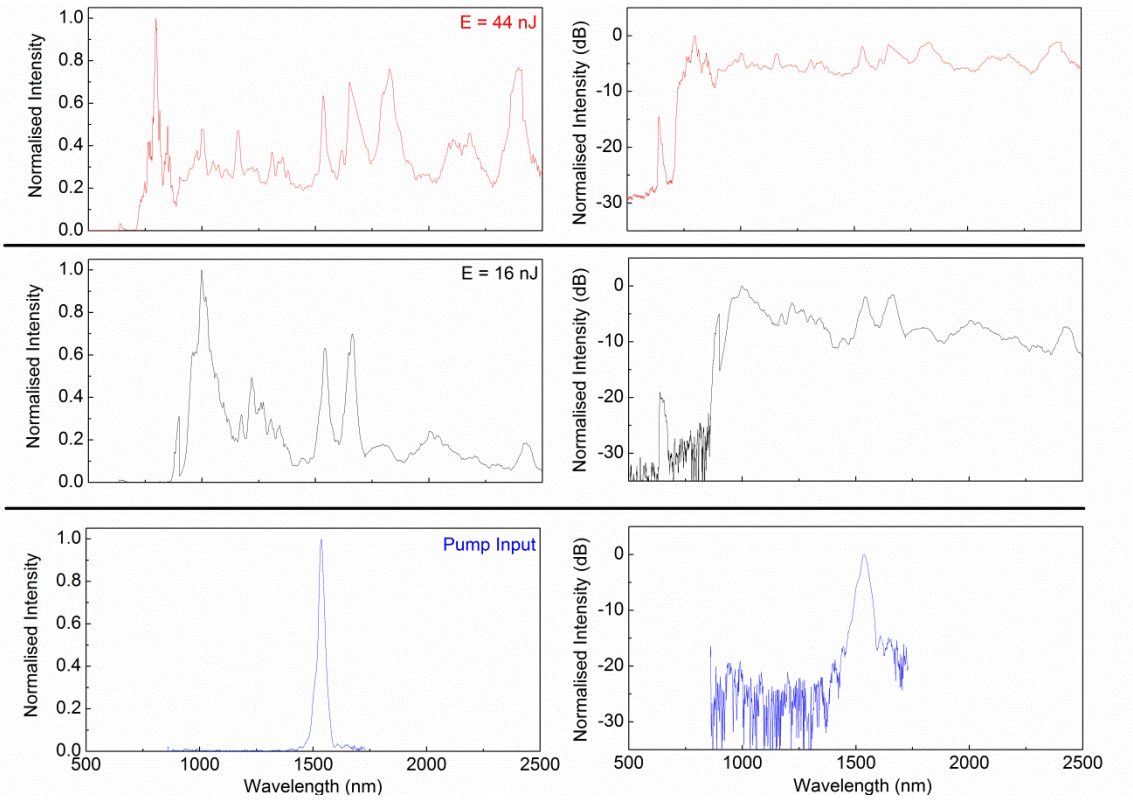

Figure 4.18: Spectral output of PBG08 for incident pulse energies of 16 nJ and 44 nJ. Spectra are shown in both a linear and log scale. The pump spectrum with a central wavelength of 1540 nm is shown for comparison

In comparison to the supercontinuum spectra obtained for PCF-19 and PCF-24 the recorded spectra for PCF-PBG08 is broader and extends ≈ 600 nm further into the infrared. The threshold for continuum generation for PCF-PBG08 was also much lower due to the higher material nonlinear refractive index. The limitation of the equipment meant that the full extent of the mid infrared continuum could not be measured.

4.4. 120 core MCF – evanescent field effects on supercontinuum generation

This section presents results on femtosecond pulse propagation measurements conducted onto a multi-core fibre with 120 equally spaced cores. The initial focus of this investigation was to experimentally demonstrate spatial soliton formation [79] in a multi-core fibre.

An optical spatial soliton is a self-trapped optical beam that propagates in a medium without diffraction [80]. In the context of this experiment the nonlinear localisation would be manifested via reduced evanescent field coupling from the central coupled core of a 120 core fibre. This occurs due to the nonlinear refractive index of the fibre altering the propagation constant and thus reducing the coupling coefficient between cores [80]. This nonlinear localisation effect has been observed in ULI waveguide array [81].

The 120 core fibre was supplied by Bath University; the end facet is shown in figure 4.19. The fibre was designed/ fabricated to operate at 1550 nm with no interaction between adjacent cores. Each core has a diameter of 8.64 μm and each guides a single transverse mode at 1550 nm. The spacing between cores was 34.2 μm. To allow for evanescent coupling between the cores the wavelength of the Idler output of the femtosecond OPA system described in section 2.7 was tuned to wavelengths greater than 1650 nm.

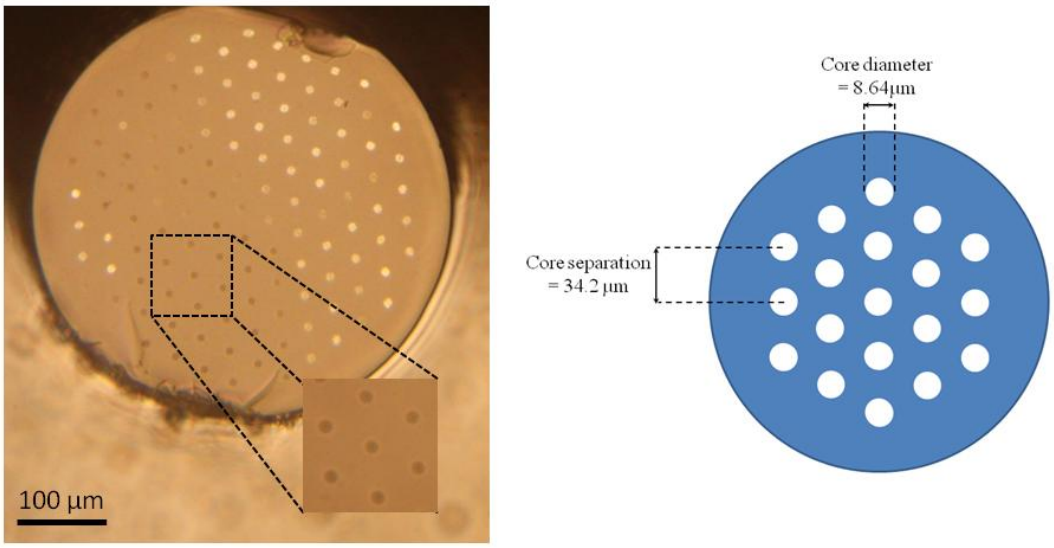

Figure 4.19: Shows (a) Microscope facet image of 120 core fibre and (b) Schematic highlighting the core diameter and core spacing

The beam was focused into and the central core by a ×20 (0.4 NA) microscope objective. The fibre output is then imaged onto a FLIR SC7000 camera by another ×20 (0.4 NA) microscope objective. The fibre length was 175 mm. Figure 4.20 shows the imaged MCF facet under low power (16 µW, 16 nJ) and high power (65 µW, 65 nJ) conditions.

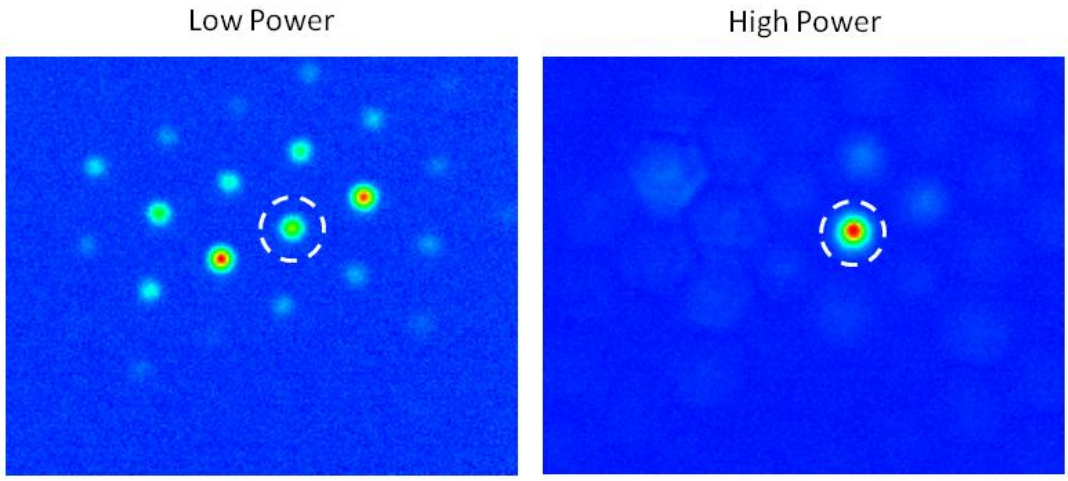

Figure 4.20: Low and high power images showing the core output from the 120 core fibre.

From figure 4.20 the effects nonlinear localisation appear apparent as the coupled power to the adjacent cores is reduced. However due to the high sensitivity and long

wavelength response of the imaging camera out-of-focus rings can be observed on the high power image. These regions were brought back into focus by adjusting the output coupling objective; this is shown in figure 4.21. The disparity in the focal planes for the central and outer ling cores was found to be due to spectral broadening of the femtosecond pulses. The shorter wavelengths generated are confined to the central core, where-as the longer wavelength generation experiences increased evanescent coupling and couples to the adjacent cores.

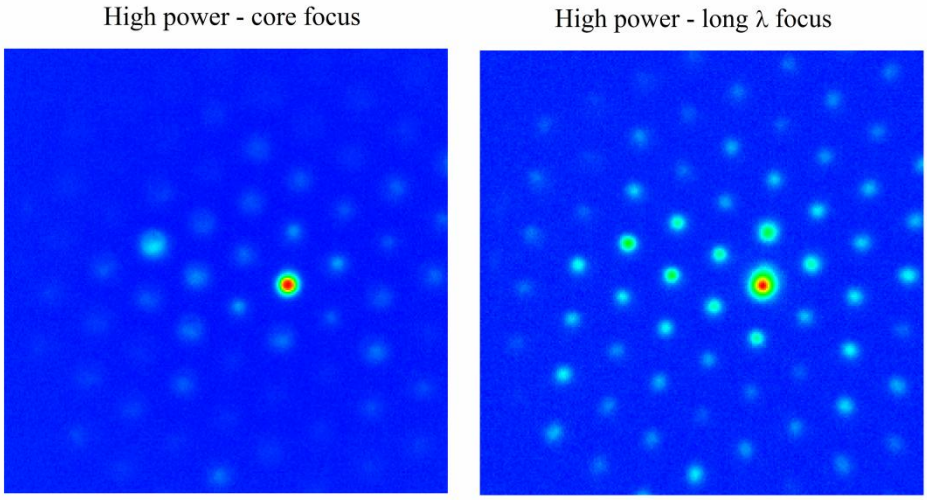

Figure 4.21: 120 core fibre output under high power coupling conditions. Image in (a) has the output objective positioned to focus pump wavelength radiation. In (b) the position of the output objective has been changed to focus the radiation in the outer lying cores

To investigate the supercontinuum spectra guided in the coupled core and the adjacent cores the fibre output was imaged through an iris mounted on an x, y translation stage. The output is then either focused onto a highly multi-mode silica patchcord which was coupled to the BW-Tek USB spectrometer or onto the camera to observe core isolation/ selection. Incident power measurements were made with a pyro-electric detector (Laser Probe RkP-575). This experimental set-up is shown in figure 4.22.

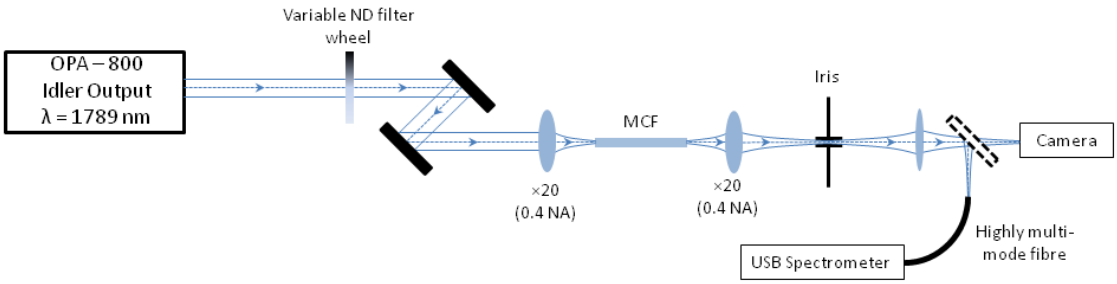

Figure 4.22: Experimental set-up measure the spectral power distribution contained in each core.

With the idler output of the OPA tuned to produce an output with a central pump wavelength of 1789 nm allowed for evanescent coupling to occur between cores. For incident pump energies of 90 nJ (input average power = 90 µW) significant spectral broadening effects were observed at the fibre output. The spectral comparison between the coupled core and one of the adjacent cores is shown in figure 4.23. This confirms the suspicion that the short wavelength radiation with respect to the pump experiences a greater degree of confinement and thus remains in the central coupled core. The red-shifted radiation is a Raman shifted soliton peak. The wavelength components of this peak undergo a higher degree of coupling due to the longer wavelengths generated in supercontinuum having a larger mode field diameter [82] than that of the pump and short wavelength components. Due to the equal spacing of the cores this soliton peak then continues to evanescently couple to all other outer lying cores. The *adjacent core* spectra in figure 4.23 shows the majority of the spectral power is situated on the longer wavelength side with respect to the pump. Peaks at 1794 nm (pump wavelength) and 1424 and 1194 nm also appear in the spectra. The peaks at 1424 and 1194 nm are particularly interesting as under low input power conditions no evanescent coupling was observed in the MCF at these wavelengths.

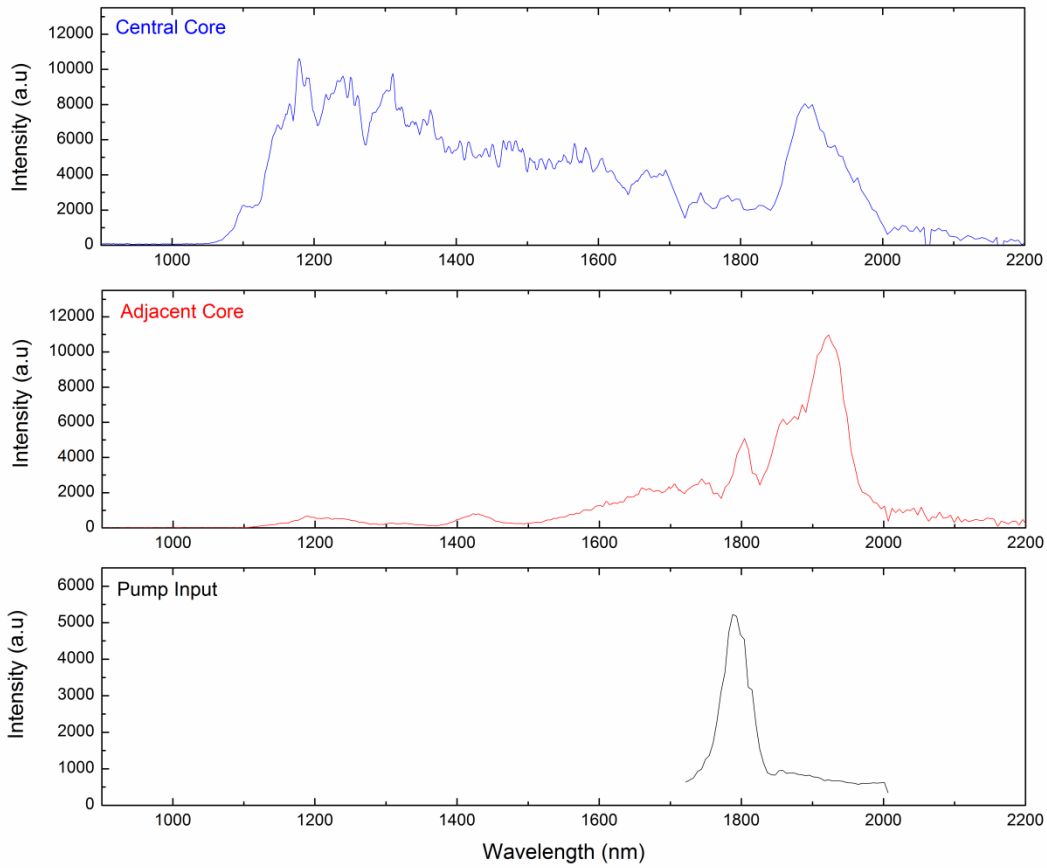

Figure 4.23: Graphs showing the spectral power distribution of the central core – blue line, adjacent core – red line. The pump input spectrum is shown for comparison – black line

By varying ND filter wheel (and thus varying the incident power) was found to vary the peak wavelength of the red-shifted radiation contained in the adjacent cores. The higher the incident power the greater the red-shift. If this red-shifted radiation is a soliton peak undergoing SSFS due to SRS from the material then the decreased interaction with the blue-shifted radiation should allow for a greater SSFS '*walk-off*'. A limiting factor of the SSFS for this fibre would be the increasing absorption coefficient of silica for wavelengths greater than 1900 nm. If a 7-core MCF, i.e. a central core with 6 outer lying cores, then a possible implementation of this effect could be to mix then re-combine the soliton radiation with that of the pump wavelength inside a nonlinear crystal to allow for harmonic generation. More complex and monolithic devices could also be fabricated via ultrafast laser inscription. This has the added advantage of independently varying the core structures – such as terminating the central core a designated distance along the length of the waveguide to ensure maximum power in the

outer lying core. Such a device could be fabricated out of mid-IR transmissive glass to allow for a greater exploitation of the un-impinged SSFS.

4.5. Conclusions

The roles of different spectral broadening mechanisms were investigated by observing their on-set and subsequent evolution in silica based PCFS. The contribution of these mechanisms to the overall supercontinuum generation was investigated for pump wavelengths on either side of the fibres zero dispersion wavelength. This experimental data was then used to aid numerical models of nonlinear pulse propagation in PCFs. The efficiency of the supercontinuum generation process was shown to be increased by matching the coupled pump radiation to that of one of the principal axis of a highly birefringent core. When the pump radiation polarisation state was launched off-axis into the fibre the power was split between the two polarisations and thus reducing the nonlinear interaction. The long wavelength edge of the supercontinuum generation in the silica PCFs was found to be limited by transmission window of silica. Research conducted on extending this wavelength range further into the infrared was demonstrated by utilising a lead bismuth galate microstructered fibre. Finally ways of tailoring the supercontinuum generation by limiting the interaction of different nonlinear optical processes were investigated by studying nonlinear pulse propagation in multi-core fibre. Through correct selection of pump wavelength it was demonstrated that the interaction of optical solitons and the short wavelength Cherenkov radiation formed via soliton fission could be restricted. The ultrafast laser inscription technique is an ideal candidate for fabrication of devices that can exploit this effect due to its large array of design freedoms. Prototype fabrication would require tailoring of parameters such as; adjusting core size, core separation and varying separation along waveguide length – all of which can be varied in the ULI fabrication process in a highly cost effective manner with the additional benefit of short fabrication times.

Chapter 5. Saturable absorption in aligned silver nanoparticles and single walled carbon nanotubes

5.1. Introduction

In this chapter the nonlinear optical process of saturable absorption will be introduced, some examples of how this mechanism can be implemented in photonic devices are then listed. This leads on to measurement of saturable absorption effects in two nanostructured materials via the z-scan experimental technique. The nonlinear transmission of silver nanostructures embedded on a silica matrix was investigated at a wavelength of 527 nm. The silver nanoparticles were elliptically shaped and were orientated in the same axis. The saturable absorption was therefore expected to be highly dependent on the polarisation of the input field. Saturable absorption effects of carbon nanotubes embedded in a polymer film were then investigated at a wavelength of 1570 nm. The main focus of this research was to study the nonlinear transmission of the single walled carbon nanotubes (SWCNT) for field strengths much greater than that of the saturation irradiance.

5.2. Saturable absorption

Saturable absorption is a nonparametric nonlinear optical process where high field strengths can decrease the absorption coefficient of a material. This process is intensity dependent and therefore means that higher field strengths will experience higher transmission through the material. This can often lead to full material transparency. The field dependent absorption, α, for a saturable absorbing material can be defined as [83];

$$\alpha = \frac{\alpha_0}{1 + \frac{I}{I_s}} \qquad \textit{Eq.(5.1)}$$

where α_0 is the linear absorption coefficient of the material, I is the field intensity of the laser and I_s is the saturation intensity of the material and corresponds to the intensity at

which the materials transmission is 50% of its full inversion value. For a two-level saturable absorbing system I_s is defined as:

$$I_s = \frac{h\nu}{\sigma\tau} \qquad \textit{Eq. (5.2)}$$

where $h\nu$ is the photon energy, σ is the absorption cross section and τ is the excited state life-time. Saturable absorbing materials have a number of useful applications in photonic devices the most widespread of which is for allowing lasers to passively modelock [84]. The effect was first demonstrated shortly after the advent of the laser by injecting saturable absorbing dyes into the laser cavity [85]. In terms of passively modelocking a laser cavity the saturable absorbing material would ideally have a large increase in transmittance for high field strengths, ΔT, and have an ultrafast recovery time. Such saturable absorbing materials are classed as 'fast' as these will lead to the shortest pulses from the laser cavity and the loss from the material is dependent on the instantaneous power of the incident pulse. Semiconductor saturable absorbing mirrors (SESAMS) were a successor to the saturable absorbing dyes and widely used in a number of commercially available ultrashort laser systems. SESAMS consist of Bragg structure that has a high reflectance at the laser wavelength, bonded to which is a saturable absorbing material – higher field strengths will experience a higher transmission through the material and thus a higher reflectance from the Bragg mirror. SESAMS have to be designed for a specific wavelength range and are typically fabricated for commercial laser systems via metal-organic chemical vapour deposition (MOCVD) or molecular beam epitaxy (MBE). To optimise the SESAM recovery time one must carefully design the Bragg structure, i.e. chirping the Bragg structure to compensate for opposite intra-cavity chromatic dispersion, in addition to the appropriate selection of the saturable absorbing material and its thickness. Recently materials such as SWCNTs [86] and graphene [87] have emerged as potential alternatives to SESAMS as they readily offer ultrafast recovery times [88] and in the case of graphene the saturable absorption process occurs over a broad wavelength range [89].

5.3. Saturable absorption in aligned silver nanoparticles on a silica matrix

Fabrication of the nanostructured sample was carried out by the department de Optica of the Centro de Investigación Científica y de Educación Superior de Ensenada, Mexico. Silver ions were implanted into a 20 × 20 × 1 mm^3 ultra-high purity silica (NSG ED-C) glass substrate at 2 MeV at room temperature via the metal ion implantation technique. The implanted samples were then thermally annealed at 600 °C in a 50%N_2 + 50%H_2 reduced atmosphere for one hour. A metal ion fluence of 7×10^{16}Ag/ cm^3 with a projected range of 0.9 µm was measured via Rutherford backscattering spectroscopy. In order to elongate the silver nanoparticles the sample was then irradiated with higher energy, 8 MeV, Si ions with a fluence of 2.3×10^{16} Si/cm^3 at an angle of 45° with respect to the sample surface. This resulted in a 0.5 µm thick layer of spheroid silver nanoparticles 1 µm below the surface of the silica glass subtstrate. Figure 5.1 shows a TEM micrograph of a composite film with the implanted silver nanoparticles

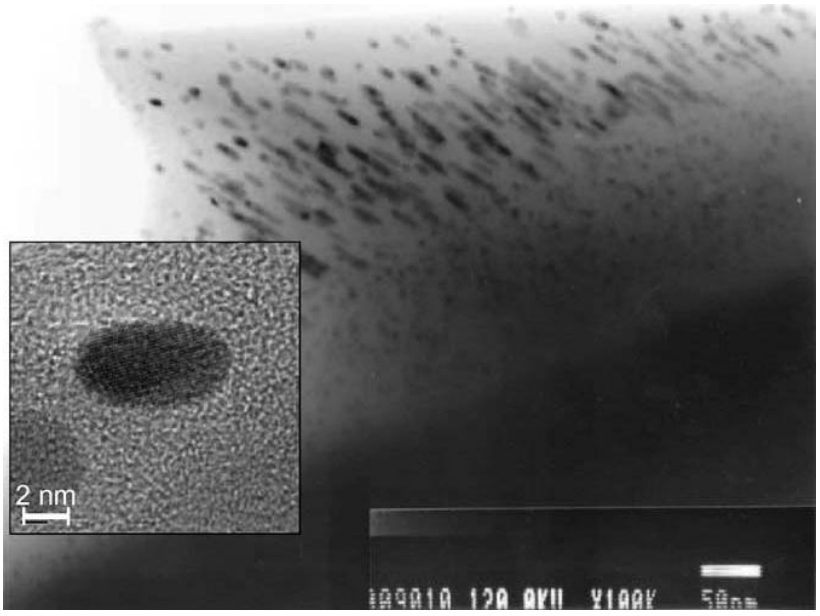

Figure 5.1: TEM micrograph of aligned silver nanoparticles deposited on a composite film

The linear absorption characteristics of the sample for orthogonal polarisations were investigated in the visible wavelength range. Figure 5.2 shows absorption spectra recorded for the sample for polarisations of M00P00 aligned parallel to the short axis of

the nanostructures and M00P90 which is aligned perpendicular to the short axis of the nanostructures.

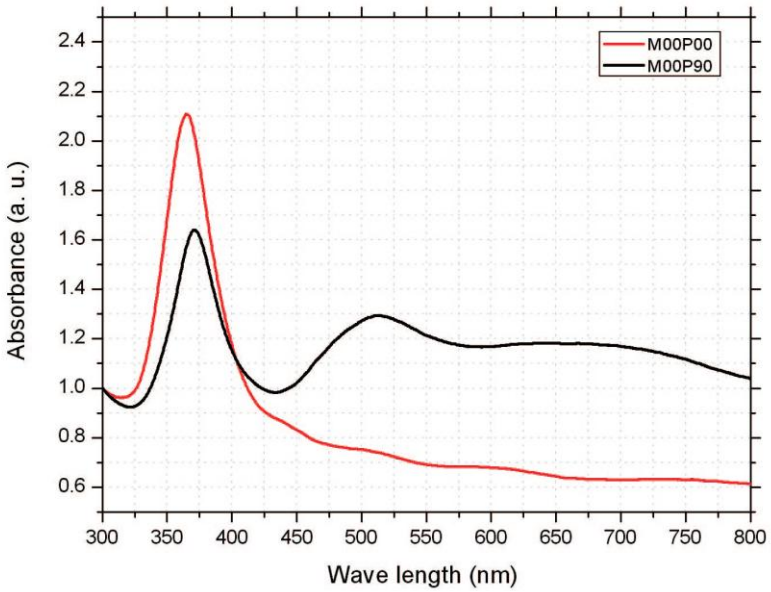

Figure 5.2: Graph showing linear absorbance for input polarisations parallel (M00P00) and perpendicular (M00P90) to the short axis of the aligned nanostructures

Figure 5.2 clearly shows two different absorption bands for orthogonal polarisations. This is due to the different surface-plasmon resonance conditions for the separate polarisations. The sample's saturable absorption characteristics were investigated at a wavelength of 527 nm which lies close to the absorption peak that appeared in the M00P90 spectra.

5.3.1. Z-scan saturable absorption measurements

The output of the femtosecond OPA system outlined in section 3.3 is adjusted to produce the desired 527 nm wavelength output. This wavelength was obtained by taking the fourth harmonic of the idler output. The pulse repetition rate was 1 kHz. This was then directed through the z-scan set-up outlined in section 2.7 with the addition of a half-wave plate and polariser to the beam path. These were placed before the z-scan focusing lens. The ref and open aperture detectors were silicon detectors (Newfocus 2032) and incident power measurements were made using the Newport 918-UV low

power photodiode. The beam was focused with a 20 cm focal length lens to a spot size of 33 µm. The pulse duration was measured to be 233 fs.

Figure 5.3 shows two z-scan traces conducted on the sample for two orthogonal polarisations. The insert indicates the input field polarisation with respect to the aligned spheroid nanoparticles. The input pulse energies were 145 nJ for both z-scans.

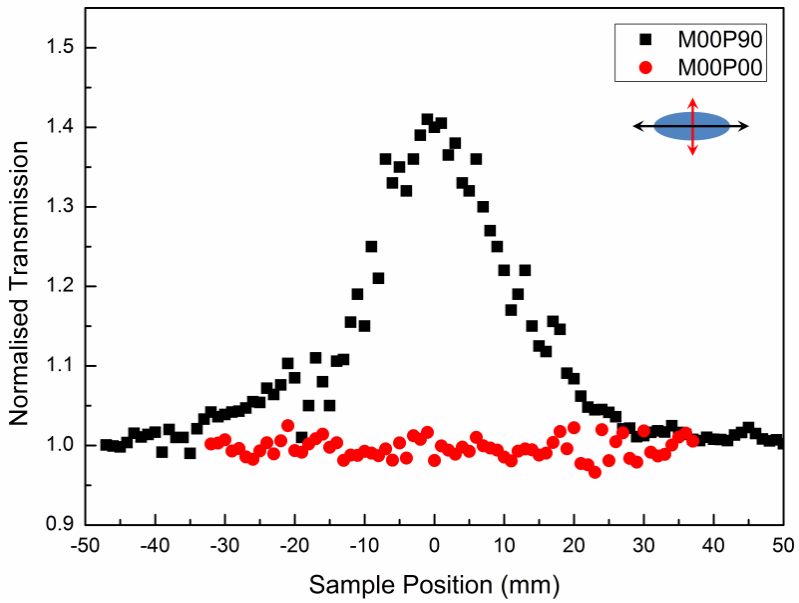

Figure 5.3: Open aperture z-scan traces conducted at a wavelength of 537 nm with pulse energies of 145 nJ for polarisations aligned parallel (M00P00, red data points) and perpendicular (M00P90, black data points) to the short axis of the aligned nanostructures.

From figure 5.3 it is evident that there is a strong polarisation dependence on the saturable absorption. The z-scan conducted with the polarisation aligned to the long axis of the spheroid nanostructures clearly shows the effect of saturable absorption, where-as no such effect is observed for the orthogonal polarisation. Z-scans are conducted for input field polarisations with 15° increments to confirm the increase in the saturation intensity as the polarisation is aligned to the short-axis of the spheroid nanostructures. For each polarisation the incident pulse energy was increased until a noticeable saturable absorption effect was observed. These z-scans were then fitted using equation 5.1 and assuming a Gaussian beam profile at each z-position. Figure 5.4 shows the trend of how I_s varied with input field polarisation with respect to the aligned nanoparticles. Saturable absorption effects for polarisation angles of 90° were observed for pulse

energies as low as 10 nJ where-as for input field polarisations of 0° pulse energies as high as 300 nJ had to be used in order to observe saturable absorption effects. The saturation fluence was calculated to be approximately 28 times higher for input polarisation angles of 0° compared to input polarisations of 90°.

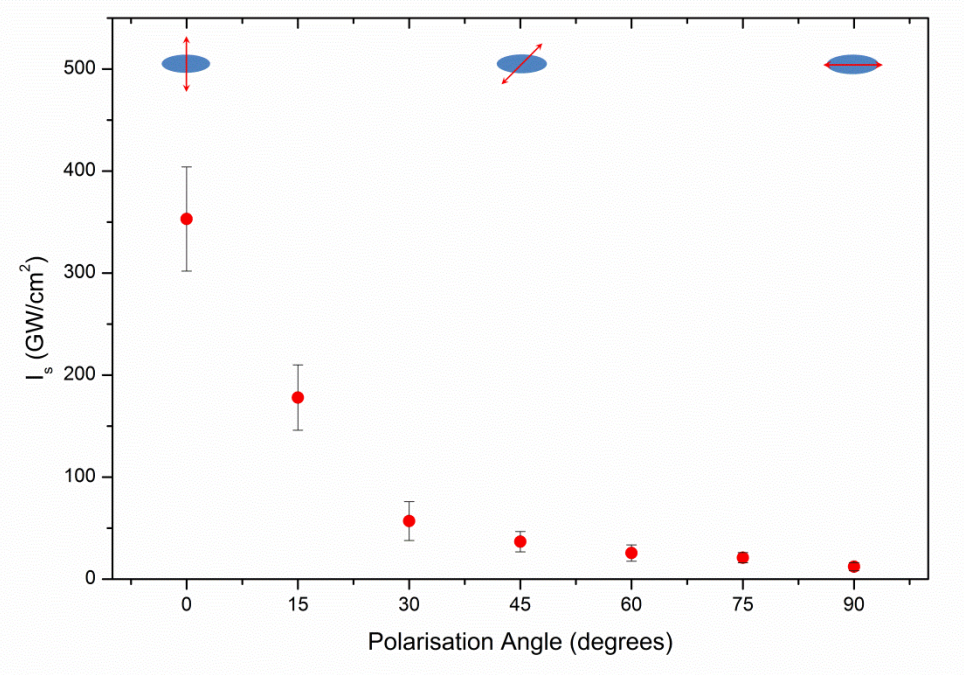

Figure 5.4: Graph showing I_s for various polarisations between 0° and 90°inferred from z-scan measurements

5.3.2. Discussion

The highly anisotropic nature of the saturable absorption nonlinear process in aligned silver spheroid nanostructures has been demonstrated via the open aperture z-scan experimental technique. The saturation intensity for varying incident polarisation angles was calculated by observing their respective threshold of saturable absorption in z-scan traces then applying the irradiance at focus to a two-level saturable absorption model.

5.4. Saturable absorption in carbon nanotubes

The single walled carbon nanotubes (SWCNT) were fabricated via the laser ablation technique [90]. This sample was provided by the Nanomaterials and Spectroscopy Group in the Department of Engineering at The University of Cambridge. The diameter

of the carbon nanotubes determines their absorption cross-section, changing the growth temperature allowed the control of the SWCNT diameter distribution and thus working saturable absorption range [91]. Here the growth conditions were selected to allow for strong absorption in the telecommunications L-band (1565 - 1625 nm). The CNT solution is then mixed with a PMMA solution before undergoing ultracentrifugation. A thick SWCNT PMMA film is produced after slow evaporation in vacuum chamber. The resulting film had an absorption peak at a wavelength of 1600 nm with SWCNT diameters of 1.4 nm.

The femtosecond OPA system was adjusted so that the signal output produced an output with a central wavelength of 1570 nm. This output was then heavily attenuated before being directed through the z-scan set-up outlined previously in section 3.3. Effects of saturable absorption are observed for pulse energies as low as 2 nJ which corresponded to an irradiance of 0.42 GW/cm^2 incident onto the sample. The saturable absorption threshold was found to be polarisation independent. This was in agreement with previous investigations into saturable absorption effects conducted on SWCNTs [92] as there was no set distribution of orientation of the SWCNTs. Figure 5.5 shows the evolution of the saturable absorption of the SWCNT PMMA film for pulse energies of 5, 15, 30 and 40 nJ. From figure 5.5 one can observe that despite the low threshold the subsequent increase of the maximum ΔT with pulse energy (measured at Z=0) is low. An increase in transmittance of approximately 35% and thus full inversion is observed with an incident irradiance of 8.45 GW/cm^2 which corresponded to input pulse energies of 40 nJ.

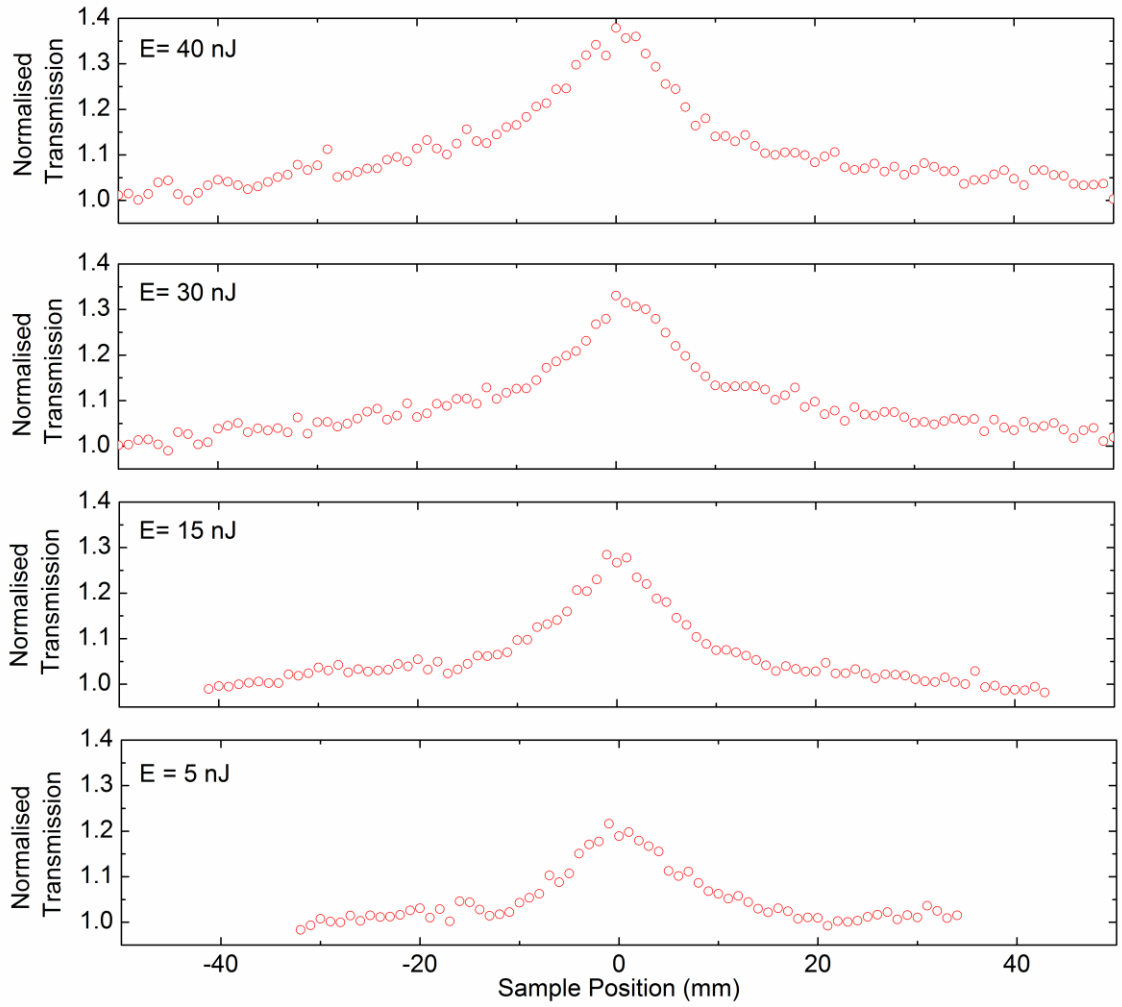

Figure 5.5: Open aperture z-scan traces showing the evolution of saturable absorption with incident pulse energy in SWCNTs embedded on a PMMA film at a wavelength of 1550 nm.

Due to the low gradient of the maximum ΔT versus pulse energy and subsequent broadening of the saturable absorption region, it was suspected that competing nonlinear absorption and saturable absorption effects were occurring within the SWCNT sample. This was predicted as nonlinear absorption has been demonstrated previously in SWCNT, but away from wavelengths were they exhibit a strong linear absorbance [93].

From figure 5.5 above it can be seen that the threshold for nonlinear absorption is much higher than that of the saturable absorption, therefore z-scan experiments were then conducted at much higher pulse energies to demonstrate and observe clear effects of nonlinear absorption occurring in the SWCNT sample. For pulse energies of approximately 95 nJ a dip which was observed in the saturable absorption peak of the z-

scan trace. This dip was highly confined to the focal region of the beam. The irradiance at focus was approximately 2×10^{14} W/m^2. This dip due to nonlinear absorption meant that the plane of greatest ΔT occurred 2 mm away from the focal plane. Figure 5.6 shows the evolution of the competing saturable absorption and nonlinear absorption effects in SWCNTs for pulse energies of 105, 140, 200 and 290 nJ. The z-scan traces in figure 5.6 are not normalised to 1.0 as due to the high irradiance saturable absorption effects were present even for z-positions of ±50 mm.

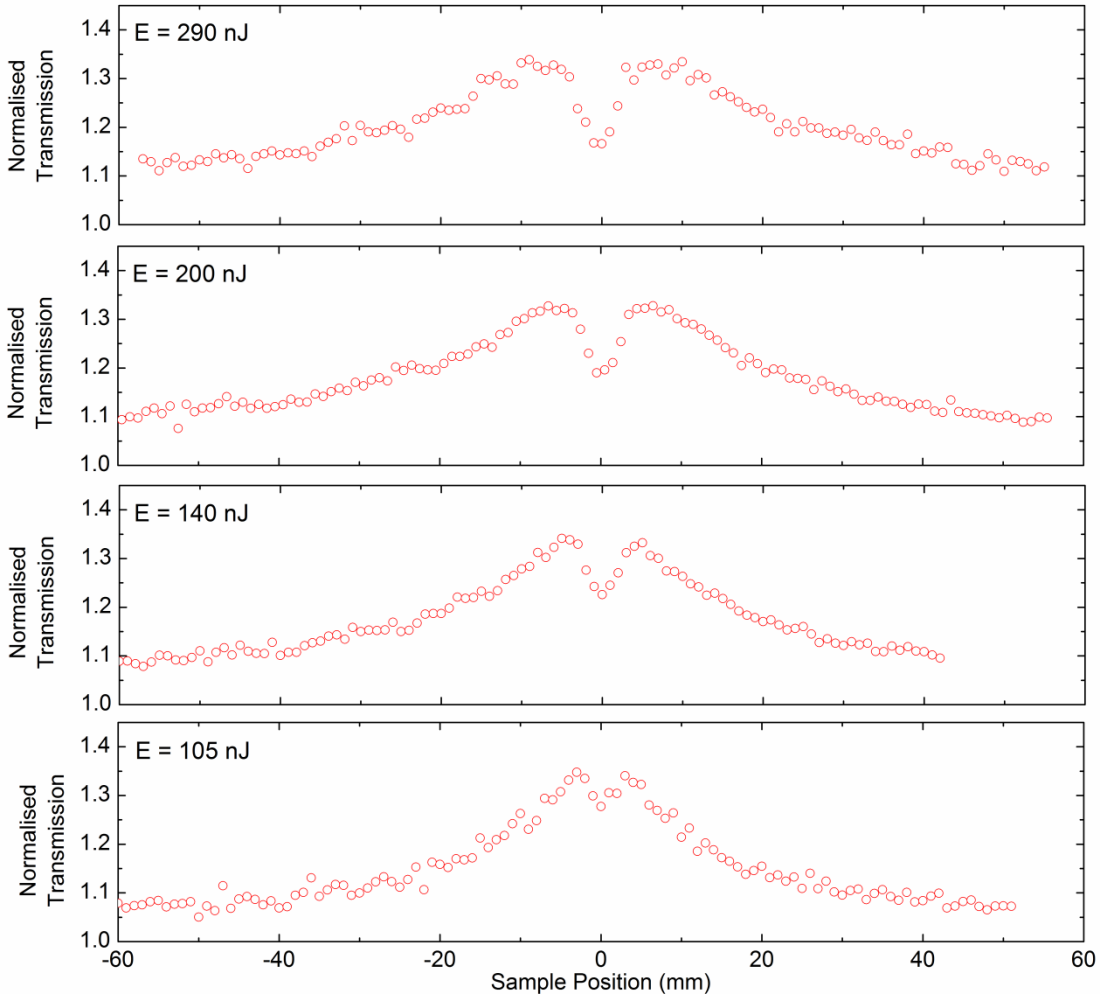

Figure 5.6: Open aperture z-scan traces conducted with high pulse energies showing the competing saturable absorption and nonlinear absorption processes in SWCNTs embedded on a PMMA film at a wavelength of 1550 nm.

From figure 5.6 it can be observed that as the pulse energy, and thus irradiance in and around the focal plane is increased, there is an increase in the amount of nonlinear absorption in the z-scan trace. Due to this effect the position of maximum transmission is located further from the focal plane. For the highest pulse energy z-scan trace shown

in figure 5.6 the transmission at the focal plane is approximately equal to that obtained far from the focal plane of the SWCNT sample. This translated to an irradiance at the focal plane of 6.2×10^{14} W/m^2 where the amount of saturable absorption was cancelled out by nonlinear absorption. No optical damage was observed on the SWCNT PMMA film after exposure to these high irradiances, this fact is re-enforced by the symmetry of the z-scan traces about the focal plane – the saturable absorption effect recovers to the same level after being translated through the focal plane. Additionally for the z-scan conducted with pulse energies of 290 nJ there is approximately 6 mm in length on either side of the focal plane where there is a plateau in ΔT. By taking the scanning knife-edge data which was used to measure the beam size with z-position (and the focal spot size) it is possible to calculate the irradiance along the beam path. This data can be used to approximate a trend of ΔT versus irradiance from the z-scan traces. Figure 5.7 shows the calculated spot size of the beam along z and the fitted Gaussian beam profile.

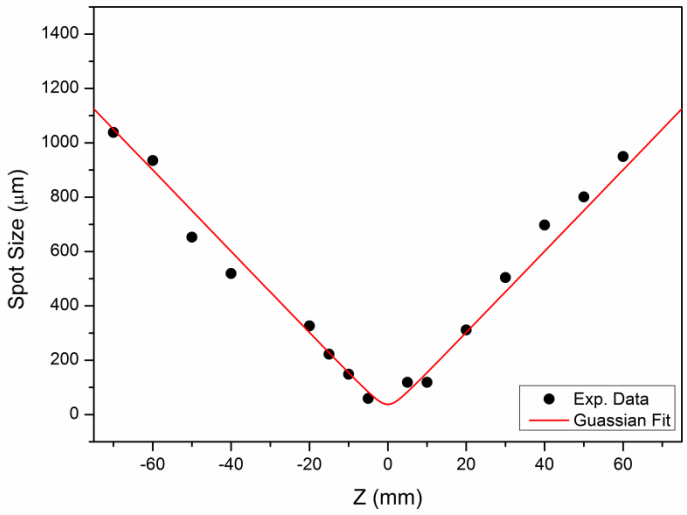

Figure 5.7: Graph showing beam width measurements (black data points) measured along z-axis fitted to the equation for a Gaussian curve with a beam waist of 37 μm.

Using this Gaussian fit to estimate the beam size for a respective z-position allows for the irradiance for each z-position to be calculated. Essentially each point of an experimental trace can now be used to display SWCNT sample transmission with irradiance. Figure 5.8 displays data from two z-scans one conducted with pulse energies of 35 nJ and with much higher pulse energies of 290 nJ. The plateau in the increase of transmission is observed for irradiances of approximately 2.5×10^{13} W/m^2 to

9.5×10^{13} W/m^2 after which nonlinear absorption affects begin to dominate and lower the effects of saturable absorption. To ensure that the nonlinear absorption observed at high irradiances was caused by the SWCNTs and not the PMMA film they were deposited onto, z-scans were conducted with pulse energies of 300 nJ for both a blank PMMA film and one with SWCNT PMMA film composition. These z-scan traces are shown in figure 5.9.

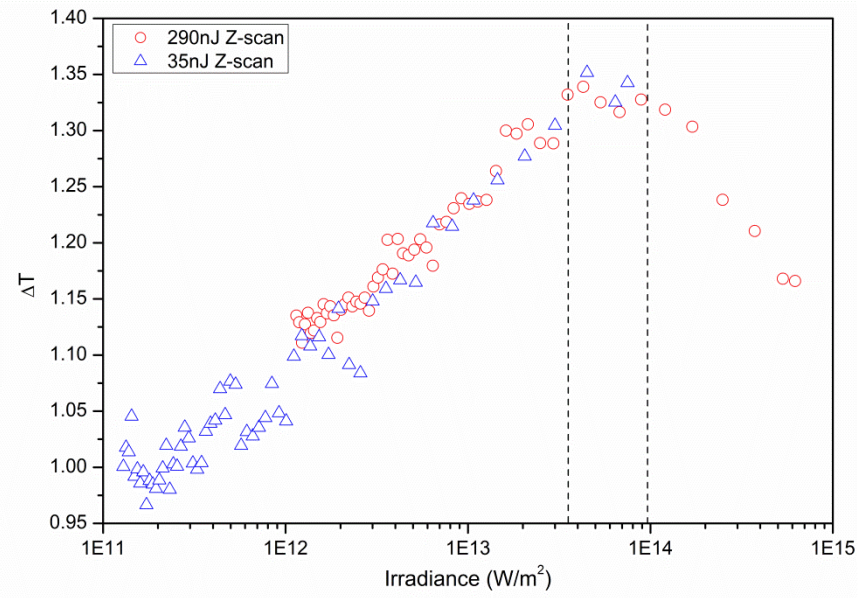

Figure 5.8: Graph showing the normalised transmission with increasing irradiance taken from two z-scan traces.

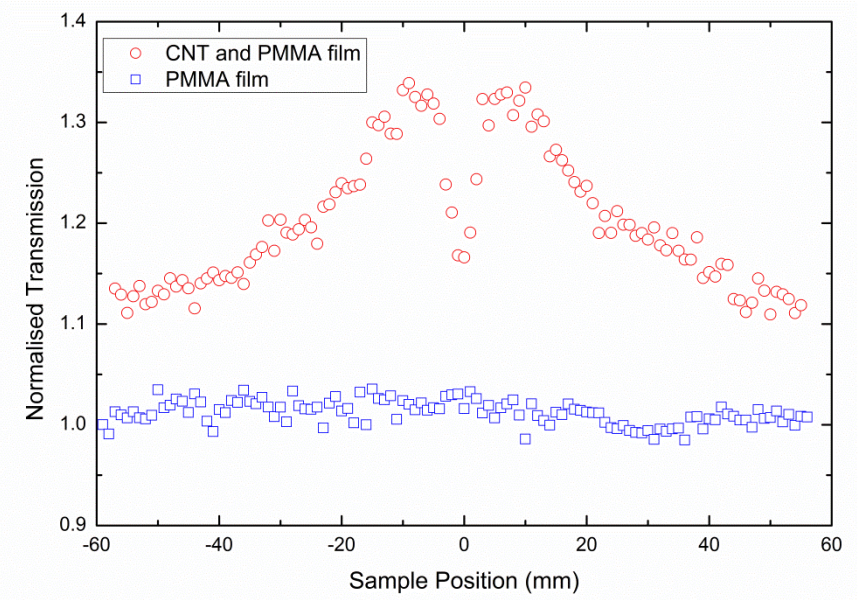

Figure 5.9: Shows z-scan data conducted with 300 nJ pulse energies on a PMMA film with/without embedded SWCNTs.

From figure 5.9 the PMMA material without embedded SWCNTs exhibited no transmission change in the z-scan trace. Therefore the effects of saturable absorption and multi-photon absorption observed in figures 5.5, 5.6, 5.8, 5.9 can be attributed solely to the embedded SWCNTs.

5.5. Discussion

Saturable absorption effects were observed in a SWCNT polymer film measured via the z-scan experimental technique. Through measurements conducted on the polymer film at high irradiances the SWCNT exhibited a coupled effect of nonlinear absorption and saturable absorption at high irradiances. At irradiances of greater than 9.5×10^{13} W/m^2 the contribution of nonlinear absorption effect was found to impede the effect saturable absorption. The level of nonlinear absorption was not found to decrease the transmission of the SWCNT sample past that of the linear transmission of the sample i.e. the decrease of transmission due to the nonlinear absorption could only *cancel out* the effects of saturable absorption. Through measuring the beam diameter at numerous z-positions and fitting these to the values to the Gaussian beam equation the irradiance at each z-position was calculated. This was then used to plot irradiance versus increase in transmission. Through this method the irradiance for greatest increase in transmission was calculated to be 2.5×10^{13} W/m^2. Both the PMMA film with and without embedded SWCNTs were exposed to irradiances of up to 6.2×10^{14} W/m^2 and no optical damage was observed on either film. Conservation of the coupled nonlinear and saturable absorption effect was observed after exposure to this field strength. This indicates that the SWCNTs themselves were not damaged during the experimental procedure.

5.6. Conclusion

Two different classes of nanostructured materials were studied using the open aperture z-scan technique. Firstly, a silver nanoparticles on silica substrate was studied at visible wavelengths. Secondly, a carbon nanotube sample was studied in the near infrared. Both types of samples exhibited similar large changes in transmission – up to a forty percent increase. The differences in the saturable absorption behaviour between the silver nanoparticles on silica substrate and the SWCNTs in PMMA film are observed.

The most striking difference is their respective sensitivity to polarisation. The aligned nanoparticles show a very strong dependence of the saturable absorption intensity on the angle of linear polarisation with the strongest saturable absorption occurring when polarisation is aligned with the long axis of the ovoid form of the nanoparticle. The randomly distributed SWCNT in polymer exhibited no dependence on the direction of polarisation. The random distribution is attributed to the fabrication technique. The SWCNT sample also demonstrated the interplay between saturable absorption and nonlinear absorption. A distinct dip with a much narrower width compared to the saturable absorption peak emerged at high pulse energies in the open aperture z-scan. From the results presented, it was clear that the nonlinear absorption was a limiting factor for the operation of the sample as a saturable absorber element.

Chapter 6.Spectral broadening in ultrafast laser inscribed gallium lanthanum sulphide waveguides

6.1. Introduction

The work presented in this chapter focuses on the fabrication of ultrafast laser inscribed waveguides in gallium lanthanum sulphide glass. The main objective of this investigation was to fabricate a highly nonlinear mid infrared waveguide. This waveguide could then form the building block of a more advanced mid-IR devices and circuits. One area of application would be in the field of gas sensing due to the presence of many fundamental absorption lines of a wide range of molecular species that are situated throughout the Mid Wavelength Infrared (MWIR) spectral region. Outside of gas sensing applications a mid infrared waveguide circuit could be implemented in the fields of directed infrared countermeasures [94] and astrophotonics devices for IR imaging and detection [95]. Ideally the guiding structure would guide a single transverse mode to allow for stand-off spectroscopic analysis and have a symmetrical profile to enable low coupling losses to and from sources and detection devices respectively.

Ultrafast laser inscription was selected due to several reasons. The fabrication time is short, there is no need for clean room facilities and the process is a single step fabrication. Another important feature of ULI is the ability to write complex 3D structures once correct fabrication parameters have been identified. Other waveguide fabrication technologies that could have been used such as deposition of thin films either by pulsed laser deposition [96], RF sputter coating [97] or thermal evaporation [98] require processes such as wet-etching [99] or embossing [100] to fabricate the waveguide structure. These technologies are multi step processes and are all applicable for use with chalcogenide materials but in the context of mid infrared waveguide fabrication they are limited by long fabrication times due to the large size of structures required to achieve mid infrared guiding. Solution casting methods such as micro-moulding in capillaries (MIMIC) are etch free processes that can fabricate waveguide structures that are easily scalable for the mid infrared spectral range [101]. A mould

fabricated with recesses in the design of the desired device is held to a substrate material before a chalcogenide solution is flown through the channels. The sample is then heated to allow for the solution to solidify, after which the mould is then removed [102]. While fabrication processes like MIMIC are low cost there are numerous fabrication steps and the circuit designs are limited to two dimensions.

GLS was selected as the substrate material due to its high nonlinear refractive index 1.5×10^{-18} m^2W^{-1} and very low nonlinear absorption coefficient < 8×10^{-14} mW^{-1} at a wavelength of 1550nm. This offers potential benefits as the basis for a nonlinear switching device. It terms of ULI, previous work by Hughes et al. [59] demonstrated near infrared waveguide fabrication in GLS with structures that exhibited a small positive refractive index change and a small change in the Raman spectrum.

Section 6.2 introduces the basis of ULI before outlining the key parameters that have to be considered when fabricating structures with this method. Section 6.3 presents the fabrication parameters used to inscribe in GLS substrates. Section 6.4 then details the morphology of the inscribed structures before spectral broadening measurements are presented in section 6.5.

6.2. Ultrafast laser inscription

Tightly focusing ultrashort laser pulses inside a transparent material can permanently alter the optical properties of a material. The high field intensities in the focal volume induce nonlinear absorption processes which then transfer optical energy in the form of free-electron plasma. Due to the nonlinear nature of this process the material modification is limited to the focal volume inside the material substrate. By careful selection of inscription parameters this can induce a positive refractive index change. Waveguide formation inside the material can then be realised by simply translating the sample through the focal region. This allows for truly three dimensional inscription capabilities - thus it can be used in the fabrication of a number of complex optical devices such as; micro-fluidic devices [103], photonic lanterns for astrophotonics [104], quantum information processing circuits [105] and multi-core fibre couplers [106]. Due to the nature of the inscription process it can be used to fabricate structures in a number

of different glasses such as borosilicates [107], polycrystalline ZnSe [108], tellurites [109], ZBLAN [110] as well as polymer [111] and crystal structures [112].

In addition to the 3D writing capabilities it is a highly flexible inscription technique with a large number of variable parameters. The key inscription parameters and how they affect the ULI process are listed below.

- Pulse Energy

By controlling the amount of energy in an optical pulse one can control the amount of energy transferred to the material. This can drastically affect the type of modification induced in the material. For example one could induce a positive refractive index change, subwavelength nanogratings or form empty voids in the material simply by varying the pulse energy parameter [113].

- Pulse Repetition Rate

Accumulative heating can occur in the focal region of the material due to subsequent pulses arriving before the heat induced by the nonlinear absorption process has had time to diffuse away. Increasing the time between pulses, i.e. lowering the repetition rate, effectively allows each pulse to interact with the cold material. This can drastically alter the shape or size of structures inscribed in a material, particularly those with a low thermal conductivity [107].

- Laser Wavelength

The laser wavelength with respect to the band-gap of the material will govern the order of multi-photon absorption, i.e. 2, 3, 4 etc. photon absorption. For laser sources whose wavelength lies far from the band-edge, then the dominant absorption mechanism is a process known as tunnelling ionisation rather than multi-photon absorption. The Keldysh parameter can be used to determine the dominant factor for the nonlinear absorption process and is defined as [114]:

$$\gamma = \frac{\omega\sqrt{2mE_g}}{eE} \qquad \textit{Eq. (6.1)}$$

where e is the effective electron charge, m is the effective electron mass, E is the amplitude of the laser electric field oscillating at frequency ω, and E_g is the material band-gap. When $\gamma \gg 1$ multiphoton absorption dominates, when $\gamma \ll 1$ the tunnelling ionisation process dominates.

- Pulse Duration and temporal shape

The spatial distribution of energy density in the focal volume can be affected by the pulse duration due to nonlinear propagation inside the substrate material causing self-focusing/de-focusing of the laser beam [108].

- Polarisation

The polarisation of the incident beam with respect to the sample translation axis has been shown to influence the propagation losses in fused silica waveguides due to nanograting formation [115]. This is a case of the polarisation affecting the efficiency of the absorbed light. Therefore one can increase/decrease the threshold of the formation on nanogratings by varying the polarisation for a given pulse energy.

- Sample Translation Speed

Similar to the case of repetition rate, the sample translation speed can vary the extent of pulse to pulse overlap in the substrate material, but on a coarser scale. This allows for design freedom even for inscription laser sources that have a fixed repetition rate.

- Focusing Lens/ Objective

By changing the focusing objective one can alter the peak irradiance inside the sample without varying the average power or pulse energy of the laser. Varying the focusing objective also affects the focal volume and modified region cross-section.

While few of the above fabrication parameters vary in complete isolation from the others this still allows for the limitations of a particular inscription set-up, such as fixed

laser wavelength and pulse energy, to be overcome by varying other aspects of the inscription set-up to reach a desired fabrication need.

6.3. Ultrafast laser inscription of waveguides in gallium lanthanum sulphide

The waveguides were fabricated using a mode-locked Yb-doped fibre laser. The laser emitted 300 fs pulses with a repetition rate of 500 kHz. The central wavelength of the laser output was 1060 nm. The pulse train from the laser was set to be circularly polarised. The sample was mounted on air bearing stages and the pulse train was focused ~240 μm from the top surface using a 50× (0.67 NA) aspheric lens. The single-scan inscription technique was used. Fabrication power incident onto the sample was varied from 200 - 37 mW in decreasing increments of 10%. Four different sample translation speeds were investigated: 0.2, 0.4, 0.6 and 0.8 mms^{-1} with the substrate translation being perpendicular to the laser beam direction. After fabrication the input and output facets of the substrate were polished giving a sample length of 14.3 mm.

6.4. Waveguide morphology

The polished samples were examined under a microscope in transmission mode in order to view the modified regions. Figure 6.1 shows the effect of increasing pulse energy and sample translation speed on the cross-sectional size of the modified region. From figure 6.2 two types of modified structures are observed; one where the modified cross-section closely resembles that of the confocal parameter of the inscription lens, and another at high fabrication powers (>56 mW) where the waveguide facets exhibit a distinct ‘teardrop’ shape similar to those observed in other ULI structures [58, 59].

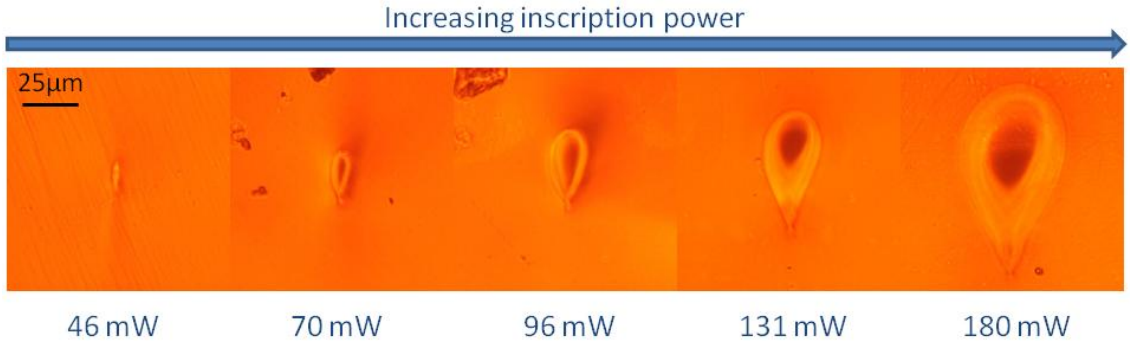

Figure 6.1: Optical micrograph of waveguide facet showing scaling with inscription average power. The pulse train travels from top to bottom of image.

The teardrop shape of the modified region is due to thermal accumulation and diffusion effects in the sample. The variation in the size of the teardrop structure was found to vary with fabrication parameters. For structures fabricated with high pulse powers the width and height of the structures written with a sample translation speed of 0.8 mm/s were significantly smaller than those written at 0.2, 0.4 and 0.6 mm/s. This effect diminished as the inscription power was decreased. This is summarised in figure 6.2 for fabrication pulse powers of 45 mW and 146 mW. This effect is predominantly due to thermal accumulation.

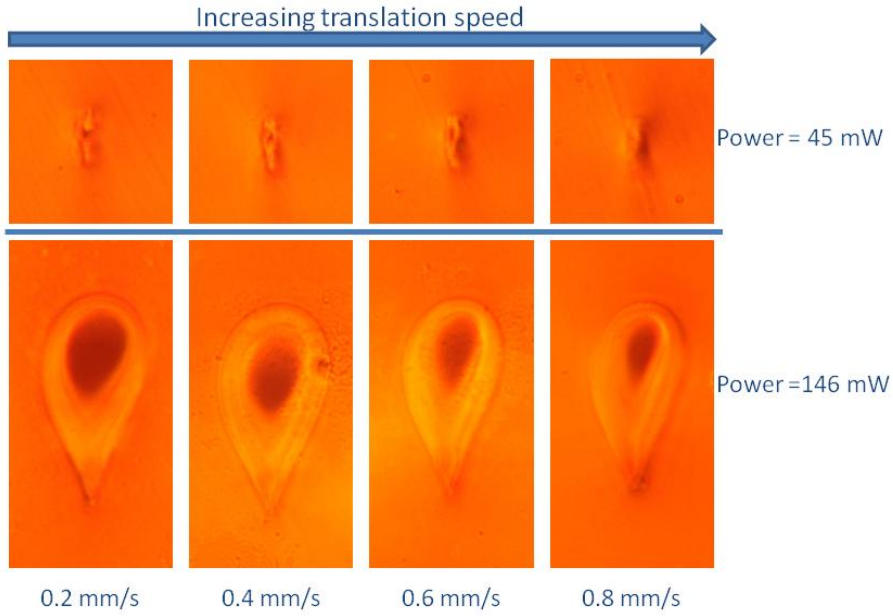

Figure 6.2: Optical micrograph of waveguide facet showing modified region cross-sectional size scaling with sample translation speed for high inscription average power (146 mW) and low inscription average power (45 mW)

Figure 6.3 plots the (a) width and (b) height of the modified structures for sample translation speeds of 0.2 and 0.8 mm/s.

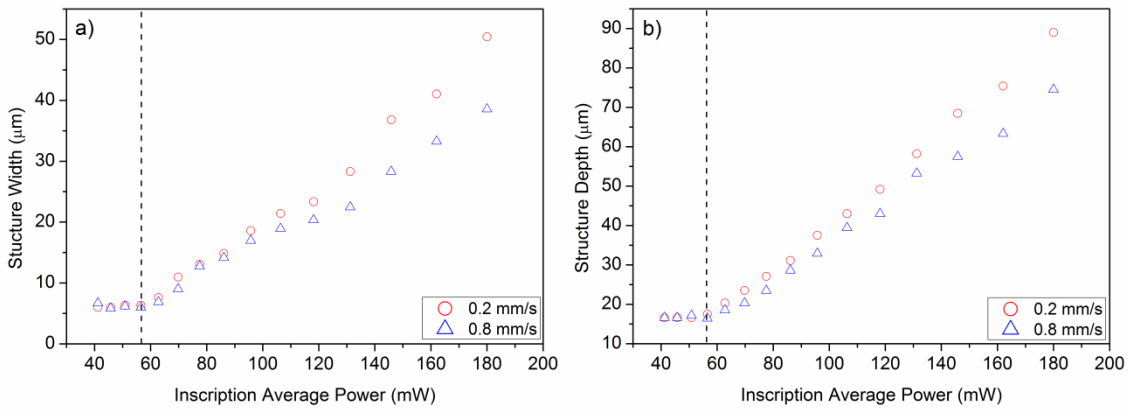

Figure 6.3: Graphs showing fabricated structure size with inscription average power. (a) stucture width, (b) structure height

From figure 6.3 it is observed that for average inscription powers greater than 56.5 mW, and therefore pulse energies of 113 nJ, the modified region size increases linearly with increasing inscription power for both the slowest and fastest sample translation speeds. These waveguides were fabricated with a pulse repetition rate of 500 kHz – the high repetition rate regime. This coupled with the fact that GLS has a relatively low transition temperature (580°C) and a thermal conductivity of 18 W/ K cm can explain the dominance of thermal effects thus explaining the steeper gradient for modified structure width and depth vs. inscription average power for slow sample translation speeds. For low inscription pulse energies, i.e. < 91.5 nJ, the modified structure size shows negligible variation with sample translation speed and therefore have a different dominant modification process.

Self-focusing of the laser pulses within the GLS substrate was also observed, as the location of the modified regions with respect to the surface of the substrate decreased as the inscription power increased. The effect of the self-focusing was found to be independent of sample translation speed. This extent of self-focusing as a function of inscription power is summarised in figure 6.4 where the distance to surface was measured from the top of the photo-darkened modified region.

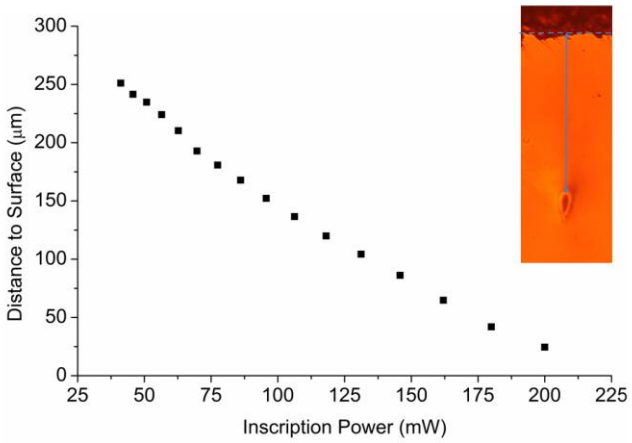

Figure 6.4:Graph showing waveguide structure depth with inscription power

This large self-focusing effect was expected due to the large nonlinear refractive index of GLS at 1550 nm which was measured to be 1.5×10^{-18} m^2 W^{-1}. The critical power for self-focusing is defined as [116]:

$$P_{crit} = \frac{\alpha\lambda^2}{4\pi n_0 n_2} \qquad \textit{Eq. (6.2)}$$

where λ is laser wavelength and α is a numerically calculated value for the spatial distribution of the beam, which for a Gaussian beam profile is calculated to be 1.8962, n_0 and n_2 are the materials linear and nonlinear refractive index terms respectively. Using the linear refractive index for {65} Ga_2S_3: {32} La_2S_3:{3} La_2O_3 of 2.398 [117] and using the nonlinear refractive index of this GLS composition calculated at 1550 nm as a conservative estimate its nonlinear refractive index at a wavelength of 1064 nm gives a critical power for self-focusing of ≈ 4.75 kW. The lowest average power used for inscription was 37 mW which gives a peak power of 24.7 kW which is over 5 times higher than that of the self-focusing threshold. Every inscribed structure was found to have manifested a positive refractive index change in relation to the un-modified GLS even for fabrication pulse energies as low as 74 nJ. The guiding characteristics of the structures were then tested at a range of wavelengths.

6.5. Spectral broadening measurements

The guiding characteristics of the inscribed structures were then examined at near and mid-IR wavelengths using the wavelength tuneable femtosecond source outlined in section 2.7. The wavelengths selected for investigation were 1550, 2485 and 3850 nm. Structures that were found to guide a single transverse mode at the investigation wavelengths were then tested for their nonlinear guiding properties The material ZDW of GLS lies in the mid-IR spectral region at approximately 4 µm, therefore it is expected that as the investigation wavelengths approach this ZDW an increase in the nonlinear spectral broadening will be observed.

6.5.1. Waveguide characterisation - 1550 nm

To ensure no nonlinear guiding effects were occurring in the waveguide structures the OPA output was heavily attenuated. This was then coupled to the waveguides by a 20× (0.4NA) silica microscope objective. The input coupling objective was mounted on an x, y, z manual translation stage (Elliot Scientific MDE122) and the substrate was mounted on a 4- axis x, y, pitch yaw translation stage (Thorlabs MBT401). The output facets of the waveguides were imaged using another silica 20× (0.4 NA) and imaged onto an Electrophysics camera (Model 7920A). The camera was connected to a computer with a frame grabber card. A USAF 1951 test resolution pattern was imaged in the same configuration in order to calibrate the mode size etc. This mode imaging experimental set-up is shown in figure 6.5.

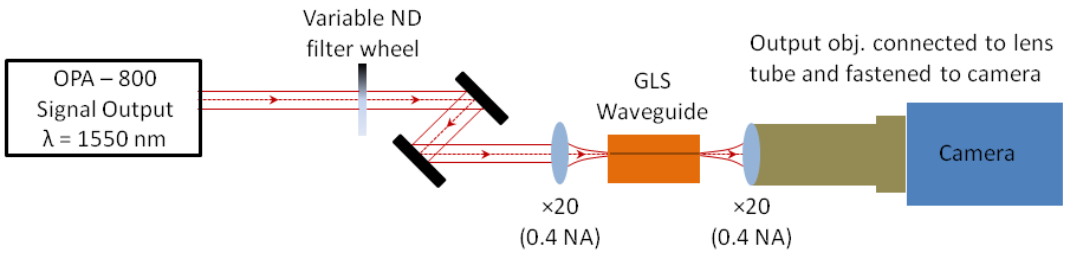

Figure 6.5: GLS waveguide mode imaging set-up.

At this wavelength the structures inscribed with average powers of 37 and 41 mW and therefore incident pulse energies of 74 and 82 nJ guided a single transverse mode for all four scan speeds. On inspection a large number of structures inscribed with low pulse energies were found to guide a single transverse mode at 1550 nm. Structures written with higher pulse energies were found to guide an increasing number of multiple modes.

Figure 6.6 shows a waveguide facet, the mode profile and intensity line plots for the x and y axis of the guided mode. The structure was written with pulse energies of 82 nJ and a translation speed of 4 mm/s. The structure guided a single transverse mode with a $1/e^2$ diameter of 8.8 µm – which is 95% mode matched to that of smf-28 at a wavelength of 1550 nm. This was calculated using the Gaussian mode overlap integral, as defined in equation (6.3) [118].

$$C \approx \frac{4a^2xy}{(a^2+x^2)(a^2+y^2)} \qquad \textit{Eq. (6.3)}$$

where a is the radius of the optical fibre and the x and y parameters are the horizontal and vertical radii of the waveguide mode respectively.

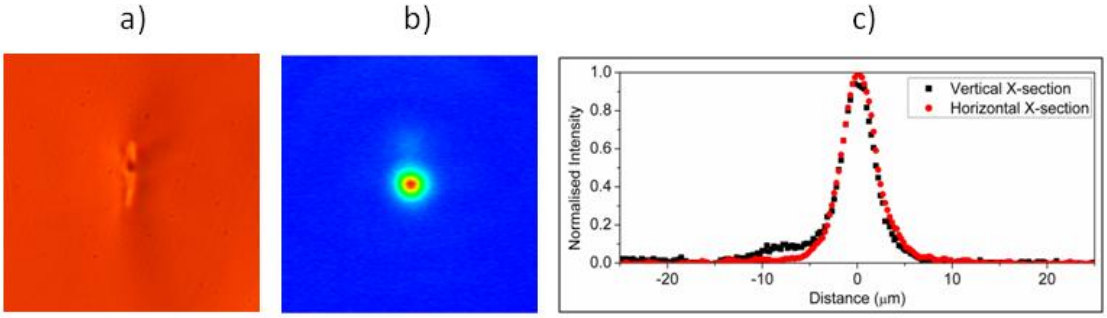

Figure 6.6: (a) Optical micrograph of waveguide facet, (b) corresponding 1550 nm mode image, (c) intensity line plots of guided mode.

The nonlinearity of the above waveguide was then investigated by increasing the input average power of the 1550 nm light and observing the spectrally broadened output. Figure 6.7 shows the experimental configuration for the continuum investigation. The

waveguide output was collimated by a 20× (0.4 NA) silica objective and coupled to a spectrometer (Ocean Optics NIR512/ BWTek BTC500E) via a 600 µm diameter core multimode silica patchcord. A variable neutral density filter wheel was used to vary the power output of the OPA before being coupled to the test waveguide.

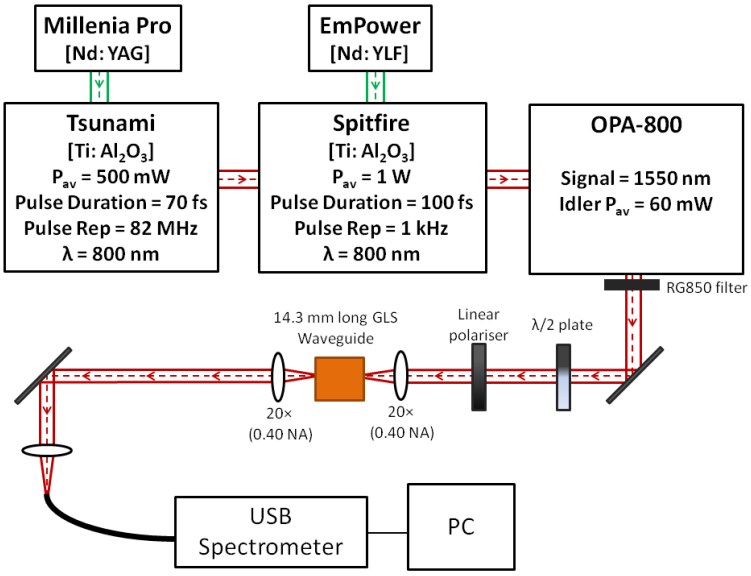

Figure 6.7: Experimental set-up for continuum investigation

Figure 6.8 shows the evolution of the spectral broadening with pump energy. At the -15 dB points the continuum spanned 462 nm from 1293 to 1755 nm when pulse energies (measured before coupling objective) of 115 nJ are coupled to the waveguide. The focusing spot size of the microscope objective was measured to be 6.7 µm which would incur a 0.35 dB coupling loss to the waveguide facet. Taking into account the reflected power due to the Fresnel reflection at the input facet meant that the maximum attainable coupled pulse energies to the waveguide were 88.5 nJ from 115 nJ incident.

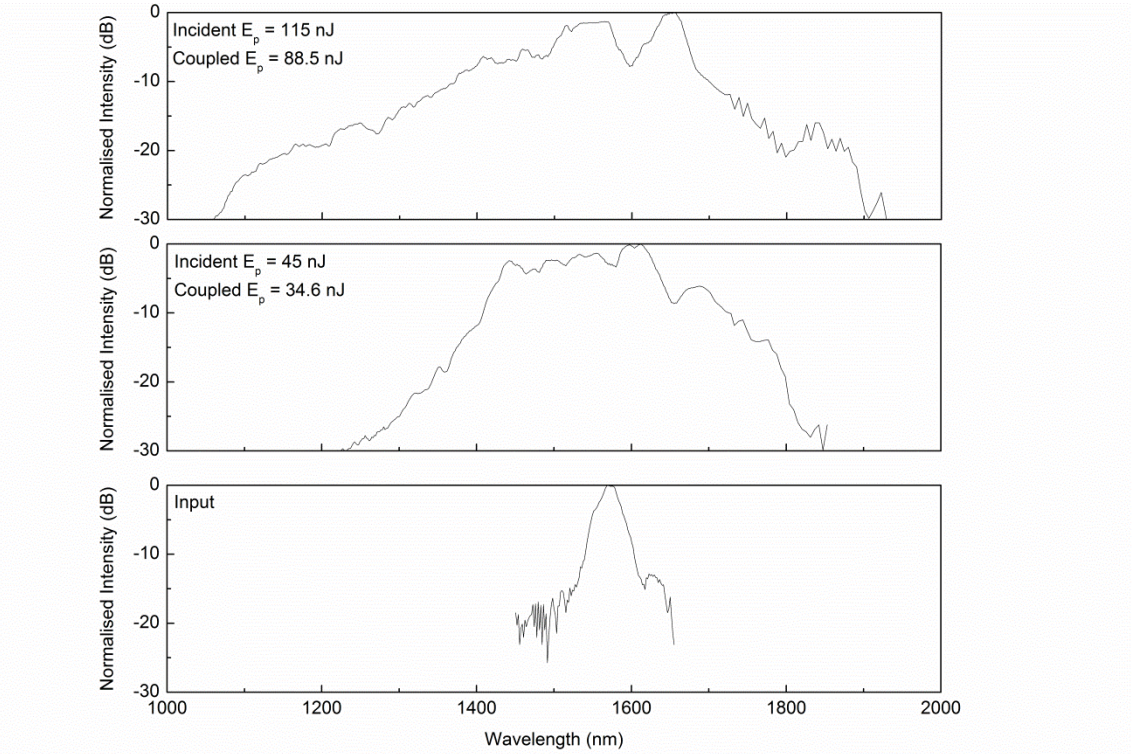

Figure 6.8: Evolution of spectrally broadened femtosecond pulses with input pulse energy.

Due to the pump wavelength lying well into the normal dispersion regime the primary spectral broadening mechanism is expected to be SPM. The shape of the output spectra in figure 6.8 confirm the dominance of SPM – intense peaks either side of the pump input wavelength. The red-shifting of the main spectral peak by 105 nm from 1550 to 1655 nm is evidence of stimulated Raman scattering.

6.5.2. Waveguide characterisation - 2485 nm

The Idler output of the OPA system was then used to observe the guiding characteristics further into the infrared. The wavelength of interest was 2485 nm as this was the longest wavelength the Idler output could be stably tuned to. At this wavelength the intrinsic losses in silica are significant - thus a chalcogenide glass based integrated optical devices have the advantage of increased material transmission. The near-field images of the guided modes were imaged using a FLIR SC700 camera connected to a PC. A software package (Altair) was used to capture and record images. 20× (0.24 NA) ZnSe

aspheric lenses (Innovation Photonics LFO-5-6-λ) are used to couple/image the 2485 nm radiation to/from the waveguide structures.

At a wavelength of 2485 nm, structures inscribed with pulse energies between 101 - 125 nJ were found to guide a single transverse mode. Figure 6.9 shows the facet image of a waveguide written with pulse energies of 113 nJ and a translation speed of 0.4 mm/s. The mode field diameter of the guided mode was calculated to be 19.05 µm in the x axis and 23.75 µm in the y axis.

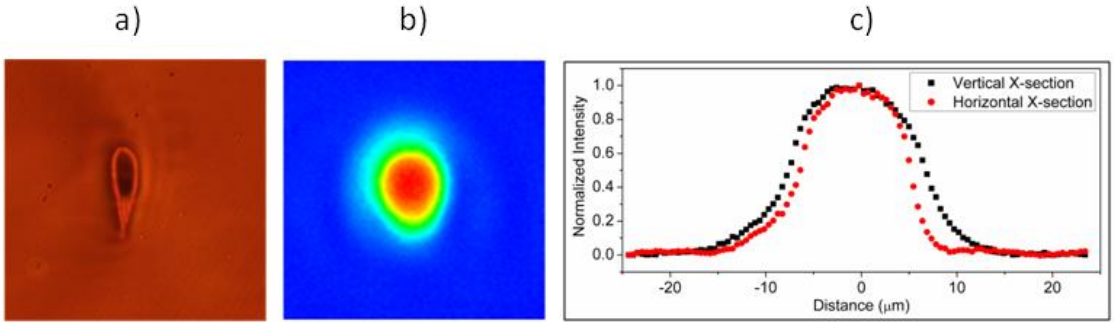

Figure 6.9: (a) Optical micrograph of waveguide facet, (b) corresponding 2485 nm mode image, (c) intensity line plots of guided mode.

In order to observe the nonlinear spectral broadening characteristics of this guiding structure for femtosecond pulses with a central wavelength of 2485 nm the experimental set-up described in figure 6.7 was changed to include a number of mid infrared diagnostic equipment. This was necessary due to the limited working ranges of the USB spectrometers. The OPA output was passed through an MgF_2 half-wave plate and a BaF_2 wire grid polarizer which were used for power and polarization control. A monochromator (Zolix Omni λ-300) used in conjunction with a PbSe detector and lock-in amplifier which replaced the USB spectrometers for measuring the spectral power distribution. The highly multimode patch-cord is also replaced with a calcium fluoride lens with a focal length of 5 mm which was placed at the entrance slit of the monochromator. Incident power measurements were made using a pyro-electric detector (Laser Probe Inc. RkP-575). This altered experimental arrangement is summarised in figure 6.10.

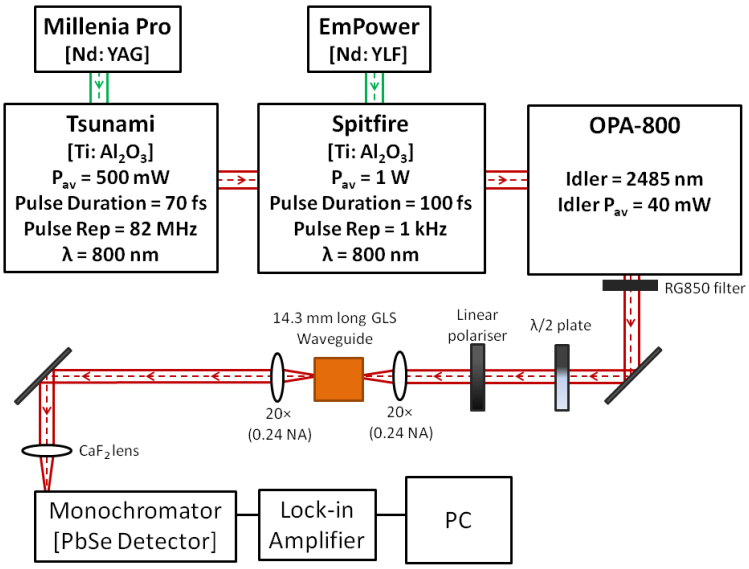

Figure 6.10: Experimental set-up for spectral broadening measurements for pump wavelengths of 2485 nm.

Figure 6.11 shows the transmitted spectrum of waveguide shown above in figure 6.9 when pulse energies of 72 and 130 nJ were incident onto the coupling lens. The input pump spectrum is also shown for comparison. The focusing spot diameter ($1/e^2$) of the input objective was measured to be 12.5 μm. Using equation (6.3) the minimum coupling loss from the objective to the waveguide was calculated to be 1.21 dB due to spatial mismatch. The aspheric lens was measured to have a throughput loss of 0.97 dB. After taking into account further losses due to Fresnel reflection at the waveguide facet meant that pulse energies of 65.8 nJ were coupled to the waveguide in comparison to the 130 nJ incident measurement. Like-wise 36.5 nJ coupled pulse energies were calculated for incident pulse energies of 72 nJ.

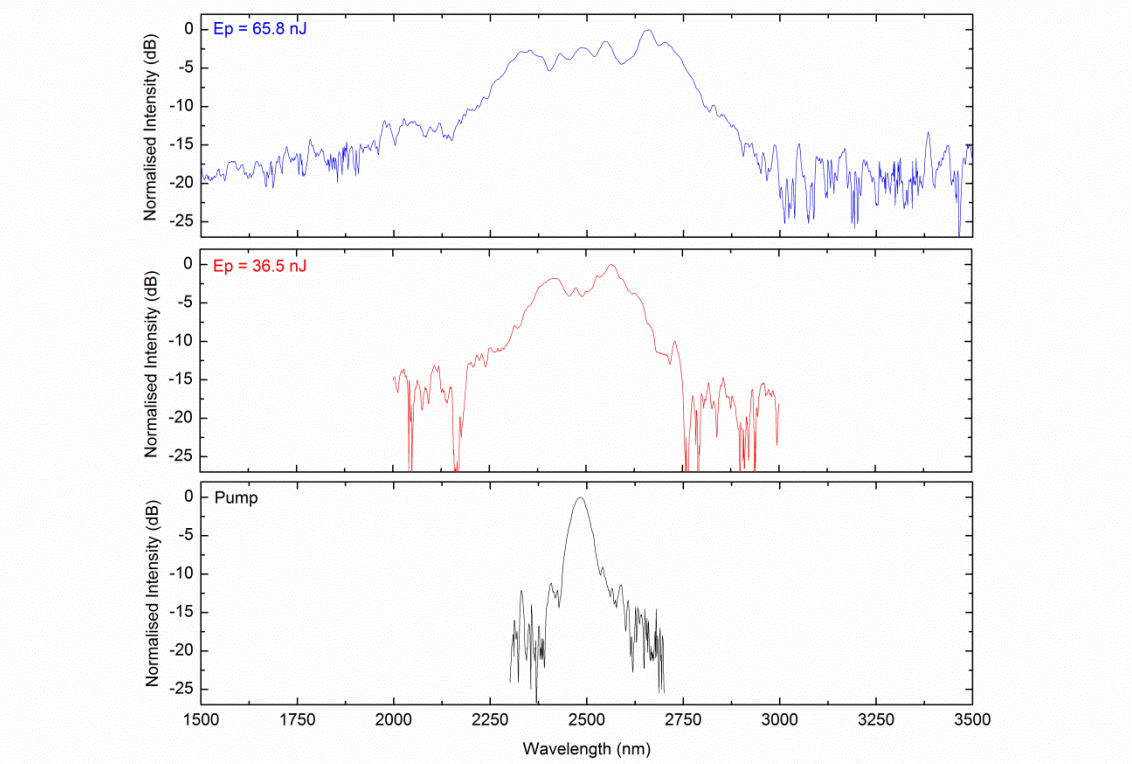

Figure 6.11: Graph showing normalized transmission spectra for coupled femtosecond pulse energies of 36.5 and 65.8 nJ. The pump input spectrum is shown for comparison.

The pump wavelength is still firmly in the normal dispersion regime for GLS and the continuum evolution is similar to that observed in figure 6.8 at 1550 nm – with the characteristic build-up of self phase modulation. Figures 4(b) and 4(c) show the individual broadened output spectra plotted with a linear scale with arrows indicating these self-phase modulation peaks. At the -15 dB points the broadened spectrum spanned 899 nm from 2002 nm to 2901 nm. The peak of the continuum with the most spectral power is red-shifted by 176 nm with respect to the input pulse wavelength and is again evidence of stimulated Raman scattering.

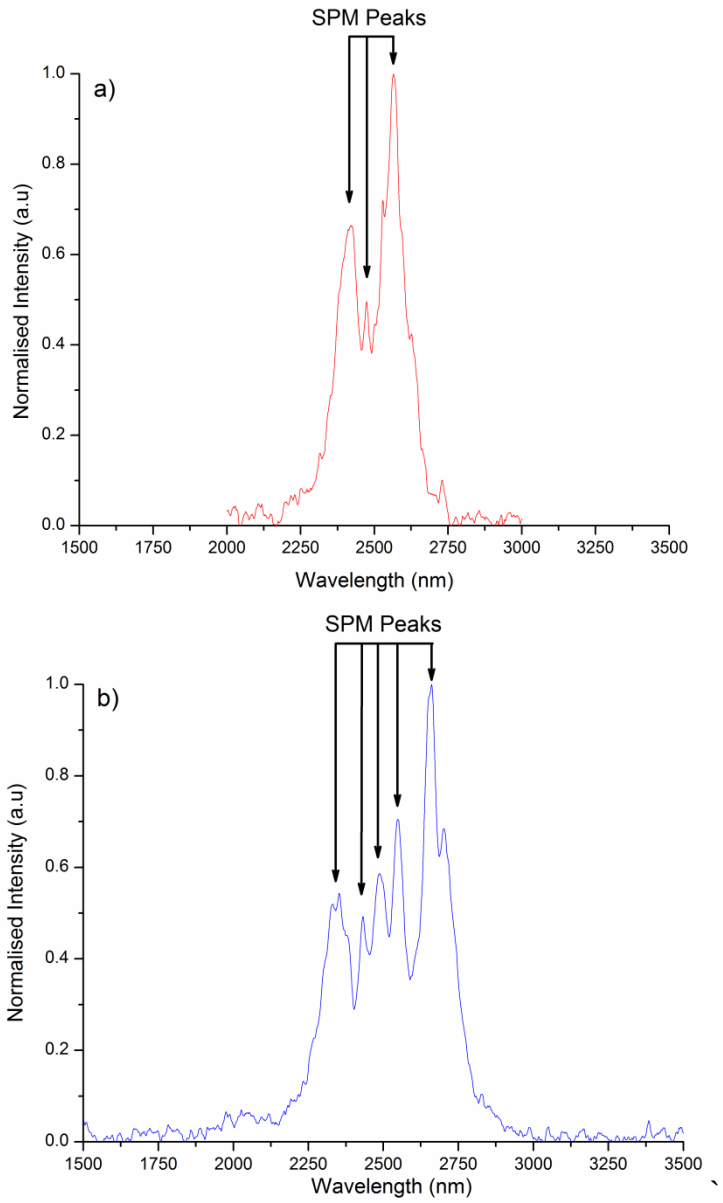

Figure 6.12: Graphs showing waveguide output spectra with highlighted SPM peaks for coupled pulse energies of (a) 36.5 nJ and (b) 65.8 nJ

From the number of SPM peaks in the broadened output spectra it is possible to calculate the maximum phase change occurring within the sample. This phase change then determines the nonlinear refractive index the radiation experiences upon propagation, and thus the nonlinear refractive index of the modified region. Using equation (6.4), where m is the number of SPM peaks in a given spectra, the maximum nonlinear phase change undergone by the guided light can be calculated [119].

$$\emptyset \max = m - \frac{1}{2} \qquad \textit{Eq. (6.4)}$$

From figure 6.12 (a) we can see there are 3 distinguishable peaks; therefore this yields a maximum nonlinear phase change of 2.5π for coupled pulse energies of 36.5 nJ. Similarly coupled pulse energies of 65.8 nJ yielded a maximum nonlinear phase change of 4.5π.

This maximum π nonlinear phase change can then be used in equation (2.27) and subsequently re-arranged to obtain an upper estimate on the nonlinear refractive index of the waveguide, n_2, for a given waveguide length, L, for a set irradiance, I.

$$n_2 = \frac{2\pi LI}{\lambda \Delta \emptyset_{nl}} \qquad \textit{Eq. (6.5)}$$

where the irradiance is calculated using equation (6.6), where E_p is the pulse energy, t_p is the pulse duration and A_{eff} is the effective mode area:

$$I = \frac{E_p}{A_{eff} t_p} \qquad \textit{Eq. (6.6)}$$

The maximum n_2 of the waveguide at 2485 nm is calculated to be 1.43×10^{-19} m^2W^{-1}. In order to compare this with unmodified GLS a z-scan experiment is conducted at a wavelength of 2485 nm on a 1 mm thick piece of GLS. The focusing lens was a 20 cm focal length calcium fluoride lens and two PbSe detectors were used to measure the reference and closed aperture data. Apart from these optics/diagnostic equipment substitutions the experimental arrangement was the same as that outlined in section 3.3 Figure 6.13 shows a closed aperture z-scan trace with pulse energies of 500 nJ and an aperture transmission of 50%. The theoretical fit corresponds to a nonlinear refractive index of 7.8 ± 0.9 x 10^{-19} m^2W^{-1}at 2485 nm.

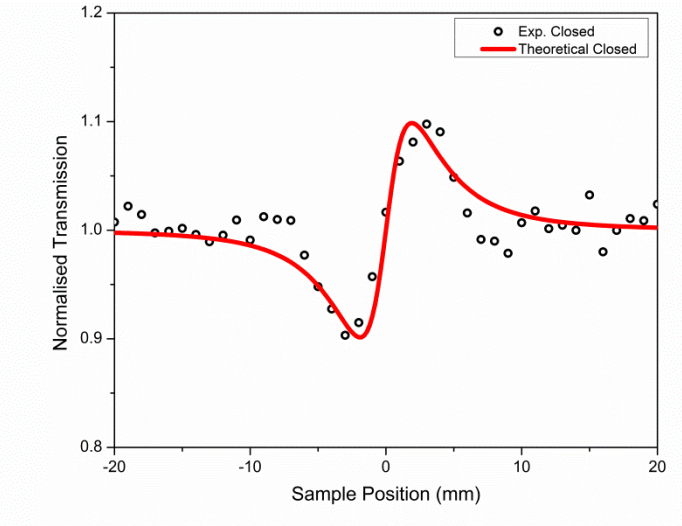

Figure 6.13: Closed aperture Z-scan trace conducted on 1mm thick GLS sample with pulse energies of 500 nJ and an aperture transmission of 50%

The value obtained for the nonlinear refractive index from the z-scan of the un-modified bulk GLS is approximately 5 times higher than that calculated by the self phase modulation results from the waveguide transmission experiments. This significant difference highlights how the re-structuring of the material can impact upon the material properties. It may be the case that the decrease in the nonlinear refractive index is heightened for structures inscribed with high pulse energies due to significant photo-darkening regions and large modification areas.

6.5.3. Waveguide characterisation - 3850 nm

The guiding characteristics of the inscribed structures were then investigated at a wavelength of 3850 nm – close to the material zero dispersion wavelength of un-modified GLS. This wavelength of interest was accessed by focusing the signal and idler outputs of the OPA onto a difference frequency crystal. To obtain the required 3850 nm difference frequency mixing output the signal and idler were tuned to wavelengths of 1327 and 2018 nm respectively. A long pass 2500 nm filter was placed at the output of the OPA to block the residual signal and idler radiation.

Structures inscribed with pulse energies of 140 nJ to 172 nJ were found to guide a single transverse mode at a wavelength of 3850 nm. Figure 6.14 shows one such

structure along with the corresponding near field mode profile and x, y plane cross-sections. This was inscribed with a pulse energy of 140 nJ and a translation speed of 0.6 mm/s. The $1/e^2$ diameter of this guided mode was calculated to be 19.34 µm in the x and 27.22 µm diameter cross-section in y.

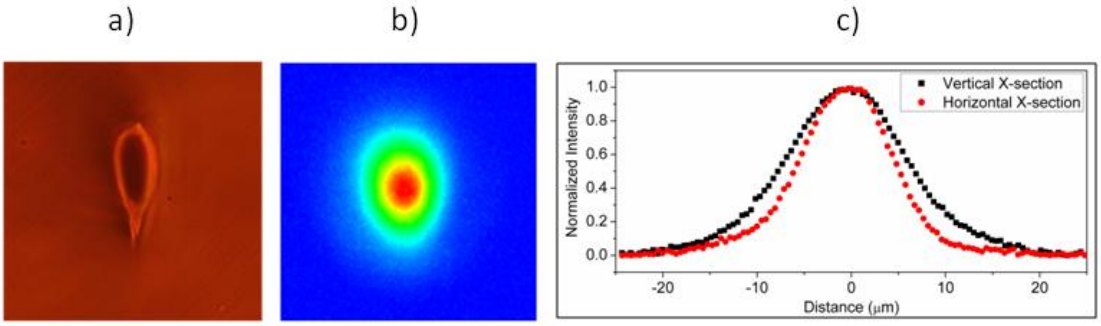

Figure 6.14: (a) Optical micrograph of waveguide facet, (b) corresponding 3850 nm mode image, (c) intensity line plots of guided mode.

The average power of the OPA output was then increased and the spectral power distribution from the waveguide output was recorded. Figure 6.15 shows the span of continuum when 115 nJ pulses are incident onto the aspheric lens. The input pulse spectrum is also shown for comparison. At 3850 nm the aspheric lens was measured to give an input coupling spot size of 14.5 µm, which would yield a 1.03 dB coupling loss to this waveguide structure. Taking into account the loss due to the spatial mis-match between the waveguide mode and the focusing spot, the Fresnel reflection loss and the loss incurred by the aspheric lens gave a maximum coupled pulse energy for propagation through the waveguide of 57 nJ (from 115 nJ incident). At the -15 dB points the continuum spanned 1588 nm from 2911 nm to 4499 nm from a 14.3 mm long waveguide. Although the pump wavelength lies close to the zero-dispersion wavelength of GLS the broadening still has the characteristics of self-phase modulation.

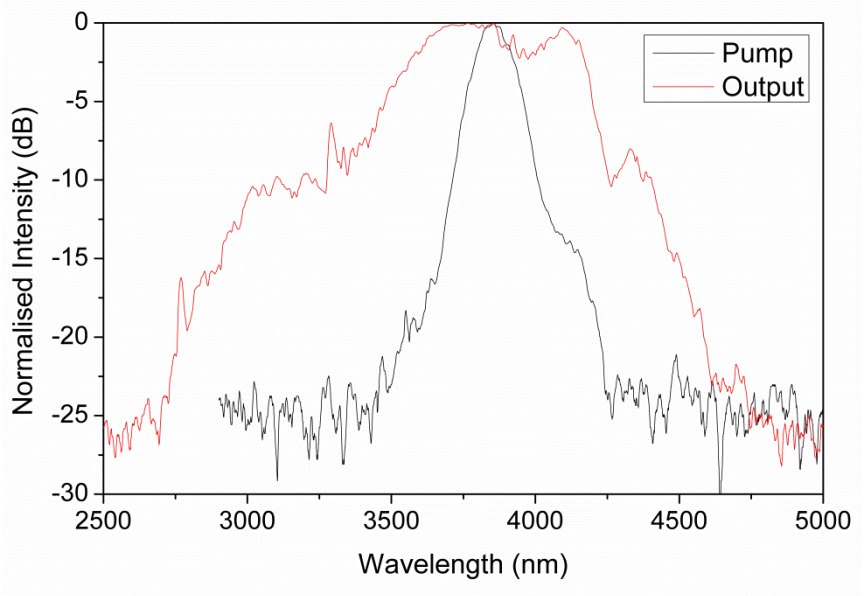

Figure 6.15: Graph showing normalized transmission spectra for coupled femtosecond pulse energies of 57 nJ from incident pulse energies of 115 nJ. The pump input spectrum is shown for comparison.

6.6. Discussion

Nonlinear spectral broadening was observed in three separate structures at three different pump wavelengths throughout the near and mid infrared. The effect of moving closer to the ZDW wavelength was found to improve the continuum generation with increased spectral broadening observed for lower coupled pulse energies. While the mode structures guided single transverse modes, they were asymmetric and were encompassed by a large modified structure. The large modified structure limits the potential for implementation in complex and compact devices due to the larger size and non-uniform refractive index change, as observed by the photo-darkened region in the facet images.

To acquire a more uniform modified region and symmetric mode profile the multi-scan inscription technique [120] was implemented. This would allow for a higher degree of flexibility over the energy deposition for inscribing structures.

6.7. ULI multiscan technique

The multiscan technique was implemented to fabricate a smoother refractive index change and a more symmetrical guided mode in order to lower the coupling and scattering losses of the waveguide structures. The multi-scan inscription technique uses multiple single-scan modified regions with a small horizontal offset to build up a desired cross-section. This process is outlined in figure 6.16. The horizontal offset adds another variable fabrication parameter Δx.

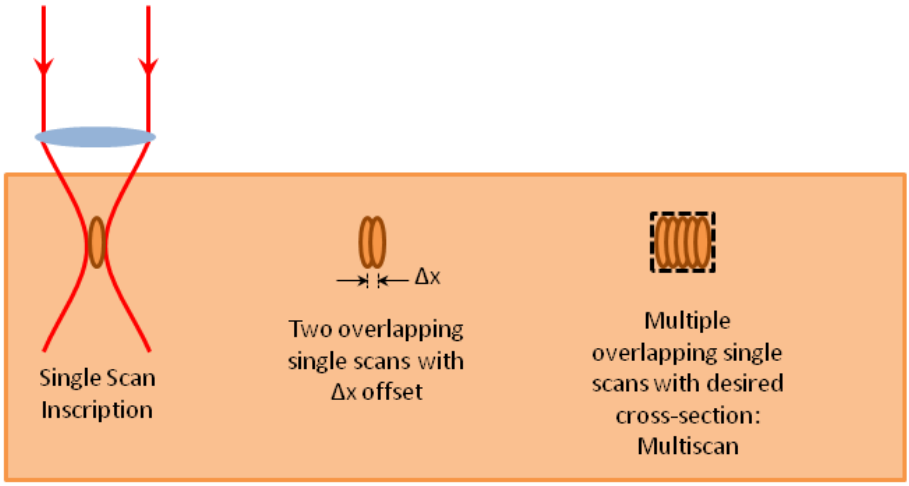

Figure 6.16: Schematic outlining the multiscan inscription process.

A different fabrication laser (IMRA µJewel) was used as the inscription laser for multiscan fabrication. This laser system is comparable to the Fianium, the laser used previously, having a similar central wavelength of emission of 1060 nm, with the added advantage of having a variable repetition rate and pulse duration. The repetition rate can be varied from 100 kHz - 5 MHz and the external pulse compressor allows for the pulse duration to be varied from 400 fs to 2 ps.

Evaluating the inscription parameters previously used, the most applicable structures for use with the multiscan technique were written with pulse energies of less than 91.5 nJ, and thus an average power of less than 45 mW. These structures exhibited the narrowest cross-section. However in order to ensure a large enough index contrast for guiding at the wavelength of interest, 4260 nm, a broad range of fabrication pulse energies were investigated. The pulse duration of the laser was set to 420 fs and with a repetition rate

of 500 kHz. The pulses were focused 100 µm below the top surface by a 0.6 NA aspheric lens. Sample translation speed of 0.2, 0.4 and 0.6 mm/s were used and the incident pulse energies were varied from 194 – 72 nJ in decreasing increments of 6%. The polarisation was set to circular. The horizontal offset, Δx, was set to 0.2 µm for multi-scan inscription

6.8. Multi-scan waveguide morphology

Like the previous inscription run two regimes were observed, one with smooth uniform refractive index changes and one were thermal accumulation effects are apparent. Figure 6.17 shows the waveguide facet structure for three different inscription pulse energies each with a 50×50 µm field of view.

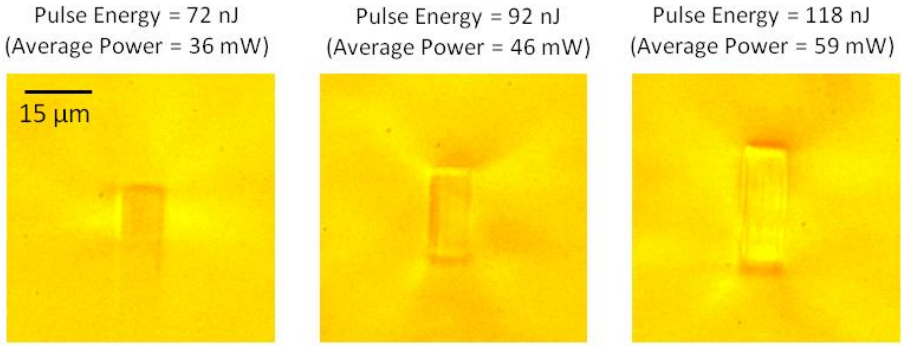

Figure 6.17: Microscope images of waveguide structures inscribed via the multiscan inscription technique.

The inscribed structures in figure 6.17 show a more uniform and symmetrical cross section than those inscribed via the single scan inscription process. As the inscription pulse energy is increased the modified region sizes lengthen and the index modification becomes less uniform as a vertical grating feature is observed in the 118 nJ inscription case. The increase of thermal accumulation effects are highlighted in figure 6.18. Each facet image has a 100×50 µm field of view.

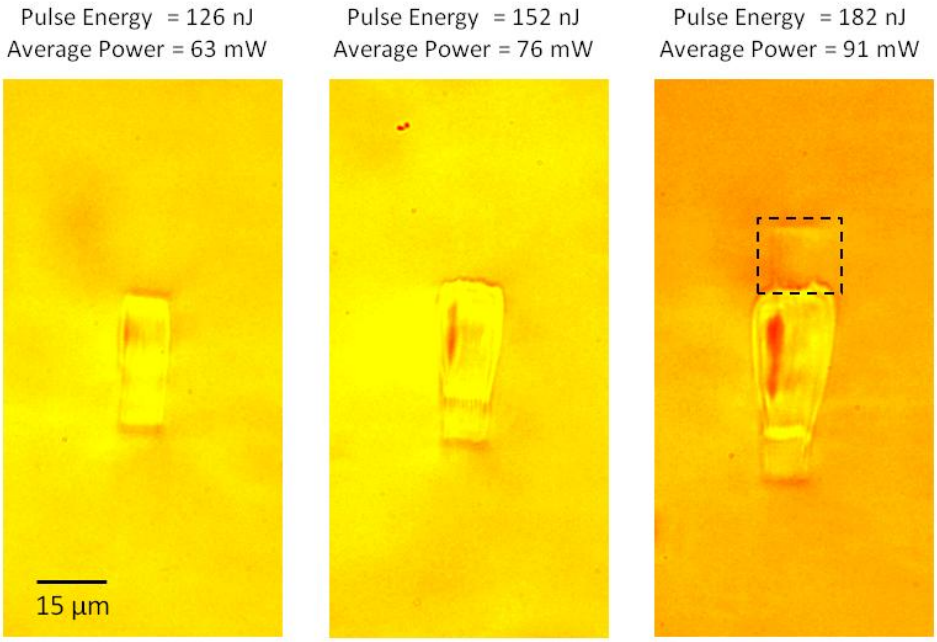

Figure 6.18: Microscope images showing thermal accumulation effects present in waveguide structures inscribed with high pulse energies via the multiscan inscription technique. Highlighted area indicates an additional modified region.

Here the evolution of the teardrop structure can clearly be seen as the pulse energy is increased. Interestingly for the highest inscription pulse energies; in addition to a significant photo-darkened region there are small areas approximately 14×9 µm in size situated just above the principal modified structure. This modified area is most likely due to reflections from the plasma filaments having enough energy to themselves induce a refractive index change in the bulk GLS.

The inscribed structures were then examined to see if a high enough index contrast had been achieved to allow for guiding at 4260 nm. The wavelength of 4260 nm was selected as a pump wavelength due to it lying approximately 260nm into the anomalous material dispersion regime of GLS. The effect pumping in the anomalous dispersion regime was expected to allow solitary wave propagation to occur in a single-mode waveguide and thus enhance the spectral broadening.

6.9. Waveguide characterisation

Due to the strong absorption of 4260 nm wavelength radiation in the atmosphere due to the presence of carbon dioxide, it was necessary to encase the difference frequency set-up outlined above in section 6.5.3 and the waveguide coupling experiment in a positive pressure chamber. A continuous flow of oxygen free Nitrogen was pumped into the chamber in order to displace the carbon dioxide. A schematic of the opened chamber experimental set-up is shown in figure 6.19.

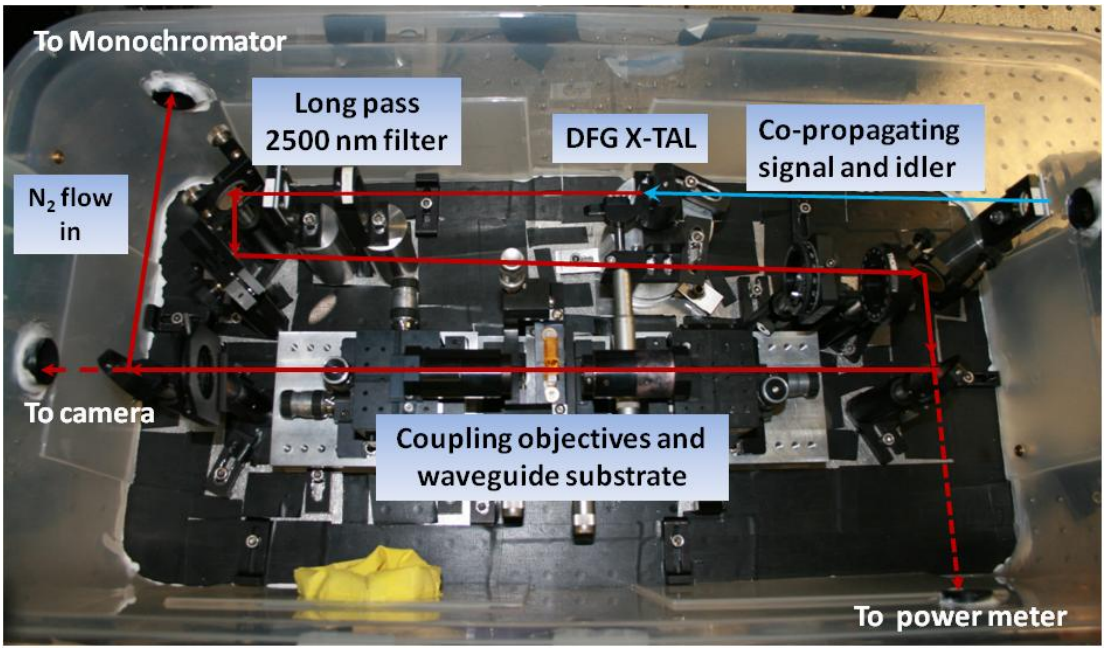

Figure 6.19: DFG and waveguide coupling experimental set-up.

The co-propagating signal and idler beams are directed through a 1 mm thick calcium fluoride window before being focused onto the $AgGaS_2$ difference frequency crystal. The residual signal and idler power is then cut-off by a long pass 2500 nm filter. The difference frequency output is then collimated and passed through a MgF_2 half-wave plate and a BaF_2 wire grid polariser which allowed for power and polarization control. Incident power measurements are made by the pyro-electric detector which was accessed by lowering a flip mirror, the beam is then passed through a calcium fluoride window and onto the detector. Two 20 mm focal length calcium fluoride lenses were used to couple and then collect the light from the test waveguides. These replaced the ZnSe aspheric lenses used in the previous mid infrared spectral broadening

measurements. The calcium fluoride lenses exhibited a much lower throughput loss and were better mode matched to that of the inscribed structures. Both the calcium fluoride lenses were mounted on separate x, y, z translation stages. The waveguide substrate was mounted on the four axis translation stage. By changing the position of a second flip mirror the waveguide output could either be directed onto a camera (FLIR SC7000) in order to record the guided mode profiles, or onto the monochromator (Zolix Omni λ-300). Both the monochromator and the camera lay outside the positive pressure chamber. The monochromator was again used in conjunction with a PbSe detector and a lock-in amplifier.

The multiscan structures inscribed with pulse energies between 139 – 105 nJ were found to guide a single transverse mode at 4260 nm. Figure 6.20 shows the facet image of an inscribed waveguide and the corresponding mode profile at 4260 nm. The waveguide was fabricated with a pulse energy of 118nJ and a sample translation speed of 0.4 mm/s. The field of view for both the facet image and mode profile is 100 μm. The guided mode exhibits a greater degree of circular symmetry than waveguides inscribed previously in GLS using the single-scan writing process. The $1/e^2$ mode field diameter was calculated to be 45.5 μm in x and 44.6 μm in y. This mode size is large in comparison to the size of the modified region, thus the index contrast between the modified area and that of the bulk is low due to the largely evanescent nature of the guided mode.

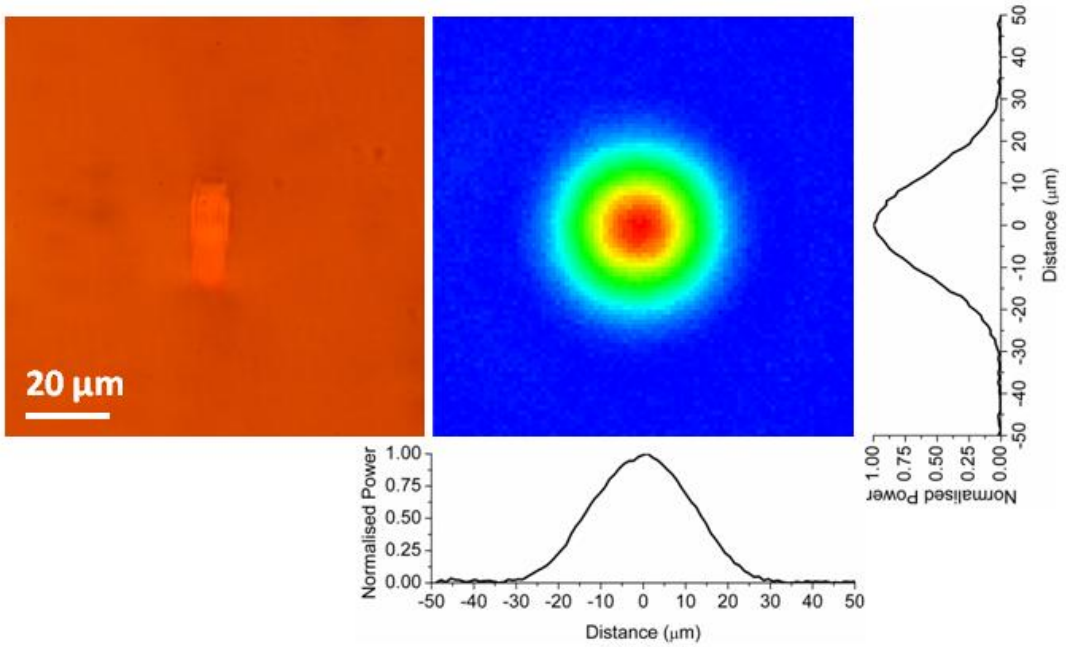

Figure 6.20: Microscope waveguide facet image and corresponding 4260 nm waveguide mode profile with x and y –plane cross sections.

6.10. Spectral broadening investigation

The nonlinear guiding properties of the waveguide featured above in figure 6.20 were then investigated by increasing the incident pulse energy to 410 nJ and observing the spectral power distribution of the output. Figure 6.21 shows the recorded output spectra. The input polarisation was set to parallel to the optical table, along x-axis, with respect to the waveguide facet. The theoretical pump spectrum is shown for comparison. Both traces are normalised to their respective peaks. The simulated input spectrum was calculated by fitting a Gaussian curve to the pump spectrum data as the monochromator could not record CO_2 absorption free spectra. This is highlighted in figure 6.22.

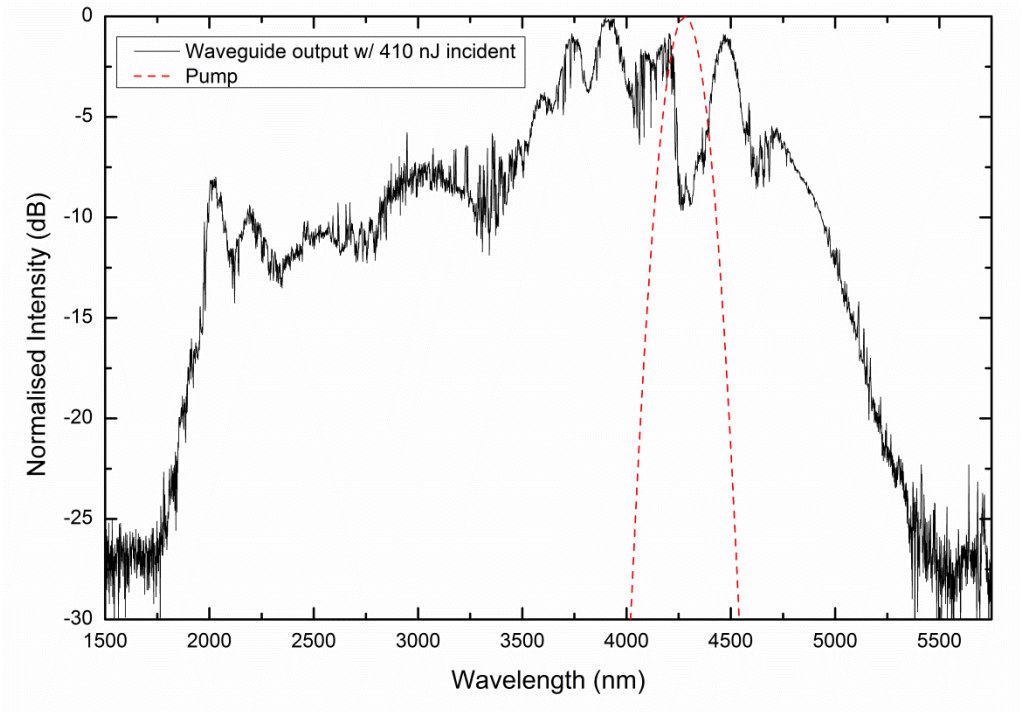

Figure 6.21: Spectrally broadened waveguide output with input pulse energies of 410 nJ with a central wavelength of 4260 nm

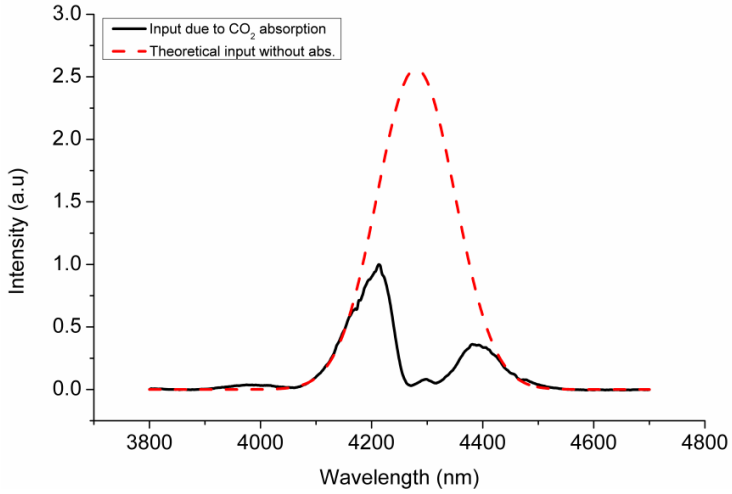

Figure 6.22 Simulated absorption free Gaussian input spectrum fitted to recorded input spectrum

At the -15 dB points the continuum spanned from 1850-5100 nm. However the responsivity of the PbSe detector drops rapidly at wavelengths greater than 4500 nm and has less than a 5% relative response at wavelengths greater than 5000 nm. However power has been redistributed away from the 4.2-4.4 µm absorption band to other wavelengths throughout the entire MWIR region (3-5 µm). From figure 6.20 the carbon dioxide absorption effects can still be observed. This is due to the waveguide output

having to pass through a small amount of the atmosphere before being coupled to the monochromator. Three repeat waveguides are then fabricated in three separate substrates in order to demonstrate the repeatability of the inscription process. The differences in the spectrally broadened outputs for waveguides inscribed with pulse energies of 118 nJ and a sample translation speed of 0.4 mm/s were then investigated. Each of the substrates were aligned side by-side on the four-axis translation stage. Coupling from one substrate to the next was performed by simply moving along x. To ensure optimised coupling to each waveguide this process was conducted in an un-purged environment (i.e. with the chamber lid off). After coupling optimisation the waveguide experimental chamber was then sealed and oxygen free nitrogen was flown through the chamber. Figure 6.23 shows the comparison for the spectrally broadened outputs of the four inscribed waveguides with incident pulse energies of 400 nJ.

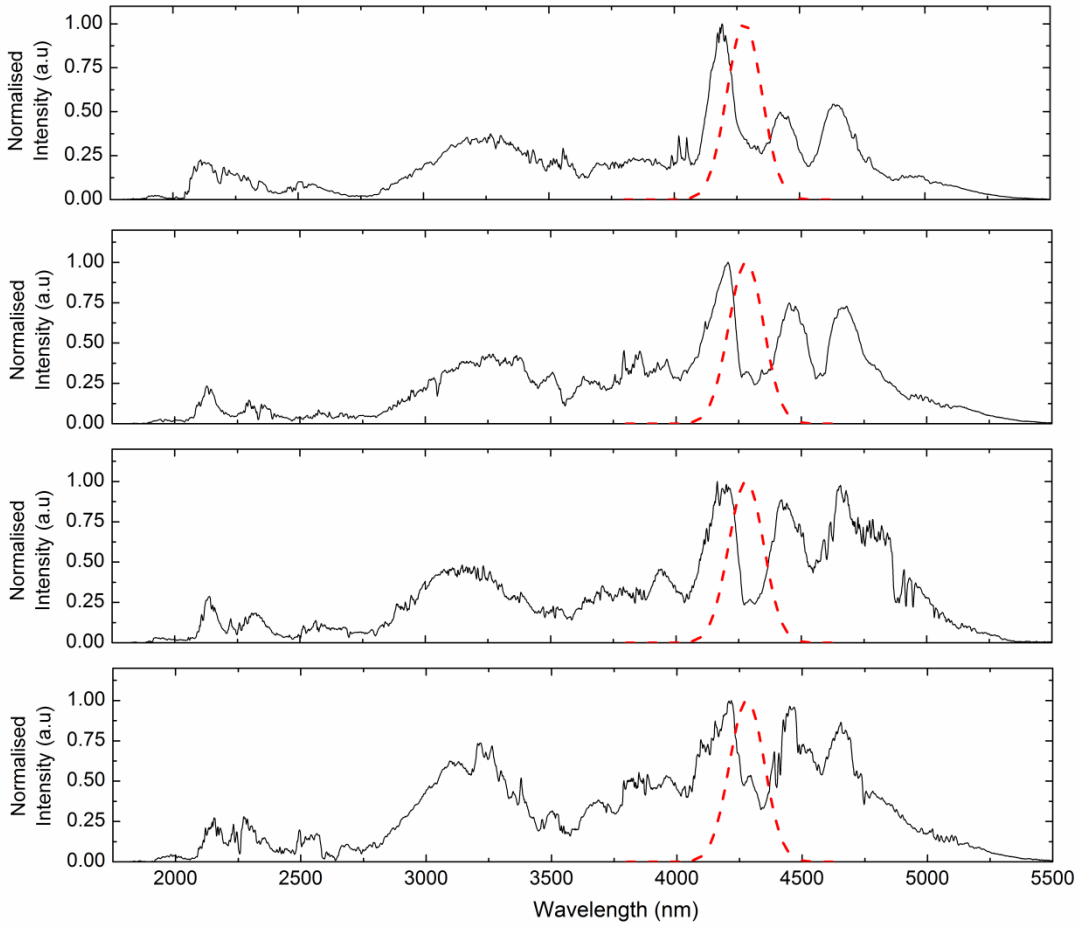

Figure 6.23: Comparison of spectral broadening for 4 separate waveguide structures inscribed with identical parameters. The incident pulse energy was 400 nJ.

Differences between the spectra may lie in drift of laser power over time. It takes the monochromator 45 minutes to scan across the wavelength range (1700 - 6000 nm), small atmospheric changes over this time can also lead to differences in recorded spectra. However the breadth of the continuum remains unchanged.

6.11. Discussion

The work contained in this chapter has shown that ULI can be utilised to fabricate, in a single fabrication step, structures that can be tailored to guide throughout the near and mid infrared. The fabrication times of MWIR guiding structures are much shorter than those required while using thin film deposition techniques. Additionally, fabrication times for structures that either guide a single transverse mode in either the near or mid IR are comparable due to the dominant fabrication parameter being inscription pulse energy. The generation of a supercontinuum that fills the MWIR atmospheric transmission window has wide potential for fabrication of optical sensors and military countermeasure devices. The multi-scan inscription technique was implemented to fabricate a more confined, and uniform, modified area by reducing the effects of thermal accumulation. This cleaner refractive index profile should allow increased evanescent field interaction between waveguides and thus allow for the fabrication of complex optical devices, such as directional couplers or evanescent field sensors. These devices can be fabricated in a single fabrication step and also used for devices designed in three dimensions thus giving ULI an advantage over technologies such as MIMIC which require mould fabrication and are limited to 2D device fabrication.

In the literature it can be seen that ULI has been demonstrated to be a useful tool for the fabrication of a diverse range of optical devices including pulsed and cw laser sources [121-125] and nonlinear frequency doubling [126] conversion chips. It can be seen that in the future ULI can be used to transfer the difference frequency stage used in this chapter to a waveguide in lithium niobate. An integrated mid IR supercontinuum chip can then be envisioned by coupling to the highly nonlinear waveguide in GLS described in this chapter.

Chapter 7. Conclusions and further work

7.1. Conclusions

The work in this thesis has focused on nonlinear optical processes in the near and mid infrared. Chapters 3 and 5 focused on investigations into the fundamental nonlinear absorption and refraction effects in bulk glasses and nanostructured materials. Chapters 4 and 6 concentrated on how nonlinear waveguides, namely how a materials' nonlinearity could be enhanced by increasing the interaction length and minimising dispersion.

In chapter 3 the z-scan experimental set-up was used to measure the nonlinear refractive index and nonlinear absorption coefficients of a number of chalcogenide and tellurite glass systems. The chalcogenide samples provided by Nottingham University were compositions of As-S-Se and As-Se-Te. Of the As-S-Se system the highest switching figures of merit were measured in $As_{40}Se_{60}$ and $As_{40}S_{60}$. The presence of both sulphur and selenium in the same system was found to reduce the nonlinear switching figure of merit. This effect was found to be greatest for the $As_{40}S_{(60-x)}Se_{(x)}$ and $As_{30}Se_{(70-x)}Te_{(x)}$ compositions. In the As-Se-Te chalcogenide system increasing the molar concentration of telerium shifted the short wavelength absorption edge to longer wavelengths, up to the investigation wavelength. Therefore these samples exhibited the highest nonlinear absorption coefficient and thus the lowest nonlinear switching figure of merit. The short wavelength absorption being situated at near infrared wavelengths, specifically greater than 1064 nm, also meant that they were incompatible with the nonlinear optics groups ULI Yb:fibre laser system. Of the glasses investigated in this study the chalcogenide glass GLS was found to have the highest nonlinear optical switching figure of merit. This high FOM in addition to being an arsenic free chalcogenide glass and the compatibility with the ytterbium fibre laser used for ULI in the nonlinear optics group meant that it was as the substrate material for fabrication of a nonlinear, mid infrared guiding waveguide.

Chapter 4 presented work on identifying how the different nonlinear spectral broadening mechanisms shape the supercontinuum generation in highly nonlinear silica photonic crystal fibres. The fibres were provided by CGCRI. This investigation focused on the effect of fibre dispersion and how it affects the threshold of the different spectral broadening mechanisms that lead to supercontinuum generation. The results of this experimental study enabled collaborators at CGCRI to further develop their theoretical model for supercontinuum generation in PCFs. It was found that maximising the contribution of solitary wave mechanics, such as soliton fission and soliton self-frequency shift, allowed for increased spectral broadening of femtosecond pulses in the photonic crystal fibres. Additionally by coupling the radiation to one of the principal axis of a highly birefringent PCF further enhanced supercontinuum generation. This was due to the polarisation maintaining elliptical core confining the radiation in one fibre axis and experiencing one dispersion profile. Launching the radiation into the fibre off-axis was found to decrease the spectral broadening efficiency as the coupled power was split between the two principal axis and thus divided into the two dispersion profiles. A study into supercontinuum generation and evanescent field coupling was then conducted in a 120 core silica fibre. This study found that interaction between the solitary wave and shorter wavelength radiation could be reduced.

In chapter 5 the effect of saturable absorption in two nanostructured materials was observed. Z-scan experiments demonstrated that by aligning silver spheroid nanoparticles on a high purity silica host glass allowed for a highly anisotropic saturable absorption dependence. Saturable absorption investigations in single walled carbon nanotubes embedded in a PMMA film exhibited no such polarisation dependence due to the unaligned nature of their deposition. Competing multiphoton and saturable absorption processes were found to occur in the SWCNT at high irradiances. The field irradiance where the effects of multi-photon absorption began to outweigh that of saturable absorption was identified as 9.5×10^{13} W/m^2. This effect manifested as a dip in the saturable absorption z-scan trace, meaning that the location of greatest transmission lay outside of the focal plane. The depth and width about the focal plane of this nonlinear absorption dip subsequently increased for increasing irradiance z-scans. This dip was not observed in the blank PMMA film. The recovery of the saturable absorption

after translation through the focus also confirmed that this dip was not in part due to ablation of either the SWNCTs or the PMMA film.

Chapter 6 presented waveguide fabrication and spectral broadening characterisation of a gallium lanthanum sulphide glass waveguide. The waveguide was fabricated via ultrafast laser inscription. The waveguiding characteristics were strongly dependent on the fabrication pulse energy. Through appropriate selection of inscription pulse energy and sample translation speed yielded a modified structure which exhibited a small positive refractive index change but with minimal thermal accumulation and diffusion shaping. This modified region was then built up through the multiscan inscription technique in order to fabricate a structure to enable guiding mid infrared radiation in a single transverse mode. Upon coupling femtosecond pulses with a central wavelength of 4260 nm into such a structure a supercontinuum spanning over 3000 nm across the mid wavelength infrared spectral region.

7.2. Further work

The study into the nonlinear optical properties of chalcogenide glasses provided by Nottingham University was conducted at 1550 nm and assessed in regards to telecoms switching applications. As mentioned earlier the dominant nonlinear optical process in the $As_{30}Se_{(70-x)}Te_{(x)}$ chalcogenide system was nonlinear absorption, however they also exhibited a large nonlinear refractive index. A shift of focus of this collaboration towards mid infrared operating integrated devices via ULI could see higher effective nonlinearity waveguide fabrication. To negate the effect of single photon absorption would require a longer wavelength of emission inscription laser, such as a modelocked thulium fibre laser emitting at 1900 nm. The development of a modelocked thulium fibre laser as waveguide inscription source could be undertaken in collaboration with CGCRI who have the facilities and expertise to fabricate rare-earth doped fibres. An additional concern for this potential project are the additional safety measures that would need to incorporated into the inscription set up due to working with arsenic based chalcogenide glasses.

The highly evanescent guiding nature of the GLS waveguides fabricated via multiscan ULI could allow for an embedded sensor device that also takes advantage of the inherent 3D writing capabilities offered by ULI. Such a device could consist of a single mode waveguide written inside a highly nonlinear glass that generates a broad supercontinuum before splitting into two waveguides. One of which is raised close to the substrate surface in order for the evanescent field to interact with the surface. Fundamental molecular absorption lines that lie inside the bandwidth of the supercontinuum bandwidth will therefore manifest as a dip in the supercontinuum spectrum which can be monitored by comparing to the second embedded 'reference' channel. The fabrication of a compact mid infrared nonlinear optical device could be realised by incorporating both the difference mixing stage and supercontinuum stage onto one ULI fabricated chip. Whereby the mid infrared difference frequency pump source is generated in a ULI waveguide in lithium niobate. This can then be bonded or laser wielded onto the mid infrared continuum waveguide fabricated from GLS.

Additionally the ultrafast laser inscription technique is an ideal candidate for the basis of tailoring evanescent field interaction in the supercontinuum process – such as soliton radiation isolation. Prototype fabrication can be optimised for a wide range of wavelengths and can be used to modify a multitude of materials. Furthermore ULI can be used to vary waveguide separation and properties along the waveguide length or to recombine the radiation into a single waveguide and therefore spatial-temporal tailoring of supercontinuum generation. Ideally this recombination of supercontinuum radiation into a single core would allow for wavemixing between different wavelength components that would otherwise not temporally overlap inside a single core. As seen with the supercontinuum investigation in the CGCRI photonic crystal fibres, the interaction between the solitary wave and other co-propagating wavelength components greatly improves the generated supercontinuum. Therefore in order to optimise this spectral broadening the recombination would spatially and temporally overlap the soliton with the numerous other wavelengths generated through the other nonlinear processes multiple times. However the large normal dispersion at near infrared wavelengths displayed by chalcogenide glasses combined with the low contribution of waveguide dispersion from ULI waveguides means that the zero dispersion wavelength of a ULI chalcogenide waveguide could not be shifted far enough into the near infrared

to allow for solitary wave propagation to occur. At near infrared wavelengths it would be less challenging to exploit this effect in non silica based glasses, such as ZBLAN or calcium fluoride due to the increased infrared transmission ranges exhibited by these glasses.

References

1 J. F. Reintjes, "Chapter 1: Introduction," in *Nonlinear optical parametric processes in liquids and gases*, (Academic Press, 1984).

2 P. A. Franken, A. E. Hill, C. W. Peters, and G. Weinreich, "Generation of optical harmonics," Phys. Rev. Letters **7**, 118-119 (1961).

3 K.Zhao, Q. Zhang, M. Chini, Y. Wu, X. Wang, and Z. Chang, "Tailoring a 67 attosecond pulse through advantageous phase-mismatch," Opt. Letters **37**, 3891-3893 (2012).

4 M. Uiberacker, T. Uphues, M. Schultze, A. J. Verhoef, V. Yakovlev, M. F. Kling, J. Rauschenberger, N. M. Kabachnik, H. Schröder, M. Lezius, K. L. Kompa, H.-G. Muller, M. J. J. Vrakking, S. Hendel, U. Kleineberg, U. Heinzmann, M. Drescher and F. Krausz, "Attosecond real-time observation of electron tunnelling in atoms," Nature **446**, 627-632 (2007).

5 D. Huang, E. A. Swanson, C. P. Lin, J. S. Schuman, W. G. Stinson, W. Chang, M. R. Hee, T. Flotte, K. Gregory, C. A. Puliafito and J. G. Fujimoto, "Optical coherence tomography," Science **254**, 1178-1181 (1991).

6 J. F. De Boer, T. E. Milner, M. J. C. Van Gemert, and J. S. Nelson, "Two-dimensional birefringence imaging in biological tissue by polarization-sensitive optical coherence tomography," Opt. Letters **22**, 934-936 (1997).

7 D. L. Budenz, M-J. Fredette, W. J. Feuer, D. R. Anderson, "Reproducibility of peripapillary retinal nerve fiber thickness measurements with stratus OCT in Glaucomatous eyes," Ophthalmology **115**, 661-666 (2008).

8 N. N. Lal, B. F. Soares, J. K. Sinha, F. Huang, S. Mahajan, P. N. Bartlett, N.C. Greenham, and J.J. Baumburg, "Enhancing solar cells with localized plasmons in nanovoids," Opt. Express **19**, 11256 - 11263 (2011).

9 T. Nakasyotani, H. Toda, T. Kuri, and K. Kitayama, "Wavelength-division-multiplexed millimetre-waveband radio-on-fiber system using a supercontinuum source," J. Lightw. Tehnol. **24**, 404-410 (2006).

10 R. R. Alfano and S. L. Shapiro, "Emission in the region 4000 to 7000 Å via four-photon coupling in glass," Phys. Rev. Letters **24**, 584-587 (1970).

11 J. I. Gersten, R. R. Alfano and M. Belic, "Combined stimulated scattering and continuum self-phase modulations," Phys. Rev. A **21**, 1222-1224 (1980).

12 D. E. Spence, P. N. Kean, and W. Sibbett, "60-fsec pulse generation from a self-mode-locked Ti:sapphire laser," Opt. Lett **16**, 42-44 (1991).

13 R. H. Stolen and C. Lin, "Self-phase modulation in silica optical fibers," Phys. Rev. A **17**, 1448-1454 (1978).

14 J. C. Knight, T. A. Birks, P. St. J. Russell, and D. M. Atkin, "All-silica single-mode fiber with photonic crystal cladding," Opt. Letters **21**, 1547 - 1549 (1996).

15 J. K. Ranka, R. S. Windeler and A. J. Stentz, “Visible continuum generation in air-silica microstructure optical fibers with anomalous dispersion at 800nm,” Opt, Letters **25**, 25 - 27 (2000).

16 H. Lim, F. Ö. Ilday, and F. W. Wise, “Femtosecond ytterbium fiber laser with photonic crystal fiber for dispersion control,” Opt. Express **10**, 1497-1502 (2002).

17 X. Feng, H-Y. Tam, and P. K. A. Wai, “Stable and uniform multiwavelength erbium-doped fiber laser using nonlinear polarization rotation,” Opt. Express **14**, 8205-8210 (2006).

18 A. B. Rulkov, M. Y. Vyatkin, S.V. Popov, J. R. Taylor, and V. P. Gaponstev, “High brightness picoseconds all-fiber generation in 525-1800 nm range with picoseconds Yb pumping,” Opt. Express **13**, 377 – 381 (2005).

19 WhiteLaseSC450-PP-HE datasheet: www.fianium.com/pdf/whitelase_HE_v2.pdf

20 G. New, “Chapter 1: Introduction,” in *Introduction to nonlinear optics*, 1st edition (Cambridge University Press, 2011).

21 R. W. Boyd, “Chapter 4: The intensity dependent refractive index,” in *Nonlinear Optics*, 2nd edition 2nd edition (Academic Press, 2003).

22 A. W. Snyder and J. Love, “Chapter 1: Bound rays of planar waveguides,” in *Optical waveguide theory,* (Springer, 1984)

23 R. R. Aflano, “Chapter 3: Ultrashort pulse propagation in nonlinear dispersive fibers,” in *The supercontinuum laser source,* 2nd edition (Springer, 2006)

24 G. New, “Chapter 6: Dispersion and optical pulses,” in *Introduction to Nonlinear optics*, 1st edition (Cambridge University Press, 2011).

25 A. Huttunen, and P. Törmä, “Optimization of dual-core and microstructure fiber geometries for dispersion compensation and large mode area,” Opt. Express **13**, 627-635 (2005).

26 B. E. Olsson and D. J. Blumenthal, “All-optical demultiplexing using fiber cross-phase modulation (XPM) and optical filtering,” IEEE Photon. Technol. Letters **13**, 875 – 877 (2001).

27 M. Rusu, R. Herda, and O. G. Okhotnikov, “Passively synchronized erbium (1550-nm) and ytterbium (1040-nm) mode-locked fiber lasers sharing a cavity,” Opt. Letters **29**, 2246-2248 (2004).

28 G. Agrawal, “Chapter 10: Four-wave mixing,” in *Nonlinear fiber optics*, 3rd edition (Academic Press, 2001).

29 J. M. Dudley and J. R. Taylor, “Chapter 8: Continuous wave supercontinuum generation,” in *Supercontinuum generation in optical fibers*, (Cambridge University Press, 2010).

30 A. Hasegawa and F. Tappert, “Transmission of stationary nonlinear optical pulses in dispersive dielectric fibers. 1. anomalous dispersion,” Applied Phys. Letters **23**, 142-144 (1973).

31 F. M. Mitschke and L. F. Mollenauer, “Discovery of the soliton self-frequency shift,” Opt. Letters **11**, 659 – 661 (1986).

32 J. Herrmann, U. Griebner, N. Zhavoronkov, A. Husakou, D. Nickel, J. C. Knight, W. J. Wadsworth, P. St. J. Russell, and G. Korn, “Experimental evidence for supercontinuum generation by fission of higher-order solitons in photonic fibers,” Phys. Rev. Letters **88**, 173901-173905 (2002).

33 S. Roy, S. K. Bhadra, K. Saitoh, M. Koshiba, and G. P. Agrawal, “Dynamics of Raman soliton during supercontinuum generation near the zero-dispersion wavelength of optical fibers,” Opt. Express **19**, 10443-10455 (2011).

34 A. V. Gorbach and D. V. Skryabin, “Light trapping in gravity-like potentials and expansion of supercontinuum spectra in photonic-crystal fibres,” Nat. Photonics **1**, 653-657 (2007).

35 T. A. Birks, J. C. Knight, and P. St. J. Russell, “Endlessly single-mode photonic crystal fiber,” Opt. Letters **22**, 961-963 (1997).

36 A. Ferrando, E. Silvestre, P. Andrés, J. J. Miret, and M. V. Andrés, “Designing the properties of dispersion-flattened photonic crystal fibers,” Opt. Express **9** 687-697 (2001).

37 W. H. Reeves, J. C. Knight, P. St. J. Russell and, p. J. Roberts, “Demonstration of ultra-flattened dispersion in photonic crystal fibers,” Opt. Express **10**, 609-613 (2002).

38 K. Saitoh and M. Koshiba, “Highly nonlinear dispersion-flattened photonic crystal fibers for supercontinuum generation in a telecommunication window,” Opt. Express **12**, 2027-2032 (2004).

39 W. J. Wadsworth, N. Joly, J. C. Knight, T. A. Birks, F. Biancalana, and P. St. J. Russell, “Supercontinuum and four-wave mixing with Q-switched pulses in endlessly single-mode photonic crystal fibres,” Opt. Express **12**, 299-309 (2004).

40 T. A. Birks, W. J. Wadsworth, and P. St. J. Russell, “Supercontinuum generation in tapered fibers,” Opt. Letters **25**, 1415-1417 (2000).

41 W. J. Wadsworth, A. Ortigosa-Blanch, J. C. Knight, T. A. Birks, T.-P. Martin Man, and P. St. J. Russell, “Supercontinuum generation in photonics crystal fibers and optical fiber tapers: a novel light source,” J. Opt. Soc. Am. B **19**, 2148-2155 (2002).

42 G. Bouwmans, F. Luan, J. C. Knight P. St. J. Russell, L. Farr, B. J. Mangan, and H. Sabert, “Properties of a hollow-core photonic bandgap fiber at 850 nm wavelength,” Opt. Express **11**, 1613-1620 (2003).

43 F. Yu, W. J. Wadsworth, and J. C. Knight, “Low loss silica hollow core fibers for 3-4 μm spectral region,” Opt. Express **20**, 11153-11158 (2012).

44 A. Zakery and S. R. Elliot, “Optical properties and applications of chalcogenide glasses: a review,” J. Non-crystalline solids **330**, 1-12 (2003).

45 J. M. Harbold, F. Ö. Ilday, F. W. Wise, and B. G. Aitken, “Highly nonlinear Ge-As-Se and Ge-As-S-Se glasses for all-optical switching,” IEEE Photonic. Tech. Letters **14**, 822-824 (2002).

46 V. Moizan, V. Nazabal, J. Troles, P. Houizot, J-L. Adam, J-L. Doualan, R. Moncorgé, F. Smektala, G. Gadret, S. Pitois, G. Canat, "Er^{3+}-doped GeGaSbS glasses for mid-IR fibre laser application: synthesis and rare earth spectroscopy," Opt. Materials **31**, 39-46 (2008).

47 J. Requejo-Isidro, A.K. Mairaj, V. Pruneri, D.W. Hewak, M.C. Netti, and J. J. Baumberg, "Self refractive non-linearities in chalcogenide based glasses" J. Non-crystalline solids **317**, 241-246 (2003).

48 M. R. E. Lamont, B. Luther-Davies, D. Y. Choi, S. Madden, and B. J. Eggleton, "Supercontinuum generation in dispersion engineered highly nonlinear (gamma =10/W/m) As(2)S(3) chalcogenide planar waveguide," Opt. Express **16**, 14938-14944 (2008).

49 V. G. Ta'eed, N. J. Baker, L. Fu, K. Finsterbusch, M. R. E. Lamont, D. J. Moss, H. C. Nguyen, B. J. Eggleton, D. Y. Choi, S. Madden, and B. Luther-Davies, "Ultrafast all-optical chalcogenide glass photonic circuits," Opt. Express **15**, 9205-9221 (2007).

50 J. S. Sanghera, L. B. Shaw, C. M. Florea, P. Pureza, V. Q. Nguyen, F. Kung, and I. D. Aggarwal, "Nonlinear properties of chalcogenide glass fibers," J. Optoelectron. Adv. Mat. **8**, 2148-2155 (2006).

51 K. Petkov and P. J. S. Ewen, 'Photoinduced changes in the linear and non-linear optical properties of chalcogenide glasses' J. Non-crystalline solids **249**, 150-159 (1999).

52 E. C. Mägi, L. Fu, H. C. Nguyen, R. E. Lamont, D. I. Yeom, and B. J. Eggleton, 'Enhanced Kerr nonlinearity in sub-wavelength diameter As_2Se_3 chalcogenide fiber tapers' Optics Express **15**, 10324-10329 (2007).

53 D. I. Yeom, E. C. Mägi, M. R. E. Lamont, M. A. F. Roelens, L. Fu, and B. J. Eggleton, "Low-energy threshold supercontinuum generated in highly nonlinear As_2Se_3 chalcogenide submicron tapers," Opt. Letters **33**, 660-662 (2008).

54 R. DeSalvo, A. A. Said, D. J. Hagan, E. W. Van Stryland, and M. Sheik-Bahae, "Infrared to ultraviolet measurements of two-photon absorption and n_2 in wide bandgap solids," IEEE J. Quantum Electron. **32**, 1324-1333 (1996).

55 P. Domachuk, N. A. Wolchover, M. Cronin-Golomb, A. Wang, A. K. George, C. M. B. Cordeiro, J. C. Knight, and F. G. Omenetto, "Over 4000 nm bandwidth of mid-IR supercontinuum generation in sub-centimeter segments of highly nonlinear tellurite PCFs," Opt. Express **16**, 7161-7168 (2008).

56 N. F. Borrelli, C. Smith, D. C. Allan, and T. P. Seward III, "Densification of fused silica under 193-nm excitation", J. Opt. Soc of Am. B, **14**, 1606 (1997).

57 K. Muira, Jianrong Qiu, H. Inouye, T. Mitsuyu, and K. Hirao, "Photowritten optical waveguides in various glasses with ultrashort pulses," Appl. Phys. Letters **71**, 3329-3331 (1997).

58 N. D. Psaila, R. R. Thomson, H. T. Bookey, S. Shen, N. Chiodo, R. Osellame, G. Cerullo, A. Jha, and A. K. Kar 'Supercontinuum generation in an ultrafast laser inscribed chalcogenide glass waveguide' Opt. Express, **15**, 15776-15781 (2007).

59 M. Hughes, W. Yang, and D. Hewak, "Fabrication and characterization of femtosecond laser written waveguides in chalcogenide glass," Appl. Phys. Letters **90**, 131113-131116 (2007).

60 H. Kanbara, H. Kobayashi, T. Kaino, T. Kurihara, N. Ooba, and K. Kubodera, "Highly nonlinear ultrafast optical kerr shutters with use of organic nonlinear materials," J. Opt. Soc. Am. B **11**, 2216-2223 (1994).

61 M. Sheik-Bahae, A. A. Said, T. H. Wei, D. J. Hagan, and E. W. Van Stryland, "Sensitive measurement of optical nonlinearities using a single beam," IEEE J. Quantum Electron. **26**, 760-769 (1990).

62 J. T. Gopinath, M. Soljačić, E. P. Ippen, V. N. Fuflyigin, W. A. King, and M. Shurgulin, "Third Order nonlinearities in Ge-As-Se based glasses for telecommunications applications," J. Applied Phys **96**, 6931-6933 (2004).

63 S. Hughes, J. M Burzler, G. Spruce, and B. S. Wherrett, "Fast Fourier transform techniques for efficient simulation of Z-scan measurements," J. Opt. Soc. Am. B **12,** 1888-1893 (1995).

64 J. M. Harbold, F. Ö. Ilday, F. W. Wise, J. S. Sanghera, V. Q. Nguyen, L. B. Shaw, and I. D. Aggarwal, "Highly nonlinear As-S-Se glasses for all-optical switching," Opt. Letters **27**, 119-121 (2002).

65 T. Cardinal, K. A. Richardson, H. Shim, A. Schulte, R. Beatty, K. Le Foulgoc, C. Meneghini, J. F. Viens, and A. Villeneuve, "Non-linear optical properties of chalcogenide glasses in the system As-S-Se," J. Non-crystalline Solids **256**, 353-360 (1999).

66 G. Lenz, J. Zimmermann, T. Katsufuji, M. E. Lines, H. Y. Hwang, S. Spälter, R. E. Slusher, S. W. Cheong, J. S. Sanghera, and I. D. Aggarwal, "Large kerr effect in bulk Se-based chalcogenide glasses," Opt. Letters **25**, 254-256 (2000).

67 J. Fatome, C. Fortier, T. N. Nguyen, T. Chartier, F. Smektala, K. Messaad, B. Kibler, S. Pitois, G. Gadret, C. Finot, J. Troles, F. Desevedavy, P. Houizot, G. Renversez, L. Brilland, and N. Traynor, "Linear and nonlinear characterizations of chalcogenide photonic crystal fibers," IEEE J. Lightw. Technol. **27**, 1707-1715 (2009).

68 L. B. Fu, M. Rochette, V. G. Ta'eed, D. J. Moss, and B. J. Eggleton, "Investigation of self-phase modulation based optical regeneration in single mode As_2Se_3 chalcogenide glass fiber," Opt. Express **13**, 7637-7644 (2005).

69 R. E. Slusher, G. Lenz, J. Hodelin, J. Sangherra, L. Brandon Shaw, and I. D. Aggarwal, "Large raman gain and nonlinear phase shifts in high-purity As(2)Se(3) chalcogenide fibers," J. Opt. Soc. Am. B **21**, 1146-1155 (2004).

70 F. Smektala, C. Quemard, L. Leneindre, J. Lucas, A. Barthelemy, C. De Angelis, J. Non-Crystalline Solids **239**, 139-142 (1998).

71 Y. Ruan, W. Li, R. Jarvis, N. Madsen, A. Rode, and B. Luther-Davies, "Fabrication and characterization of low loss rib chalcogenide waveguides made by dry etching," Opt. Express **12**, 5140-5145 (2004).

72 M. Balu, J. Hales, D. Hagan, and E. W. Van Stryland, "White-light continuum z-scan technique for nonlinear materials characterization," Opt. Express **12**, 3820-3826 (2004).

73 A. Major, F. Yoshino, J. S. Aitchison, P. W. E. Smith, E. Sorokin, and I. T. Sorokina, "Ultrafast nonresonant third-order optical nonlinearities in ZnSe for photonic switching at telecom wavelengths," Applied Phys. Letters **85**, 4606-4608 (2004).

74 M. Lehtonen, G. Gnety, H. Ludvigsen, and M. Kaivola, "Supercontinuum generation in a highly birefringent microstructered fiber," Applied Phys. Letters **82**, 2197-2199 (2003).

75 D. Ghosh, S. Roy, M. Pal, A. Pal, S. K. Bhadra, J. McCarthy, H. T. Bookey, and A. K. Kar "Generation of supercontinuum and its theoretical study in three-ring silica microstructured optical fibers" Applied Optics **48**, G12-G20 (2009).

76 H. Ademgil and S. Hexha, "Highly nonlinear birefringent photonic crystal fiber," Opt. Comm. **282**, 2831-2835 (2009).

77 C. Xiong and W. J. Wadsworth, "Polarized supercontinuum in birefringent photonic crystal fibre pumped at 1064 nm and application to tuneable visible/UV generation," Opt. Express **18**, 2438-2445 (2008).

78 G. Genty, M. Lehtonen, H. Ludvigsen, J. Broeng, and M. Kaivola, "Spectral broadening of femtosecond pulses into continuum radiation in microstructured fibers," Opt. Express **10**, 1083-1098 (2002).

79 M. Segev, "Optical spatial solitons," Opt. Quantum Electron. **30**, 503-533 (1998).

80 G. I. A. Stegeman, D. N. Christodoulides, and M. Segev, "Optical spatial solitons: historical perspectives," IEEE J. Sel. Topics Quantum Electron. **6**, 1419-1427 (2000).

81 A. Szameit, D. Blömer, J. Burghoff, T. Schreiber, T. Pertsch, S. Nolte, A. Tünnermann, and F. Lederer, "Discrete nonlinear localization in femtosecond laser written waveguides in fused silica," Opt. Express **13**, 10552-10557 (2005).

82 B. Kibler, J. M. Dudley, and S. Coen, "Supercontinuum generation and nonlinear pulse propagation in photonic crystal fiber: influence of the frequency-dependent effective mode area," Applied Phys. B **81**, 337-342 (2005).

83 R. W. Boyd, "Chapter 1: The nonlinear optical susceptibility," in *Nonlinear optics*, 2nd edition (Academic Press, 2003).

84 Z. Zhang, K. Torizuka, T. Itatani, K. Kobayashi, T. Sugaya, and T. Nakagawa, "Self-starting mode-loced femtosecond forsterite laser with a semiconductor saturable-absorber mirror," Opt. Letters **22**, 1006-1008 (1997).

85 A. J. DeMaria, D. A. Stetser, and H. Heynau, “Self modelocking of lasers with saturable absorbers,” Applied Phys. Letters **8**, 174-176 (1966).

86 S. Yamashita, Y. Inoue, S. Maruyama, Y. Murakami, H. Yaguchi, M. Jablonski, and S. Y. Set, “Saturable absorbers incorporating carbon nanotubes directly synthesized onto substrates and fibers and their application to mode-locked fiber lasers,” Opt. Letters **29**, 1581-1583 (2004).

87 J. Ma, G. Q. Xie, P. Lv, W. L. Gao, P. Yuan, L.J. Qian, H. H. Yu, H. J. Zhang, J. Y. Wang, D. Y. Tang, “Graphene mode-locked femwtosecond laser at 2 mu m wavelength,” Opt. Letters **37**, 2085-2087 (2012).

88 A. Martinez, K. Fuse, B. Xu, and S. Yamashita, “Optical deposition of grapheme and carbon nanotubes in a fiber ferrule for passive mode-locked lasing,” Opt. Express **18**, 23054-23061 (2010).

89 H. Zhang, D. Tang, R. J. Knize, L. Zhao, Q. Bao, and K. Ping Loh, “Graphene mode locked, wavelength-tunable, dissipative soliton fiber laser,” Applied Phys. Letters **96**, 111112 (2010).

90 S. Lebedkin, P. Schweiss, B. Renker, S. Malik, F. Hennrich, M. Neumaier, C. Stoermer, M. M. Kappes, “sinlge-walled carbon nanotubes with diameters approaching 6 nm obtained by laser vaporization,” Carbon **40**, 417-423 (2002).

91 Z. Sun, A. G. Rozhin, F. Wang, V. Scardaci, W. I. Milne, I. H. White, F. Hennrich, and A. C. Ferrari, “L-band ultrafast fiber laser mode locked by carbon nanotubes,” Applied Phys. Letters **93**, 06114 (2008).

92 M. A. Solodyankin, E. D. Obraztsova, A. S. Lobach, A. I. Chernov, A. V. Tausenev, V. I. Konov, and E. M. Dianov, “Mode-locked 1.93μm thulium fiber laser with a carbon nanotube absorber,” Opt. Letters **33**, 1336-1338 (2008).

93 J. Wang and W. J. Blau, “Nonlinear optical and optical limiting properties of individual single-walled carbon nanotubes,” Applied Phys. B **91**, 521-524 (2008).

94 P. Ljungberg, R. G. Kihlen, S. H. Lundqvist, P. Potet, and S. Berrebi, “Multispectral imaging MWIR sensor for determination of spectral target signitures,” SPIE Proceedings- The International Society for OptiCAL Engineering, Infrared Technology and Applications XXIII, Orlando, FL, USA, (1997).

95 J. Bland-Hawthorn and P. Kern, “Astrophotonics: a new era for astronomical instruments,” Opt. Express **17**, 1880-1884 (2009).

96 M. Frumar, B. Frumarova, P. Nemec, T. Wagner, J. Jedelsky, M. Hrdlicka, “Thin Chalcogenide films prepared by pulsed laser deposition – new amorphous materials applicable in optoelectronics and chemical sensors,” J. Non-Crystalline Solids **352**, 544-561 (2006).

97 D. A. Turnbull, J. S. Sanghera, V. Q. Nguyen, and I. D. Aggarwal, “Fabrication of waveguides in sputtered films of GeAsSe glass via photodarkening with above bandgap light,” Mat. Letters **58**, 51-54 (2003).

98 J. Fick, É. J. Knystautas, A. Villeneuve, F. Schiettekatte, S. Roorda, and K. A. Richardson, "High photoluminescence in erbium-doped chalcogenide thin films," J. Non-crystalline Solids **272**, 200-208 (2000).

99 J. F. Viens, C. Meneghini, A. Villeneuve, T. V. Galstian, É. J. Knystautas, M. A. Duguay, K. A. Richardson, and T. Cardinal, "Fabrication and characterization of integrated optical waveguides in sulfide chalcogenide glasses," J. Lightw. Technol. **17**, 1184-1191 (1999).

100 Z. G. Lian, W. Pan, D. Furniss, T. M. Benson, A. B. Seddon, T. Kohoutek, J. Orava, and T. Wagner, "Embossing of chalcogenide glasses: monomode rib optical waveguides in evaporated thin films," Opt. Letters **34**, 1234-1236 (2009).

101 C. Tsay, E. Mujagić, C. K. Madsen, C. F. Gmachl, and C. B. Arnold, "Mid-infrared characterization of solution processed As_2S_3 chalcogenide glass waveguides," Opt. Express **18**, 15523-15530 (2010).

102 C. Tsay, Y. Zha, and C. Arnold, "Solution-processed chalcogenide glass for integrated single-mode mid-infrared waveguides," Opt. Express **18**, 26744-26753 (2010).

103 Y. Bellouard, A. Said, M. Dugan, and P. Bado, "Fabrication of high-aspect ratio, microfluidic channels and tunnels using femtosecond laser pulses and chemical etching," Opt. Express **12**, 2120-2129 (2004).

104 R. R. Thomson, T. A. Birks, S. G. Leon-Saval, A. K. Kar, and J. Bland-Hawthorn, "Ultrafast laser inscription of an integrated photonic lantern," Opt. Express **19**, 5698-5705 (2011).

105 G. D. Marshall, A. Politi, J. C. F. Matthews, P. Dekker, M. Ams, M. J. Withford, and J. L. O' Brien, "Laser written waveguide photonic quantum circuits," Opt. Express **17**, 12546-12554 (2009).

106 R. R. Thomson, H. T. Bookey, N. D. Psaila, A. Fender, S. Campbell, W. N. Macpherson, J. S. Barton, D. T. Reid, and A. K. Kar, "Ultrafast-laser inscription of a three dimensional fan-out device for multicore fiber coupling applications," Opt. Express **15**, 11691-11697 (2007).

107 S. M. Eaton, H. Zhang, M. L. Ng, J. Li, W. Chen, S. Ho and, P. R. Herman, "Transition from thermal diffusion to heat accumulation in high repetition rate femtosecond laser writing of buried optical waveguides," Opt. Express **16**, 9443-9458 (2008).

108 J. R. Macdonald, R. R. Thomson, S. J. Beecher, N. D. Psaila, H. T. Bookey, and A. K. Kar, "Ultrafast laser inscription of near-infrared waveguides in polycrystalline ZnSe," Opt. Letters **35**, 4036-4038 (2010).

109 T. Toney Fernandez, G. Della Valle, R. Osellame, G. Jose, N. Chiodo, A. Jha, and P. Laporta, "Active waveguides written by femtosecond laser irradiation in an erbium-doped phoso-tellurite glass" Opt. Express **16**, 15198-15205 (2008).

110 D. G. Lancaster, S. Gross, H. Ebendorff-Heidepriem, A. Fuerbach, M. J. Withford, and T. M. Munro, "2.1 μm waveguide laser fabricated by

femtosecond laser direct-writing in Ho^{3+}, Tm^{3+}: ZBLAN glass," Opt. Letters **37**, 996-998 (2012)

111 A. Baum, P.J. Scully, M. Basanta, C. L. Thomas, P. Fielden, N. Goddard, W. Perrie, P. Chalker, "Photochemistry of refractive index structures in poly(methyl methacrylate) by femtosecond laser irradiation," Opt. Letters **32**, 190–192 (2007).

112 H. T. Bookey, R. R. Thomson, N. D. Psaila, A. K. Kar, N. Chiodo, R. Osellame and G. Cerullo, "Femtosecond laser inscription of low insertion loss waveguides in Z-cut lithium niobate," IEEE Photon. Technol. Letters **19**, 892–894 (2007).

113 R. Osellame, G. Cerulio, and R. Ramponi, "Femtosecond laser micromachining: phohonic and microfluidic devices in transparent materials," (Springer, 2012).

114 S. S. Mao, F. Quéré, S. Guizard, X. Mao, R. E. Russo, G. Petite,and P. Martin, "Dynamics of femtosecond laser interactions with dialectrics," Applied Phys. A **79**, 1695-1709 (2004).

115 A. H. Nejadmalayeri and P. R. Herman, "Ultrafast laser waveguide writing: lithium niobate and the role of circular polarization and picosecond pulse width," Opt. Letters, **31**, 2987-2989 (2006).

116 G. Fibich and A. L. Gaeta, "Critical power for self-focusing in bulk media and in hollow waveguides," Opt. Letters, **25**. 335-337 (2000).

117 GLS data-sheet: http://www.chgsouthampton.com/products/GLSGlassDataSheet.pdf

118 X. Orignac, D. Barbier, X. M. Du, R. M. Almeida, O. McCarthy, E. Yeatman, "Sol-gel silica/titania-on-silicon Er/Yb-doped waveguides for optical amplification at 1.5 μm," Opt. Materials **12**, 1-18 (1999).

119 D. Blömer, A. Szameit, F. Driesow, T. Scheiber, S. Nolte, and A. Tünnermann, "Nonlinear refractive index of fs-laser-written waveguides in fused silica," Opt. Express **14**, 2151-2157 (2006).

120 Y. Nasu, M. Kohtoku, and Y. Hibino, "Low-loss waveguides written with a femtosecond laser for flexible interconnection in a planar light-wave circuit", Opt. Letters, **30**, 723-725 (2005).

121 S. J. Beecher, R. R. Thomson, N. D. Psaila, Z. Sun, T. Hasan, A. G. Rozhin, A. C. Ferrari and A. K. Kar, "320 fs pulse generation from an ultrafast laser inscribed waveguide laser mode locked by a nanotube saturable absorber," Applied Phys. Letters **97**, 111114 (2010).

122 J. R. Macdonald, S. J. Beecher, P. A. Berry, G. Brown, K. L. Schelper, and A. K. Kar, "Efficient mid-infrared Cr:ZnSe channel waveguide laser operating at 2486 nm," Opt. Letters **38**, 2194-2196 (2013).

123 R. Mary, S. J. Beecher, G. Brown, R. R. Thomson, D. Jaque, S. Ohara, and A. K. Kar, "Compact, highly efficient ytterbium doped bismuthate glass waveguide laser," Opt. Letters **37**, 1691-1693 (2012).

124 N. D. Psaila, R. R. Thomson, H. T. Bookey, N. Chiodo, S. Shen, R. Osellame, G. Cerullo, A. Jha, and A. K. Kar, "Er:Yb-doped oxyfluoride

silicate glass waveguide laser fabricated using ultrafast laser inscription," IEEE Photon. Tech. Letters **20**, 126-128 (2008).

125 F. Fusari, R. R. Thomson, G. Jose, F. M. Bain, A. A. Lagatsky, N. D. Psaila, A. K. Kar, A. Jha, W. Sibbett, and C. T. Brown, "Lasing action at around 1.9 μm from an ultrafast laser inscribed Tm-doped glass waveguide," Opt. Letters **36**, 1566-1568 (2011).

126 S. J. Beecher, R. R. Thomson, D. T. Reid, N. D. Psaila, M. Ebrahim-Zadeh, and A. K. Kar, "Strain field manipulation in ultrafast laser inscribed BiB_3O_6 optical waveguides for nonlinear applications", Opt. Letters **36**, 4548-4550 (2011).